REMOTE-SENSING CLASSIFICATION OF FLOODPLAIN LAND COVER AND GEOMORPHOLOGY FROM LANDSAT 7 AND ANCILLARY DATA USING GEOGRAPHIC OBJECT-BASED IMAGE ANALYSIS

A Thesis

by

XINGCHEN CHEN

Submitted to the Office of Graduate and Professional Studies of
Texas A&M University
in partial fulfillment of the requirements for the degree of

MASTER OF SCIENCE

Chair of Committee,	Anthony M. Filippi
Co-Chair of Committee,	İnci Güneralp
Committee Member,	Huilin Gao
Head of Department,	David Cairns

August 2019

Major Subject: Geography

ABSTRACT

Detailed classification of floodplain land cover and geomorphology is a fundamental step in understanding the process-pattern interactions between a river channel and its floodplain. Although supervised classification has been used extensively to classify remote-sensing images for a range of landscapes, including floodplain landscapes, GEOgraphic Object-Based Image Analysis (GEOBIA) has been rarely used to classify vegetation and the geomorphology of these environments. In this study, using GEOBIA, we examine the floodplain of Río Beni, located in the Bolivian Amazon. Río Beni is a highly-dynamic river system, characterized by rapid planform migration and chute and neck cut-off processes that are observable over decadal scales. The Río Beni floodplain is abundant with geomorphic landforms of varying types, ranging from oxbow lakes, meander scars, to scroll bars. The floodplain vegetation is composed of forest and non-forest vegetation, entailing spatially-varying patterns across the floodplain. In order to determine the effects of varying input data on remote sensing-based land-cover and geomorphic classification within the Río Beni floodplain, we perform 24 dataset-combination classification trials, where Landsat 7 ETM+ image bands are combined with various ancillary data layers as joint inputs, including the enhanced vegetation index (EVI), normalized water index (NDWI), and a detrended digital elevation model (DDEM). Overall classification accuracy for the dataset-combination trials range from 55.22% to 88.52%, whereas the Kappa Index of Agreement ranges from 0.4417 to 0.8539. The highest classification accuracies for each respective land-cover and geomorphic class—stemming from the various dataset-combination trials—are: river (91.32%), oxbow lake (96.90%), sandbar (86.68%), scroll bar ridge (28.85%), scroll bar swale (35.53%), forest (97.01%), non-forest vegetation (80.29%), and bare soil (96.39%). Results also indicate that in addition to

the Landsat 7 image, the NDWI image is beneficial to the classification of the river class; the EVI and NDWI images are beneficial to classifying oxbow lake and non-forest vegetation classes; the DDEM aids in the classification of the sandbar class; and the DDEM and NDWI data layers are beneficial to classifying bare soil. Nine automated local threshold methods (Bernsen, Contrast, Mean, Median, MidGrey, Niblack, Otsu, Phansalkar) were also applied to two scroll bar rich areas within our floodplain study site to segment image into scroll bar ridges and scroll bar swales. Result showing Bernsen's method with a local radius 210m can achieve an accuracy of 92.20% across our two study sites. When applying to the whole floodplain, the mean method can achieve an accuracy of 81.02%.

ACKNOWLEDGEMENTS

I would like to thank my committee chair, Dr. Anthony Filippi, my committee co-chair, Dr. İnci Güneralp, and my outside committee member, Dr. Huilin Gao, for their guidance and support throughout the course of this research.

Thanks also goes to my friends and colleagues and the Department faculty and staff for making my time at Texas A&M University a great experience.

Finally, thanks to my mother and father for their encouragement and support throughout graduate school.

CONTRIBUTORS AND FUNDING SOURCES

Contributors

This work was supervised by a thesis committee consisting of Dr. Anthony Filippi and Dr. İnci Güneralp of the Department of Geography, and Dr. Huilin Gao of the Department of Civil Engineering.

The detrended DEM used in this thesis was generated by Billy Hales of the Department of Geography.

All other work conducted for the thesis was completed by the student independently.

Funding Sources

There are no outside funding contributions to acknowledge related to the research and compilation of this document.

TABLE OF CONTENTS

Page

LIST OF FIGURES

Page

LIST OF TABLES

Page

1. INTRODUCTION

Geomorphological floodplain is defined as the largely horizontally-bedded alluvial landform adjacent to a channel, separated from the channel by banks, and built of sediment transported by the present flow-regime (Nanson and Croke 1992).

Floodplains, as an important ecosystem component, have many functions. Flood protection is the first function of the floodplain, by the definition, floodplain is the area that will be inundated in a 100-year flood, so the basic function of the floodplain is to attenuate the peak flows when there is a flooding and enhance the low flows. Floodplain, with its enormous drainage area is the habitat for the wildlife and showing the biodiversity in the ecosystem. For the hydrology perspective, the floodplain has the function of convey and store water, recharge the ground water and essential to protect the water quality.

Detailed classification of floodplain land cover and geomorphology is a fundamental step in understanding the process-pattern interactions between a river channel and its floodplain. Such classification also provides important information for estimating the spatial extent of flooding and developing effective management strategies for rivers and their ecosystems. Although supervised classification (Brondízio et al. 1996; Turner and Congalton 1998; Friedl et al. 2002; Gómez, White and Wulder 2016; Khatami, Mountrakis and Stehman 2016) has been used extensively to classify a range of landscapes, including floodplain landscapes, GEOgraphic Object-Based Image Analysis (GEOBIA) has rarely been used (Furtado et al. 2015; Iersel et al. 2016) to classify vegetation and the geomorphology of these environments. The proposed research will address the use of GEOBIA in land-cover and geomorphology classification of meandering-river floodplains and fill knowledge gaps via the following research objectives:

(1) Establish optimal dataset combinations used as input to the GEOBIA classification method, of those tested, in order to maximize classification accuracy; and

(2) Identify the most accurate scroll bar-specific extraction method based on automated local thresholding, and compare the results with those from GEOBIA.

2. LITERATURE REVIEW

2.1. Floodplain

The definition of the floodplain varies. American hydrologists have stated that the consensus being shared by various state, federal and local authorities is that floods need to be regulated has a probability of occurrence once in 100 years. And they proposed floodplain is the flooded area being affected by the once in 100-year flood event. They also noted that 100-year flood event may or may not be the main flood that result in the formation of the floodplain, but for the lack of better definition, the 100-year flood event is usually treated at the floodplain-forming discharge (Bhowmik and Stall 1979).

Junk, Bayley and Sparks (1989) suggested that the definition of floodplain proposed by Bhowmik and Stall (1979) is arbitrary, obtaining historical record of 100 years would not be possible for some river systems and this definition lacks meaning in ecology. Instead, they defined floodplain as areas that are periodically inundated by the lateral overflow of rivers or lakes, and/or by direct precipitation or groundwater; the resulting physicochemical environment causes the biota to respond by morphological, anatomical, physiological, phenological, and/or ethological adaptations, and produce characteristic community structures. This definition was not focused on the single 100-year flood event but extend it to short or long duration floods. It also incorporated the ecological meaning to the definition by recognize the interaction between the biota and flood event.

Graf (1988) suggested geomorphic history should also be included in the definition of the floodplain. Nanson and Croke (1992) indicated the aforementioned definitions were for hydraulic

floodplain and proposed a new definition. This geomorphological floodplain is defined as the largely horizontally-bedded alluvial landform adjacent to a channel, separated from the channel by banks, and built of sediment transported by the present flow-regime.

Ilhardt, Verry and Palik (2000) also defined the floodplain as the flat depositional area adjacent to the channel of some stream types.

2.2. Vegetation Index

Ever since human being have launched the first civilian Earth observation satellite (Earth Resources Technology Satellite, ERTS-1), scientists are trying to study the vegetation coverage on the earth surface with the data derived from the satellite (USGS 2016). Considering the chlorophyll absorbs visible light ranging from 0.4 to 0.7 um for the purpose of photosynthesis and the strong reflectance of the near-infrared light caused by the cell structure of the plant leaves, this huge difference in the reflectance was used by many researchers to determine the spatial distribution of vegetation in the satellite image.

Various combinations of the red and near-infrared band have been deployed resulting in broad choice of vegetation indices. The following vegetation indices are usually used in literature:

$$DVI = NIR - R \quad (1)$$

Difference Vegetation Index (DVI) is calculated by subtracting the red band from the near infrared band. DVI is sensitive to the vegetation amount but does not account for the difference between radiance and reflectance caused by the atmosphere or shadows.

$$RVI = \frac{NIR}{R} \tag{2}$$

Ratio Vegetation Index (RVI), also called Simple Ratio is represented by near-infrared band divided by red band. Vegetation are often associated with high RVI, water, ice and soil are often associated with low RVI. RVI also reduces the atmospheric and topographic effects.

$$NDVI = \frac{NIR - R}{NIR + R} \tag{3}$$

Normalized Difference Vegetation Index (NDVI), like the RVI is a ratio-based vegetation index but calculated by dividing the difference between near-infrared band and red band by the sum of the near-infrared and red band. NDVI has a range of -1 to 1 and is strongly linked to the amount of vegetation. NDVI have the advantages of minimizing the topographic effects and exhibiting a good differentiation between vegetation and soil.

In general, NDVI is a simple and effective vegetation index being used to assess the plant grow and vegetation cover in a local or global scale (Henik 2012). In addition to assessing the vegetation, the NDVI is also found to have a strong connection to the surface emissivity (Valor and Caselles 1996), being an important component in the weather prediction models (Gutman and Ignatov 1998) and is widely used in ecosystem related researches such as determining the habitats for animals (Hurlbert 2004) and assessing the land degradation at multiple scales (Yengoh et al. 2014).

The Enhanced Vegetation Index (EVI) was proposed by the Moderate Resolution Imaging Spectroradiometer (MODIS) Land Discipline Group as an improvement over NDVI. In the

equation (equation 4), NIR, R, and B are atmospherically-corrected surface reflectances in near-infrared, red, and blue bands respectively. G is a gain factor, C_1 and C_2 are the coefficients of the aerosol resistance term, which uses the blue band to correct for aerosol influences in the red band, and L is a canopy background adjustment (Huete et al. 2002; Jiang et al. 2008). EVI was originally used for MODIS and the parameter values for G, C_1 and C_2 and L are 2.5, 6, 7.5, and 1, respectively (Huete, Justice and Liu 1994). EVI is based on feedback-based approach that incorporates both background adjustment and atmospheric resistance concept (Matsushita et al. 2007).

$$EVI = G\frac{NIR - R}{NIR + C_1R - C_2B + L} \quad (4)$$

Huete et al. (2002) found NDVI and EVI demonstrated good dynamic range and sensitivity for monitoring and assessing spatial and temporal variations in vegetation amount and condition. However, he also noted that NDVI is trend to saturate in high biomass regions for example in the Amazon while EVI is still sensitive to the canopy variations.

Since Landsat project is the world's longest running collection of satellite imagery of Earth, many researches were conducted using Landsat images and EVI is widely applied. The wavelength of the blue, red, near-infrared band of MODIS are 459-479nm, 620-670nm and 841-876nm respectively. Since those specifics are similar to the wavelength used in the Landsat satellite (Table 3), the values for G, C_1, C_2 and L used in MODIS can be applied to Landsat image directly or with little modification. Oguro et al. (2003) used Landsat derived EVI to monitor rice field in the growing season. Soudani et al. (2006) used Landsat derived EVI for leaf area index estimation in

temperate coniferous and deciduous forest stands. Hassan, Bourque and Meng (2007) used Landsat derived EVI in mapping seasonal accumulation of growing degree days. Tatsumi et al. (2015) used Landsat derived EVI to develop a new technique for crop type classification. They all adopted the same parameter setting recommend by Huete et al. (1994). Wu et al. (2010) used a series of vegetation indices calculated based on Landsat TM image and Hyperion image to estimate the canopy chlorophyll content of the maze field. In the calculation of the EVI, he used the same parameter values recommend by Huete et al. (1994), except changed the C_2 parameter from 7.5 to 7.

2.3. GEOgraphic Object-Based Image Analysis (GEOBIA) Overview

Ever since the first Landsat satellite was launched in 1972, imagery derived from the remote sensor has provide tremendous information about the earth surface we lived on. Since earth surface reflectance are captured and recorded in digital remote sensing imagery with pixel as the smallest unit, most methods developed since 1970s are based on the individual pixel and try to use different algorithms to extract information from pixel values. These approached are called pixel-based methods. In the last a few decades, we has seen fast development in the remote sensing field, with higher resolution sensors being launched into the space, more and more high quality remote sensing imagery available to the public at no cost or less cost than before, people's awareness of the remote sensing products and interacting with them in daily life such as weather forecast and maps from google earth images. Scientists and researchers are also thinking about possibility of the extracting surface reflectance information based on other methods than the pixel-based method.

As early as 1990s, several research groups have found the pre-defined boundaries such as the boundaries of the agricultural fields can be used to increase the accuracy of the terrain objects classification (Janssen 1994).

In the case that no pre-defined boundary is available, how to include neighborhood information across several spectral bands is a question need to be answered. Image segmentation is one of the solutions emerged at that time.

Segmentation methods introduced before 2000 are mainly focus on the grey scale imagery. Kartikeyan, Sarkar and Majumder (1998) noted that although segmentation of grey scale image has some development in the field of robotic vision and many other fields, image segmentation based on the color or multi-band imagery has shown little development. Kartikeyan et al. (1998) further divided the segmentation methods into two categories: local behavior based approach and global behavior based approach. Local behavior based approach used variance of feature in a small neighborhood to derive segmentation result. Depending on the analytic method used, local behavior based approach can be classified into two categories: edge detection method and region growing method. Edge detection is primarily applying a moving window to a neighborhood of pixels that will derive high value if edge is detected. N-dimensional edge detection methods have been applied in Di Zenzo (1986) and Trahanias and Venetsanopoulos (1993). Another method is the region growing method which first select a small number of pixels, test the homogeneity of those selected pixels based on specific region model. Next step is to split or merge depending on the homogeneity values derived in the prior step. Skidmore (1989) proposed a region growing algorithm that started with single seed pixel using the homogeneity criterion. Thomas et al. (1987) in his review article, examined several separability indices such as Euclidean distance, divergence,

Jeffries-matusita distance and Bhattacharyya distance for their effectiveness in separating classes of interest to the user.

Baatz et al. (2000) proposed a new optimization method for high quality multi-scale image segmentation. This method is generally a region growing method. It started with treating each pixel in the image as one image object. And the next step is to compare a pair of image objects to see if those two image objects can be merged into larger object. The criterion for merging is based on the local homogeneity, comparing the similarity of adjacent image objects. A value called "merging cost" is being calculated for each potential merge. These costs are indicator of "degree of fitting". If the degree of fitting is smaller than the "least degree of fitting" decided by the end user, the merging will be complete. This whole procedure will come to an end if there are no potential merges as permitted by the "least degree of fitting". Since smaller "least degree of fitting" will permit less merging than larger "least degree of fitting", which will cause smaller image objects at the end of segmentation, hence the "least degree of fitting" is also called "scale parameter". Larger "scale parameter" will generate larger segmentation objects. The calculation of "degree of fitting" and heterogeneity criteria is described in detail in the paper. This segmentation method is adopted in the commercial object-based analysis software eCognition and being used by many researchers afterwards.

2.4. GEOgraphic Object-Based Image Analysis (GEOBIA)-Related Research

Flanders, Hall-Beyer and Pereverzoff (2003) used an object-based approach to classify forest cut blocks in Canada. Landsat 7 ETM+ bands 1-5 and 7 were used in the segmentation with equal weighting, and in the classification process, spectral characteristics, texture, shape, and the hierarchical relationships between objects of different sizes were selected as the class membership

functions to assign class. Results demonstrated that the object-based accuracies of cut block scars, sparse forest, young forest, mature forest, urban objects, and water were significantly higher than those derived from a traditional pixel-based method (maximum likelihood classification).

Drăguţ and Blaschke (2006) implemented object-oriented image analysis in an effort to automatically classify the landform elements. Three layers consisting of slope gradient, profile curvature, and plan curvature derived from a digital terrain model (DTM), in addition to the DTM, were used as input layers for the segmentation. Segmentation was conducted in eCognition software, where four scale parameters values—300, 200, 100, and 10—were used to generate segmented images with various object sizes. Segmented images were then draped over the DTM to classify image into nine landforms such as peak, shoulder, and side slope. The result showing multiscale image segmentation can achieve a satisfying result for the geomorphometry and terrain classification.

Chubey, Franklin and Wulder (2006) applied an object-based approach to IKONOS-2 imagery to derive forest inventory information. Results showed that the segmented objects carried important forest-related information, such as spectral and spatial characteristics of forest stands, which is essential in differentiating various forest stand species.

Dorren, Maier and Seijmonsbergen (2003) examined whether topographic-corrected Landsat TM images along with DEMs can improve the accuracy in mapping forest stand types in steep mountainous terrain. A forest mask derived from the Landsat TM image data was used to generate first-level segmentation results, which were then used to differentiate forest and non-forest areas. Objects assigned as forest were then used to generate second-level, finer-scale segmentation results. A decision tree was used in the classification process in order to classify the forest into four stand types. Results indicated that the object-based method does not yield any

improvement over the per-pixel classification in the forest stand classification, based on overall accuracy values and kappa statistics. However, the authors noted that the forest stand type map derived from object-based method agrees more with reality. This controversy is likely caused by not using randomly sampled truth in the validation process.

Forghani, Cechet and Nadimpalli (2007) applied object-based classification on multi-sensor optical imagery for the generation of terrain surface roughness information, which can be used in wind risk simulation. Sensors used included MODIS, Landsat, and IKONOS; the utility of such derived image data was tested, and results showed that object-based image classification improves the quality of the terrain mapping relative to the pixel-based maximum likelihood classification method.

Frohn et al. (2011) applied segmentation and object-based processing to Landsat ETM+ images, with an aim to classify wetlands in Alachua County, Florida, USA. The segmentation method used in that study was a bottom-up, region-merging approach, and output was generated at three scales: scale 50 was used for data masking, and scales 7 and 10 were used for classification. Membership functions were used in classifying the objects into wetland or non-wetland classes, and membership features used were spectral mean, shape, and size parameters, texture, and ratio of band 4 to the overall brightness values. The results indicated that the object-based classifier outperformed the maximum likelihood classifier by 12%.

Kim, Madden and Xu (2010) used very high spatial-resolution image data and GEOBIA method to map vegetation in Great Smoky Mountains National Park, USA. Segmentation was performed on the three spectral bands of the 0.5-m spatial-resolution aerial photograph, with a series of scale parameter values, ranging from 50 to 300. In the classification process, spectral and non-spectral ancillary data, such as three texture measures calculated from grey-level co-

occurrence matrix (i.e., contrast, correlation and entropy) were used. Results indicated that the incorporation of topographic and texture variables increased the accuracy of the vegetation classification by 5% and 2.8% respectively, as measured by the Kappa Index of Agreement.

Lewinski (2006) used Landsat ETM+ image bands 2, 3, and 4, as well as the panchromatic band, to produce three pan-sharpened images. Then, two levels of segmentation were performed in eCognition software: level one only employs the panchromatic image at a fine scale, and level two uses the three pan-sharpened images, with a 1:2:1 weighting scheme at a coarse scale. Classification was also conducted via eCognition with the following parameters of the object chosen to aid the classification: spectral standard deviations, spectral average values, and Haralick texture functions. Results showing land-use class separation did not significantly improve with the inclusion of the panchromatic image. However, the panchromatic image was found to be beneficial to the image-segmentation process.

Myint et al. (2011) used QuickBird image data to determine whether an object-based classifier can delineate urban features correctly in Phoenix, Arizona. Multispectral image segmentation using eCognition was performed to generate image segments at four scales: 10, 25, 50, and 100. Two object-based classification methods—a membership function classifier and a nearest-neighbor classifier—were tested. Results demonstrated that an object-based classifier can achieve a higher overall accuracy (90.40%) compared with a commonly-used pixel-based classifier (i.e., maximum likelihood) (67.6%).

Powers, Hay and Chen (2012) proposed a GEOBIA method, which includes new object-based texture measures (*geotex*) and a decision-tree classifier (*see5*). The authors utilized this approach to investigate how wetland type and area differ across use of five spatial resolutions, ranging from 5m to 30m. Multi-scale segmentation was performed via Size-Constrained Region

Merging (SCRM) software on pan-sharpened SPOT 5 images, resampled into 5 scales. The decision tree was then used to classify segmented objects into 15 wetland classes. Results showed that 10-m is the spatial resolution that yields the highest classification accuracy, of those tested.

Thomas, Hendrix and Congalton (2003) compared three methods for effectiveness in extracting land-cover and land-use information using 1-m high-resolution digital imagery. The three methods compared were: supervised/unsupervised per-pixel classification, raster-based spatial modeling, and image segmentation with a classification-tree analysis. The results indicated that the spatial-modeling method had the highest overall accuracy (81%), whereas the objected-based approach yielded an accuracy of 70%, and the supervised/unsupervised approach posted the lowest accuracy (58%).

3. STUDY SITE AND DATA

3.1. Study Site

In this study, we examine the floodplain of Río Beni (Figure 1), located in the Bolivian Amazon. Río Beni, with its upper sub-catchments in Andean and sub-Andean ranges, is a main tributary of the Madeira River and counts for 72% of the sediment load in Madeira River (Guyot, Jouanneau and Wasson 1999; Gautier et al. 2007). Latrubesse, Stevaux and Sinha (2005) indicated there are limited knowledge available on tropical rivers. This statement is especially true for river systems in Amazonian floodplains. Previous fluvial dynamics studies are mainly focus on anastomosed river systems in the middle and lower Amazon river (Mertes, Dunne and Martinelli 1996; Dunne et al. 1998; Mertes and Dunne 2007) as well as Rio Negro (Franzinelli and Igreja 2002; Latrubesse and Franzinelli 2002). The analysis of the Río Beni floodplain will provide new information of the meandering river system. Río Beni is a highly dynamic river system, characterized by rapid planform migration and chute and neck cut-off processes that are observable decadal scales. The sinuosity index in the upper part of the floodplain ranges from 1.5 to 2 and in the lower part it ranges from 3.5 to 4 (Gautier et al. 2010). Gautier et al. (2007) observed 27 cut-off processes occurred during 1967-2001 and those meander cut-offs generate plentiful abandoned channels which some of them are transited to oxbow lakes. Other than oxbow lake, the floodplain of Río Beni is also abundant with geomorphic landforms such as meander scars and scroll bars. The floodplain vegetation is composed of forest and non-forest vegetation, entailing spatially-varying patterns on the floodplain. In this study, we examined a total area of 2682 square kilometers of the floodplain, extending from 12˚14′ S to 14˚19′ S and from 66˚52′ to 67˚33′ W.

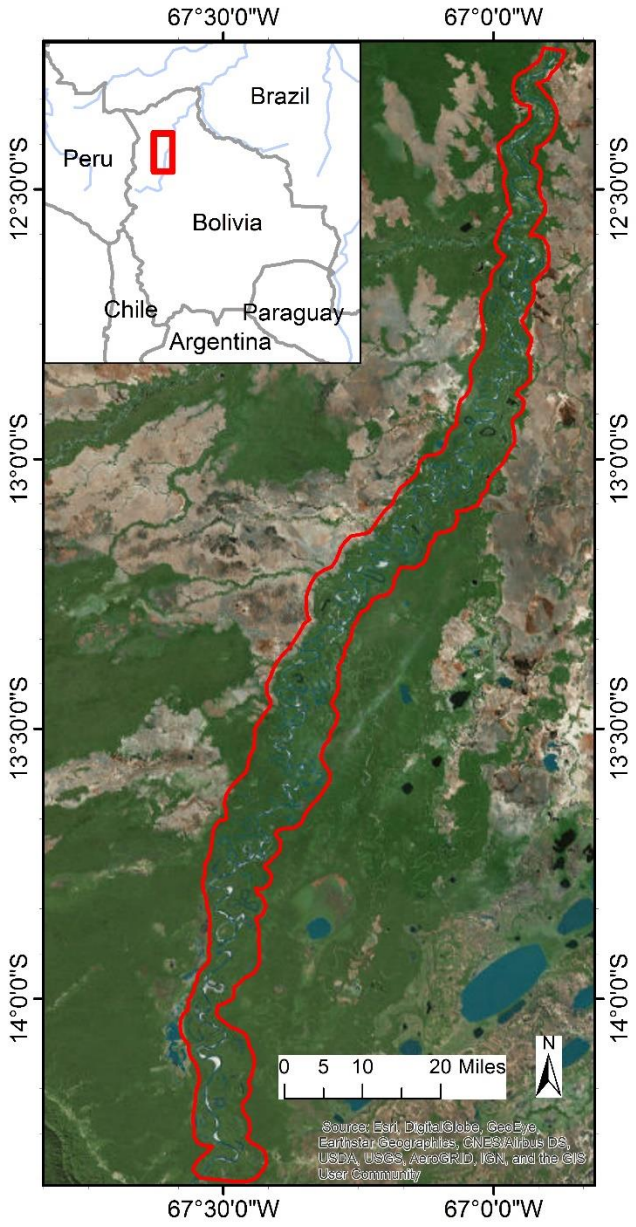

Figure 1. Study site: Río Beni Floodplain in Bolivia.

3.2. Digital Elevation Model

Digital Elevation Model (DEM) which can display the terrain's surface in 3D visualization is commonly used by geomorphologists to measure and extract the surface characters. Currently, a variety of DEM products are available to the public at no cost.

3.2.1. United States National Elevation Dataset

The National Elevation Dataset (NED) provided by the U.S. Geological Survey (USGS) is a DEM dataset with coverage of the mainland US and its territories. The elevation data inside NED all share a consistent resolution and elevation units (Gesch et al. 2002).

3.2.2. ASTER Global Digital Elevation Model

Advanced Spaceborne Thermal Emission and Reflection Radiometer (ASTER) Global Digital Elevation Model (GDEM) is a dataset produced by the Ministry of Economy, Trade and Industry (METI) of Japan and National Aeronautics and Space Administration (NASA) of United States (Jet Propulsion Laboratory 2004). Elevations were measured aboard the Terra satellite launched by NASA in December 1999, using downward- and rearward-pointing stereoscopic cameras. These cameras captured overlapping near-infrared images of effectively global geographic extent (latitudes S83 to N83). The first version of the GDEM (GDEM1) was released in June 2009, and the second version of the GDEM (GDEM2) was released in October 2011; both versions have a spatial resolution of 30m (NASA/METI/AIST/Japan Space Systems 2009). The second version of the GDEM exhibits higher accuracy over the United States, with an average absolute vertical accuracy approximately -0.2 m, when compared with ~18,207 control points in the Conterminous US (CONUS), and a 17-m precision with a confidence level set at 0.95 (Gesch et al. 2011; Tachikawa et al. 2011; Robinson, Regetz and Guralnick 2014).

3.2.3. Shuttle Radar Topography Mission Digital Elevation Model

Shuttle Radar Topography Mission (SRTM) is a joint mission conducted by the National Aeronautics and Space Administration (NASA), the National Imagery and Mapping Agency (NIMA) under the U.S. Department of Defense, and the German and Italian space agencies, with an aim to acquire radar elevation data at a global scale that can be used to build a high-resolution topographic database of the Earth (Nghiem et al. 2001; Jet Propulsion Laboratory 2019). This mission started when Space Shuttle Endeavour was launched on February 11, 2000, and over a period of 11 days, successfully collected synthetic aperture radar (SAR) data, covering ~80% of the globe (from 60°S to 60°N), with some part of the Earth having more than four times the coverage (Nghiem et al. 2001; Robinson et al. 2014). The radar instrument used in this mission is called the Spaceborne Imaging Radar-C/X-Band Synthetic Aperture Radar, which was previously commissioned for a Space Shuttle Endeavour mission in 1994. However, to fulfill the aim of collecting 3D elevation data of the earth surface, additional C/X band antennas were installed on the 200 foot long mast of the Space Shuttle. With one pair of antennas installed at a known distance, radar interferometry can be used to triangulate the position of the surface point from space.

The resultant elevation dataset derived from SRTM has a spatial resolution of 1 arc-second, or ~30 m for the United States, and 3 arc-seconds, or ~90 m, for the rest of the world at first release. On September 23, 2014, following by an announcement from the White House, 1 arc-second (~30 m) elevation data were made available to the public for the global dataset.

3.2.4. Comparison among various Digital Elevation Models

Since SRTM is humanity's first attempt to generate a high-resolution digital elevation dataset at a global scale, the accuracy of the SRTM dataset is important for all the users around the world. As indicated by the producer, final linear vertical absolute height error of the SRTM dataset is specified to be less than 16m for 90% of the data and final circular absolute geolocation error of the SRTM dataset is set to be less than 20m for the 90% of the data (Rodriguez et al. 2005). In order to verify the SRTM accuracy globally, extensive ground-reference data, including nearly 9.5 million ground control points collected using Kinematic Global Positioning System (KGPS) from six continents (with average error of 50cm) as well as other elevation data sources such as Digital Terrain Elevation Data (DTED) produced by NGA (National Geospatial-Intelligence Agency) have been used to evaluate the accuracy of the SRTM dataset (Rodriguez, Morris and Belz 2006). The evaluation result is shown in Table 1, values in the tables represent 90% errors (Rodriguez et al. 2005).

Table 1. Summary of SRTM accuracy (Rodriguez et al. 2005)

	Africa	**Australia**	**Eurasia**	**Islands**	**N. America**	**S. America**
Absolute Geolocation Error (m)	11.9	7.2	8.8	9.0	12.6	9.0
Absolute Height Error (m)	5.6	6.0	6.2	8.0	9.0	6.2
Relative Height Error (m)	9.8	4.7	8.7	6.2	7.0	5.5
Long Wavelength Height Error (m)	3.1	6.0	2.6	3.7	4.0	4.9

As indicated in Table 1, the absolute height error and absolute geolocation error for South America at 90 percentile is 6.2m and 9.0m respectively, which are less than the 16m and 20m requirement of the mission. Gesch et al. (2011) compared the absolute vertical accuracy of the ASTER GDEM with NED and 1 arc-second SRTM elevation dataset using 18,207 ground control points derived from National Geodetic Survey (NGS) when the second version of the GDEM was first released. The result is shown in Table 2; RMSE denotes the Root Mean Square Error, and LE95 signifies the linear error at the 95% confidence level. We can observe from the table that GDEM2 shows significant improvement over GDEM1 in mean absolute vertical error (from -3.69m to -0.2m). When compares to SRTM, although the mean absolute vertical error of the GDEM2 is slightly smaller (-0.20m compares to 0.73m), other statistics such as standard deviation, RMSE, LE95 still indicating SRTM is more consistent in error which made it more reliable than GDEM2.

Table 2. Absolute vertical accuracy assessment (unit: meter) for four elevation datasets (Gesch et al. 2011)

DEM	**Minimum**	**Maximum**	**Mean**	**Standard Deviation**	**RMSE**	**LE95**
GDEM2	-137.37	64.80	-0.20	8.68	8.68	17.01
NED	-46.21	16.42	-0.33	1.81	1.84	3.61
SRTM	-28.67	28.58	0.73	3.95	4.01	7.86
GDEM1	-127.74	105.41	-3.69	8.58	9.34	18.31

In the same paper, Gesch et al. (2011) also investigated the relationship between the absolute vertical error of GDEM2 and different land-cover types. All the ground control points were classified into three different classes: forest, developed land, and open land. Results indicate that although the RMSE of the absolute vertical error for each class is approximately the same (~9 m), the mean absolute vertical error for each class is quite different. Mean absolute vertical error for forest, developed land, and open land are 3.1m, -0.13m, and -0.95m, respectively. Such high mean error for the forest class can be explained by the method for generating the GDEM. Since GDEM was generated using ASTER stereo-pair surface-reflectance images, for areas with dense vegetation/canopy coverage or human-made structures, the derived DEM will include the elevation of such objects instead of the bare Earth (bare ground). Tachikawa et al. (2011) also confirmed that such error over forested areas can be observed when compared to a 10-m DEM of central Honshu Island generated by the Geographical Survey Institute (GSI) of Japan; absolute vertical error of the GDEM2 is 8.68m, which is larger than the 3.1m error observed in United States.

When comparing the mean error of the ASTER GDEM2 with the SRTM DEM, it is notable that in forested areas, elevation values from ASTER GDEM2 are higher than elevation values from SRTM DEM. This discrepancy can be explained by different methods used to generate those two elevation datasets. Due to the short wavelength (5.6 cm C-band radar) used in the SRTM radar, the interferometric height response in the vegetated area will be scattered, causing the derived DEM higher than bare-Earth and lower than the top of canopy (Kellndorfer et al. 2004). As for the ASTER GDEM2, since it uses stereo images to generate DEM, the derived DEM in the vegetated area will reflects the elevation at the top of canopy.

Wong et al. (2014) also suggested that when comparing both SRTM DEM and ASTER GDEM2 with a high-accuracy Light Detection and Ranging (LiDAR) DEM in a tropical montane forest area located in Malaysian Borneo, SRTM DEM is found to produce better topographic data than ASTER GDEM2.

Since our study site is located in Bolivia, South America, we chose to use the 1 arc-second (~30-m) resolution SRTM DEM based on its accuracy, as well as reliability over the South American continent (Table 1; Table 2). Also, since much of the Río Beni floodplain is densely covered with vegetation, the SRTM DEM is a better choice relative to other available global DEMs since its measured elevations are closer to bare-Earth.

3.3. Detrended DEM

A detrended DEM (DDEM), referred to as a Relative Elevation Model (REM), represents the elevations relative to the stream's or river's water surface or active channel by removing downstream changes in elevation associated with the channel gradient, a process called "detrending" (Olson et al. 2014). A detrended DEM is suitable for extracting subtle floodplain landforms, and its usefulness in extracting side channels and other fluvial landforms along stream/river corridors has been described in Jones (2006).

There are three commonly-used DEM-detrending methods: a kernel density method (Dilts, Yang and Weisberg 2010), an inverse distance weighting method (Olson et al. 2014), and a cross-section method (Jones 2006). The kernel density method and inverse distance weighting method require less time and are more automated than the cross-section method. However, the cross-section method allows user to draw cross-sections manually as a way to control how elevations are extrapolated away from the channel. Hence the cross-section method is superior when dealing

with meandering river systems like the one in our case since the automated algorithm tends to generated more artifacts in the final product. In this study, we adopted the cross-section method, and the process we employed to generate the detrended DEM for our study site is summarized below (Olson et al. 2014):

1. Digitize the left and right bank of the Río Beni, and then smooth the banks via a Savitzky-Golay filter, with a window that achieves maximum smoothness while still preserving the shape of the river banks. In this case, we adopted a 5^{th} order Savitzky-Golay filter with a kernel window of 31 vertices along the river banks.
2. Use the centerline tool in Esri ArcGIS/ArcMap to generate a channel centerline using the digitized left and right river banks. Channel centerlines generated from bends with significant unequal widths of the left and right bank will have an abnormal shape that is not centered between the banks; a Savitzky-Golay filter is used again to correct those abnormalities.
3. Draw the cross section. All cross sections must cross the channel centerline, and cross sections cannot intersect with each other. Cross sections are drawn perpendicular to the channel centerline and extend to the edges of the floodplain; exceptions can be made for meandering river channels, such as the Río Beni in this case. The spacing of cross sections are usually dependent upon the user's requirement of the final detrended DEM.
4. Assign elevations of the river channel to the cross-section. Sample points are created along the channel centerline and then used to extract the elevation of the river surface. Then, the elevation values are passed from the sampling points to the corresponding cross-sections.

5. Create a Triangulated Irregular Network (TIN) from the cross sections. The TIN is then converted to a raster DEM with the extent of the floodplain study area. This raster DEM now represents the elevation of the water surface.
6. The detrended DEM is generated by subtracting the newly-generated water surface DEM from the SRTM DEM of our study site.

The detrended DEM represents the elevation above the water surface in our study area, the Río Beni floodplain; given its properties, we expect the detrended DEM to be beneficial with respect to classification accuracy of land cover and geomorphic objects.

3.4. Satellite Image Acquisition and Preprocessing

The Landsat project is the world's longest-running collection of satellite imagery of the Earth. Since July 23, 1972, when the Earth Resources Technology Satellite was launched, the Landsat mission has continuously been providing moderate spatial-resolution multispectral data of the Earth's surface. The extensive spatio-temporal coverage of Landsat data has enabled researchers in various disciplines to investigate the world's natural resources, including forests, water, minerals, as well as Earth-surface human-related activities, such as urbanization and agriculture (USGS 2019a). Data from Landsat 5 and Landsat 7 have particularly been commonly-analyzed in recent years. Specific characteristics of the Landsat 7 ETM+ sensor are given in Table 3.

Table 3. Landsat 7 Enhanced Thematic Mapper Plus (ETM+) sensor characteristics (Goward et al. 2001).

Bands	**Wavelength Range (Micrometers)**	**Spatial Resolution (Meters)**
Band 1 - Blue	0.45-0.52	30
Band 2 - Green	0.52-0.60	30
Band 3 - Red	0.63-0.69	30
Band 4 - Near Infrared (NIR)	0.77-0.90	30
Band 5 - Shortwave Infrared (SWIR) 1	1.55-1.75	30
Band 6 - Thermal	10.40-12.50	60 * (30)
Band 7 - Shortwave Infrared (SWIR) 2	2.09-2.35	30
Band 8 - Panchromatic	0.52-0.90	15

Image-acquisition date and cloud-cover extent are the two criteria that we consider when selecting appropriate Landsat images for this study site. Since the Shuttle Radar Topography Mission (SRTM) began on February 11, 2000, and since we utilize its product (SRTM DEM) in this study, to minimize the temporal offset between Landsat image and SRTM DEM data acquisitions, we select two Landsat 7 ETM+ scenes (courtesy of the U.S. Geological Survey) acquired on September 12, 1999, as they are cloud-free with minimal temporal disjunction with respect to the SRTM DEM data-collection date. We used two Landsat scenes in order to cover the entire floodplain area of interest.

Standard Landsat data distributed by USGS are in GeoTIFF format, with 30-m pixel size. The Landsat Product Generation System (LPGS) is used to generate three different levels of Landsat products: (1) Precision and Terrain Correction Level (Level-1TP, L1TP); (2) Systematic Terrain Correction Level (Level-1GT, L1GT); and (3) Systematic Correction Level (Level-1GS,

L1GS). The Level-1TP product is radiometrically-calibrated and orthorectified based on a digital elevation model and ground control points, which translates this into being the highest-quality Level-1 product. Correction of relief displacement with this product also makes it suitable for time-series analysis at the pixel scale (USGS 2019b). The two Landsat 7 ETM+ scenes used in this study are Level-1TP products.

3.5. Enhanced Vegetation Index (EVI)

Huete et al. (2002) indicated that the normalized difference vegetation index (NDVI) tends to saturate in high biomass regions, such as in the Amazon rainforest, whereas EVI is still sensitive to forest canopy variations in such areas. Since our study site is located in a tropical floodplain environment, where a large portion of the area is covered with vegetation canopy, we use EVI as the vegetation index layer in our classification process. EVI is calculated using atmospherically-corrected Landsat surface reflectance image data (described below) based on the equation:

$$EVI = G\frac{NIR - R}{NIR + C_1R - C_2B + L} \quad (5)$$

where NIR, R, and B are atmospherically-corrected surface reflectances in near-infrared, red, and blue bands, respectively; G = 2.5, C_1 = 6, C_2 = 7.5, and L = 1.

3.6. Normalized Difference Water Index (NDWI)

McFeeters (1996) introduced Normalized Difference Water Index (NDWI) as a new method to delineate open water features and enhance their presence in images derived from remote sensor. NDWI is calculated using the equation listed below:

$$NDWI = \frac{G - NIR}{G + NIR} \quad (6)$$

In this equation, G and NIR are atmospherically corrected surface reflectances in green and near-infrared bands. Wavelengths selection presented here is aimed to enhance the reflectance of the water body by using green wavelength and limit the low NIR reflectance of the water body. This selection also benefits from the high NIR reflectance presented by soil and vegetation. When applying the equation to multispectral remote sensing image, water body will have positive NDWI values while soil and vegetation will have zero or negative values.

In our study, we use atmospheric corrected Landsat surface reflectance image of our study site to calculate the NDWI layer to be used as ancillary layer in our classification process.

4. METHOD

4.1. Image Pre-processing

Although the Landsat products were geometrically corrected by USGS, a high percentage of images are contaminated by atmospheric effects include aerosol and molecular scattering, gas absorption as well as cloud shadows (Liang, Fang and Chen 2001). Atmospheric correction is needed to remove or minimize those effects before we can retrieve spectral signature from earth surface land covers. Fast Line-of-sight Atmospheric Analysis of Spectral Hypercube (FLAASH®) radiative transfer model is selected in this study to covert the DN values in the original products to surface reflectance. The FLAASH algorithm is based on the existing MODTRAN4 radiative transfer model, which was developed by the Air Force Research Laboratory and Spectral Science Inc. to support atmospheric correction of visible to short-wave infrared multispectral and hyperspectral sensors (Cooley et al. 2002).

Certain parameters are required by the FLAASH model in order to accurately execute the atmospheric correction. Scene center location, flight date and time, sensor altitude, pixel size can be located in the metadata of the downloaded image file. Ground elevation is set as the mean elevation of the full scene calculated using the SRTM. Atmospheric Model is an important parameter in the standard MODTRAN model. Based on water vapor amount in the atmosphere, the whole world can be divided into six different zones: (1) Sub-Arctic Winter (SAW); (2) Mid-Latitude Winter (MLW); (3) U.S. Standard (US); (4) Sub-Arctic Summer (SAS); (5) Mid-Latitude Summer (MLS); (6) Tropical (T). If water vapor amount is not available (our case), Table 4 can be used to decide atmospheric zone based on the relationship between water vapor content and

seasonal-latitude surface temperature (Harris geospatial solutions 2019). In our case, atmospheric model is set to Tropical (T) since mean latitude for our study site is 13˚ and images were acquired on September. Aerosol model in the FLAASH is set to rural, since by definition, this model should be chosen if aerosols in the study area is not heavily affected by industrial or urban sources. For the Aerosol Retrieval method, we chose 2-Band (K-T) method and set the Band 7 (shortwave infrared 2) of the ETM+ image as KT upper channel, Band 3 (red) as KT lower channel.

Table 4. Seasonal-latitude surface temperature model (Harris geospatial solutions 2019)

Latitude (°N)	**Jan**	**March**	**May**	**July**	**Sept**	**Nov**
80	SAW	SAW	SAW	MLW	MLW	SAW
70	SAW	SAW	MLW	MLW	MLW	SAW
60	MLW	MLW	MLW	SAS	SAS	MLW
50	MLW	MLW	SAS	SAS	SAS	SAS
40	SAS	SAS	SAS	MLS	MLS	SAS
30	MLS	MLS	MLS	T	T	MLS
20	T	T	T	T	T	T
10	T	T	T	T	T	T
0	T	T	T	T	T	T
-10	T	T	T	T	T	T
-20	T	T	T	MLS	MLS	T
-30	MLS	MLS	MLS	MLS	MLS	MLS
-40	SAS	SAS	SAS	SAS	SAS	SAS
-50	SAS	SAS	SAS	MLW	MLW	SAS
-60	MLW	MLW	MLW	MLW	MLW	MLW
-70	MLW	MLW	MLW	MLW	MLW	MLW
-80	MLW	MLW	MLW	MLW	MLW	MLW

After completing atmospheric correction for the two Landsat 7 scenes, image mosaicking and subsetting was performed in ENVI 5.4 to derive the atmospherically-corrected surface reflectance image of the study area (Figure 2).

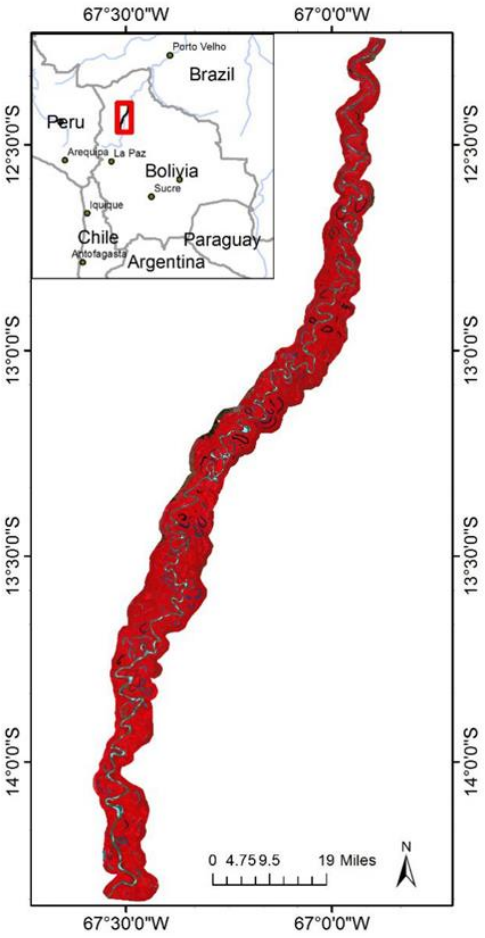

Figure 2. Surface reflectance image of the Río Beni floodplain in false-color composite.

4.2. Reference Region Selection

The floodplain of Río Beni is abundant with geomorphic landforms, ranging from oxbow lakes, meander scars, to scroll bars. Vegetation coverage of the floodplain can often be observed in the following locations: (1) Sand bar—scrub in sandbar can grow to 1-2 m in height and is dominated by *Salix humboldtiana* and *Tessaria integrifolia*; (2) River edge—dominate tree species in this area are *Erythrina, Ochroma* and *Cecropia*, and they can often grow to 20-25 meters in height; (3) Areas seasonally or permanently inundated by weak current—forest in this area is called

varzea forest and is dominated by buttressed trees with close to 30-meter canopy height; (4) Area never flooded—palms and bamboo can be observed in this area and have more undergrowth than other regions (Remsen Jr and Parker III 1983).

Given this, we propose eight (8) land-cover and geomorphic classes (Table 5): (1) River; (2) Oxbow Lake; (3) Sand Bar; (4) Scroll Bar Ridge; (5) Scroll Bar Swale; (6) Forest; (7) Non-forest Vegetation; and (8) Bare Soil. Reference regions for each land-cover and geomorphic class are required for the use as training areas for supervised classification, as well as for validation sites for the subsequent classification accuracy-assessment phase. Since the reflectance variation of the oxbow lake and sand classes present within the Landsat 7 ETM+ image mosiac is very high, those two classes have been further divided into 2 sub-classes to decrease the reflectance variation within sample groups (Table 5).

Table 5. Land cover, geomorphic classes and reference region count

No.	Land Cover and Geomorphic Classes	Reference Classes	Reference Region Count	Area (km^2)
1	River	River	25	39.43
2	Oxbow Lake	I. Oxbow Lake (Bright)	25	27.32
		II. Oxbow Lake (Dark)	25	20.25
3	Sand Bar	I. Sand Bar (Bright)	25	3.49
		II. Sand Bar (Dark)	25	2.94
4	Scroll Bar Ridge	Scroll Bar Ridge	50	2.69
5	Scroll Bar Swale	Scroll Bar Swale	50	4.14
6	Forest	Forest	100	3.96
7	Non-Forest Vegetation	Non-Forest Vegetation	50	20.04
8	Bare Soil	Bare Soil	50	42.05

The surface-reflectance image mosaic derived from the input Landsat 7 image data is the main data source for visually identifying those regions. A Normalized Difference Water Index (NDWI) image was used along with the surface-reflectance image to locate river bank and oxbow lake boundaries. Normalized Difference Vegetation Index (NDVI) image and Landsat Vegetation Continuous Fields (VCF) tree-cover data (Global Land Cover Facility, University of Maryland) are used in conjunction with the surface-reflectance image to delineate forest and non-forest vegetation regions. For scroll bars, due to the limited, moderate spatial resolution of the Landsat image data, many individual scroll bars cannot be accurately delineated using surface-reflectance image alone, a pan-sharpened image of the study site (using the panchromatic band of the Landsat 7 ETM+ sensor to increase detail in the reflectance image) as well as high-spatial resolution Google Earth images acquired during the 2000-2003 time interval are used to help delineate scroll bars in the map. Spectral reflectance variation within each reference class and average area of the individual reference regions are considered together in determining the size for each reference class. The number of regions chosen for each class ranges from 25 to 100, with the total number of reference regions is 425. Reference regions are selected across the study area (Figure 3) to ensure their representativeness of the respective classes, and reduce bias in the sampling process. Digitization of reference regions was performed in ArcMap. Example reference regions are given in Figure 4.

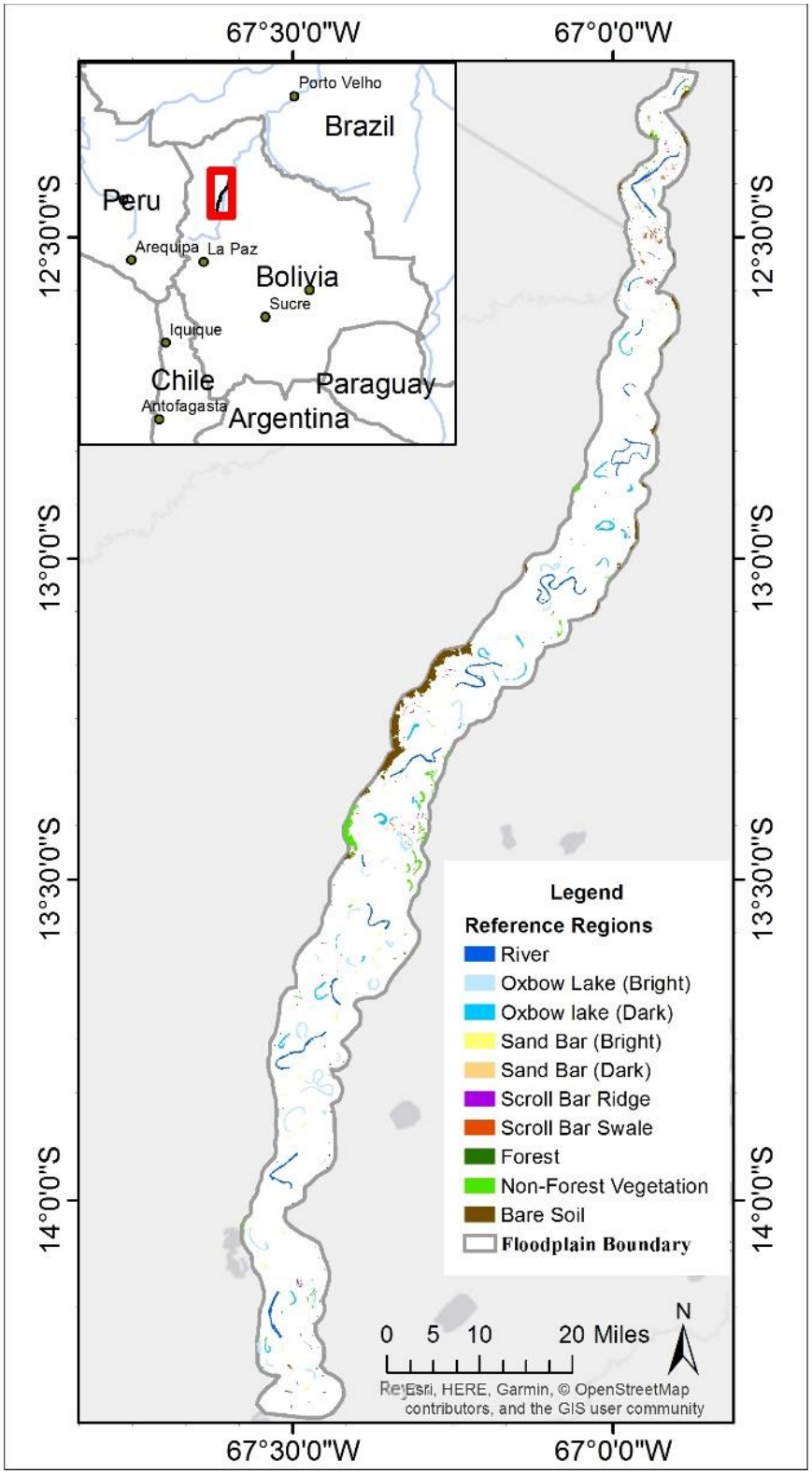

Figure 3. Spatial distribution of the reference regions in Rio Beni study site.

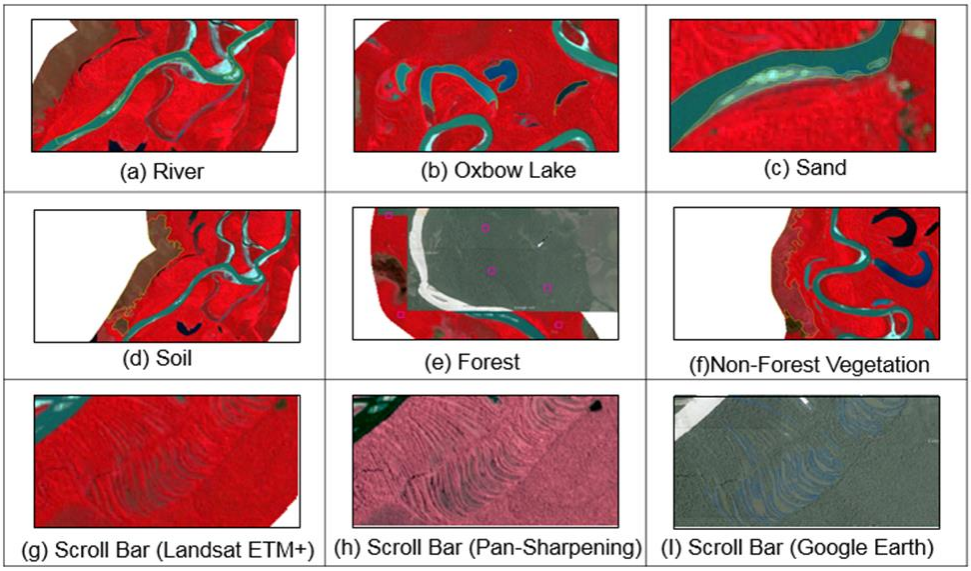

Figure 4. Reference regions of the land-cover and geomorphic classes.

For supervised classification training and validation purposes, reference regions are further divided into two parts: 60% of the reference regions are randomly selected to be used as training samples in the image classification analysis, whereas the rest of the regions serve as reference for the classification accuracy assessment.

4.3. Image Segmentation Using eCognition® Software

4.3.1. eCognition® Image Segmentation Method Overview

eCognition® is remote-sensing image-analysis software developed by Definiens Imaging GmbH in 2000 and was acquired by Trimble in 2010. It was originally designed for medical imaging applications, but remote-sensing professionals, as well as researchers in forestry, urban planning, and agriculture saw the potential of this software to rapidly and accurately extract geo-information from remote-sensing images. The patented Cognition Network Technology used in

eCognition was developed by Nobel Laureate in Physics Gerd Binning. This technology simulates human cognitive perception in extracting information from images, and the use of advanced machine-learning algorithms, as well as the infusion of user knowledge and domain expertise, enable it to automatically process large stores of images (Flanders et al. 2003; Trimble 2010).

Figure 5. Chessboard segmentation

The first step in eCognition image analysis is to divide input image into small pieces, which serve as fundamental blocks for later analysis. This step is called segmentation in this software and results are undefined objects. In general, those objects are relatively crude, but can be refined with additional rule sets. There are two kind of segmentation methods supported by eCognition: (1) A top-down segmentation, which dividing something big into smaller fragments; (2) A bottom-up segmentation, which combining smaller fragments into something bigger. Chessboard segmentation (Figure 5), quadtree-based segmentation, contrast filter/split segmentation are all representative methods within the top-down segmentation. Examples for bottom-up segmentation are multiresolution segmentation and multi-threshold segmentation. The multi-threshold segmentation divides image objects from a user defined pixel value threshold. In our study, we

choose to use multiresolution segmentation, which is a method successively merging image pixels or image objects based on a pairwise region merging technique (Trimble 2011).

To start, this algorithm identify objects with the size of one pixel and then merging them into their neighborhood if the relative homogeneity criteria is met (eCognition Developer 2014). By definition, homogeneity criterion measures the homogeneity of the pixels within image objects and two different parameters, shape and compactness are used in combination to composite this criterion. Shape value ranges from 0.0 to 0.9. By defining a shape value, you defined what percentage of shape homogeneity should be taken into consideration when composite the homogeneity criterion. Also, by changing the shape value, the color criteria (color value = 1 – shape value) will be changed. For example, if the shape value were set to 0.3, color value will automatically set to 0.7 which means homogeneity criterion will 30% depends on the shape homogeneity and 70% depends on the homogeneity of the spectral homogeneity of the input image objects. The maximum value of shape parameter was set to 0.9 since if shape value were set to 1.0, then the output segmentation objects would not have any connections with the image's spectral information. Compactness describes how compact an object is, the more compact an object is, the smaller its border appears. Compactness and smoothness are combined to decide the shape value (Trimble 2011). In this study, after multiple trials, shape value and compactness value are set to 0.1 and 0.5 respectively.

4.3.2. Segmentation Layer Weights and Scale Parameter

Seven raster layers have been chosen to use as the input layer for the segmentation process. Including six 30m resolution atmospheric corrected surface reflectance images (Blue, Green, Red, Near Infrared, Shortwave Infrared 1, Shortwave Infrared 2) derived from Landsat ETM+ and 30m resolution DEM raster from SRTM. After choosing the input layer, individual layer's weight also needs to be set before the segmentation can start. Image layers should be weighted depending on the importance of each layer and their fitness to the result of the segmentation. If higher weight is set to one image layer, then more weight is assigned to this layer's pixel information in the segmentation. Weights for the input layer were usually decided on a case-by-case scenario. Many researchers use equal weights for their input layers. For example, Gupta and Bhadauria (2014) use equal weights for the Landsat ETM+ image bands for a San Antonio, Texas study area, as well as high-spatial resolution orthophotos (acquired in 1995, 2000, 2003 and 2004) to generate segmentation results; Zhang et al. (2010) choose to use equal weighting for the four (4) pan-sharpened multispectral bands (derived from QuickBird and Ikonos multispectral images) acquired over Fredericton, Canada to determine optimal segmentation parameters for eCognition, as well as other researchers (Sun et al. 2014; Wei, Chen and Ma 2005). However, different weighting can be used if there is more information in a given image/layer relative to other data layers. In Syed, Dare and Jones (2005), equal weight (weight = 1) was assigned to each of the multispectral bands due to lack of color homogeneity visually observed within the same features in the image. However, another layer that was used—a LiDAR-derived nDSM layer entailed more homogeneity in grey level; therefore more weight (weight = 5.5) was given to this layer. In Kampouraki, Wood and Brewer (2008), the authors found, through several empirical trials, that the best values for each

parameter were: weight of red band = 2; weight of green band = 4; and weight of blue band = 1. Chubey et al. (2006) found that preliminary correlation analysis of the image data revealed a high degree of correlation among the three bands representing the visible portion of the spectrum (bands 1 through 3), but much lower correlation between the near-infrared band (band 4) and the visible bands. In response to the above considerations and observations, the weightings of the multispectral bands were arranged such that the three visible bands were assigned equal weights, and the sum of the weights assigned to the three visible bands combined equaled the weighting assigned to the near-infrared band.

In our study, we adopt the method proposed by Chubey et al. (2006). We first conduct a correlation analysis on our six (6) 30-m spatial-resolution atmospherically-corrected surface-reflectance images, and the result is given in Table 6. Based on the correlation matrix, blue, green, and red bands are highly correlated (with a correlation index greater than 0.96), as is the case between the first and second SWIR bands (i.e., SWIR 1 and SWIR 2) (where correlation index = 0.82). Based on this information, equal weight should be assigned for Blue, Red and Green band and for SWIR 1 and SWIR 2 band. Since NIR band has low correlation with other bands, greater weight should assign to NIR band to extract more information from this band.

Table 6. Correlation matrix of the surface reflectance images

Correlation Coefficient	Blue	Green	Red	NIR	SWIR 1	SWIR 2
Blue	1.000	0.968	0.961	-0.580	-0.067	0.433
Green	0.968	1.000	0.966	-0.559	-0.111	0.366
Red	0.961	0.966	1.000	-0.618	-0.098	0.409
NIR	-0.580	-0.559	-0.618	1.000	0.637	0.176
SWIR 1	-0.067	-0.111	-0.098	0.637	1.000	0.820
SWIR 2	0.433	0.366	0.409	0.176	0.820	1.000

4.3.3. Selecting optimal segmentation result

In order to observe different weighting combination as well as different scale parameter's effect on the segmentation process, we propose 15 trials as shown in Table 7. First, for the scale parameter, we select three scale parameters (10, 20 and 30) to generate segmentation object at different scale level. Second, within each scale parameter, following our conclusion from previous section, equal weight (weight = 1) has been assigned for Blue, Red and Green band and for SWIR 1 and SWIR 2 band. Different weighting combination between NIR band and SRTM is then adopted for each scale.

Table 7. Segmentation trials with different weighted layers and scale parameter

Trial NO.	Weight							Scale Parameter
	Blue	Green	Red	NIR	SWIR1	SWIR2	SRTM	
1	1	1	1	3	1	1	0	
2	1	1	1	2	1	1	1	
3	1	1	1	3	1	1	1	10
4	1	1	1	2	1	1	2	
5	1	1	1	3	1	1	3	
6	1	1	1	3	1	1	0	
7	1	1	1	2	1	1	1	
8	1	1	1	3	1	1	1	20
9	1	1	1	2	1	1	2	
10	1	1	1	3	1	1	3	
11	1	1	1	3	1	1	0	
12	1	1	1	2	1	1	1	
13	1	1	1	3	1	1	1	30
14	1	1	1	2	1	1	2	
15	1	1	1	3	1	1	3	

Evaluation of the segmentation result is needed once the trials described above are conducted. Generally speaking, there are two kinds of the discrepancies that will occur in the segmentation process:

- Under segmentation, which occurs if the segmentation method divides the image into too few segments, resulting a part or even the whole real world object be contained in another object.
- Over segmentation, which occurs if the segmentation method divides the image into too many segments, resulting the real-world objects being divided into sub-objects.

While over segmentation can divide real word object into multiple parts, it's usually feasible to rebuild the original object using those sub-objects in the post-processing. However,

rebuilding the original object using under-segmentation result would be much harder. Therefore, under- segmented result should be avoided during the segmentation process.

Various accuracy assessment methods have been introduced from the day when image segmentation was first performed and keep evolving as new segmentation methods emerged. In one review paper (Zhang 1996), the author studied different evaluation methods and attempted to generalize those existing methods into three categories:

1) Analytical methods, these methods inspect and analyze the principles as well as the properties behind the segmentation algorithms. One advantage of this evaluation method is that it does not rely on the implementation of segmentation algorithms and thus can avoid the errors introduced by different evaluation trials. However, some properties associated with the algorithm may not be acquired by analytical study, which hinders the usage of this method.
2) Empirical goodness methods, these methods assess the performance of the segmentation algorithms based on the quality of the resulted image. Various quality measurements have to be defined before the implementation of this method. In general, those measurements are linked to human intuition regarding what can be classified as "ideal" segmentation. One advantage of this evaluation method is that it doesn't need a reference image for the assessment process. If reference image is hard to acquire or would be labor-intensive to acquire, empirical goodness method can provide an easy and time-efficient solution. Three criteria are often used in empirical goodness methods:
    a) Uniform property within each region, Levine and Nazif (1985) proposed that ideal segmentation algorithm should result in an image showing higher uniformity within

each segmented region. Variance of the pixel values within each region (Levine and Nazif 1985) and higher order local entropy (Pal and Pal 1989) are some of the properties can be measured here.

b) Contrast among each regions, Levine and Nazif (1985) also proposed that ideal segmentation algorithm should result in an image showing higher contrast among segmented regions. An automatic threshold selection method presented by Otsu (1979), which maximizing the separability of the resulted classes, is based on this criterion.

c) Region shape, instead of focusing on the pixel value, Sahoo, Soltani and Wong (1988) introduced a shape measure which can assess different segmentation algorithms.

3) Empirical discrepancy methods, these methods assess the performance of the segmentation algorithms based on discrepancy between user's segmentation result and an ideal segmented result of the same image. This ideal segmented result is also called reference image or gold standard (de Graaf et al. 1994) in image processing field. In general, these methods examine how much difference can be observed in user's segmentation result when compare to the reference image. Higher difference measurement usually associated with more flaws in the user's segmentation, which indicates the implemented algorithm has lower accuracy. Similar to empirical goodness methods, four criteria are often used in empirical discrepancy methods:

a) Percentage of mis-segmented pixels. This criterion derives from accuracy assessment concept used in pixel-based image classification. If a segmented image has N classes, a confusion matrix of N dimensions can be built and then used to

determine two type of errors (Type I error and Type II error) associated with the segmentation.

b) Location of mis-segmented pixels. This criterion account for the spatial position of the mis-segmented pixels. It's not uncommon to see two segmented images has similar percentage of mis-segmented pixels but with tremendously different spatial pattern.

c) Object counts in the image. This criterion examines the difference of the total objects found in the reference image and user's segmentation result.

d) Feature values of the segmented objects. The ultimate goal for the segmentation process is to extract information, thus if a segmented image can yield same feature values as in the reference image, it would be considered as high quality.

In our study, the empirical discrepancy method is selected since the main purpose for our evaluation is to assess whether image segments are based on "real" objects, such as oxbow lake boundaries, and forest and grassland outlines, in the real world. We need to determine whether the segmentation result from the trials listed on the last section can accurately delineate objects from our eight (8) land-cover and geomorphic classes.

As indicated in Neubert's review paper (Neubert, Herold and Meinel 2008), numerous comparing algorithms have emerged to assess the segmentation quality based on the corresponding reference image. In our study, we adopted a method proposed by Marpu et al. (2010). The criteria used here derive from the concept of under segmentation and over segmentation as defined earlier. Detailed explanation of this method is described below.

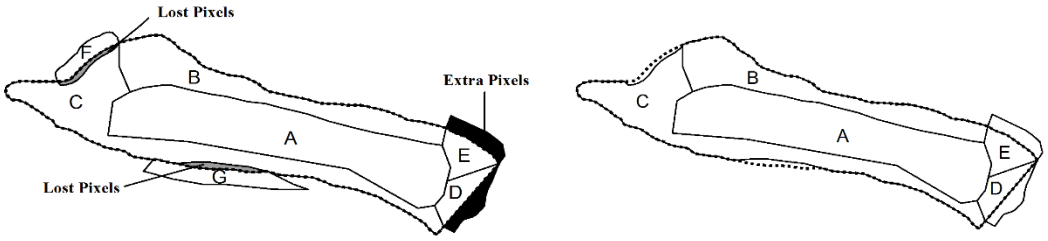

Figure 6.A. Simplified illustration of segmentation showing lost pixels and extra pixels. B. Dotted outline indicating reference object, which can be rebuilt using sub-object A, B, C, D and E in the post processing.

As illustrated in Figure 6A is a simplified result derived from one segmentation experiment. The reference object is outlined by dotted lines while the segmentation process has divided the image into multiple sub-objects (sub-object A to F). Based on the spatial relation with the reference object, those sub-objects either lies completely within the reference object or contain part of the area that is not belong to the reference object. To assess the segmentation quality, only those sub-objects which have enough overlap with the reference object can be retained for the following analysis. In our case 55 percent was chosen as a threshold for the selection. If a sub-object has less than 55 percent overlapping area with reference object, those sub-objects are not considered in the following analysis since they may not contain enough spectral information of the reference object or not beneficial to the regeneration of the reference object. In Figure 6A, sub-object A to E are selected for the following analysis based on the 55 percent threshold, sub-object F and G are not considered due to insufficient overlapping area. By using retained sub-object A to E, reference object can be rebuilt as shown in Figure 6B. After the removal of sub-object F and G, areas showing in grey in Figure 6A are defined as lost pixels since this part of the reference

object is lost during the rebuild. Lost pixels are the overlapped pixels between the reference object and those sub-objects which have less than 55 percent of overlapped area with the reference object. Similarly, extra pixels are defined as the pixels that is outside the boundary of the reference object but belongs to the sub-object which has more than 55 percent overlapped area with the reference object. Extra pixels are showing in black in Figure 6A. Figure 6B shows the difference between the reference object (outlined in dotted line) and the rebuilt reference object (consists of sub-object A to E) using 55 percent overlapping criteria. We can observe that the rebuilt reference object do not include lost pixels but includes extra pixels. Ideally, if a rebuilt reference object matches reference object at 100 percent, the lost pixels and extra pixels will all equal to zero. Thus, lost pixels and extra pixels can be used as criteria to evaluate the quality of the segmentation. Based on this thought, Marpu et al. (2010) proposed five indices to quantitatively assess the segmentation result which is also used in this study:

Index 1: For each reference object, finding the largest sub-object and calculate the ratio between its area (minus any extra pixels if existed) and reference object's area.

Index 2: For each reference object, calculate the ratio between lost pixels and reference object's area.

Index 3: For each reference object, calculate the ratio between extra pixels and reference object's area.

Index 4: the number of the reference objects which lost more than 25 percent of the pixels.

Index 5: the number of the reference objects which gained more than 25 percent of the pixels.

Index 1 to 3 are calculated on the individual reference object. Index 1 has a range (0-1) is a measurement for over-segmentation. Value closes to zero indicates extreme over-segmentation

while value closes to 1 indicates high quality segmentation. Index 2 and 3 can be used together to assess under-segmentation. Segmentation with higher quality is usually corresponding with low reading for those two indices. For image consists of multiple reference objects, index 4 and 5 can be calculated to assess the overall segmentation quality for the whole image.

4.4. Image Classification Using eCognition® Software

eCognition® software provides various methods for the image classification process. In this study, we proposed using classifier algorithm. This algorithm enables us to apply machine-learning functions to our image analysis in a two-step process: First we need to train the classifier using the training samples we obtained in previous section. Second, the trained classifier will be applied to whole image, classifying segmentation objects based on the configuration of the trained classifier (Trimble 2011).

Defining the feature space that going to be used by Nearest Neighbor classifier is the most important setting during the classification process. Four geometry feature space were selected: elliptic fit, shape index, compactness and thickness. Elliptic fit index showing how well an image objects fits into an ellipse of similar size, where value 1 indicates a perfect fit and 0 indicates no fit at all. Shape index showing the smoothness of an image object border, where lower shape index indicating smoother border of the image objects. Compactness index showing the ratio of polygon's area to the area of the circle which has the same perimeter. Compactness index ranges from 0 to 1 where 1 indicating perfect fit. Thickness index is calculated as the smallest of three eigenvalues of a rectangular 3D space with the same volume and same proportions as the image object (Trimble 2011). For spectral information statistical feature space such as mean and standard deviation of the image objects were also include in the classifier.

After classifier is configured, this Nearest Neighbor classifier will be applied to a stack of user defined image layers to execute the classification process.

4.4.1. Classification Trials Using Different Input Datasets

In order to answer our objective two: establish optimal dataset combinations used as input to the GEOBIA classification method that maximize classification accuracy, we proposed 24 different trials to investigate how the change in the input dataset combination will influence the result accuracy (Table 8).

Table 8. Input layer-combination trials

Trial	Segmentation			Classification			
	Layer one	Layer Two	Scale	Layer One	Layer Two	Layer Three	Layer Four
1	Landsat	-	20	Landsat	-	-	-
2	Landsat	-	20	Landsat	EVI	-	-
3	Landsat	-	20	Landsat	NDWI	-	-
4	Landsat	-	20	Landsat	EVI	NDWI	-
5	Landsat	-	30	Landsat	-	-	-
6	Landsat	-	30	Landsat	EVI	-	-
7	Landsat	-	30	Landsat	NDWI	-	-
8	Landsat	-	30	Landsat	EVI	NDWI	-
9	Landsat	DDEM	20	Landsat	-	-	-
10	Landsat	DDEM	20	Landsat	EVI	-	-
11	Landsat	DDEM	20	Landsat	NDWI	-	-
12	Landsat	DDEM	20	Landsat	EVI	NDWI	-
13	Landsat	DDEM	30	Landsat	-	-	-
14	Landsat	DDEM	30	Landsat	EVI	-	-
15	Landsat	DDEM	30	Landsat	NDWI	-	-
16	Landsat	DDEM	30	Landsat	EVI	NDWI	-
17	Landsat	DDEM	20	Landsat	DDEM	-	-
18	Landsat	DDEM	20	Landsat	EVI	DDEM	-
19	Landsat	DDEM	20	Landsat	NDWI	DDEM	-
20	Landsat	DDEM	20	Landsat	EVI	NDWI	DDEM

Table 8. Continued

Trial	Segmentation			Classification			
	Layer one	**Layer Two**	**Scale**	**Layer One**	**Layer Two**	**Layer Three**	**Layer Four**
21	Landsat	DDEM	30	Landsat	DDEM	-	-
22	Landsat	DDEM	30	Landsat	EVI	DDEM	-
23	Landsat	DDEM	30	Landsat	NDWI	DDEM	-
24	Landsat	DDEM	30	Landsat	EVI	NDWI	DDEM

After all the trials have been implemented in eCognition, accuracy assessment will be conducted for each of the 24 trials listed above. As mentioned in previous section, 40 percent of the total reference regions that were generated earlier will be used as validation data in this step. Classification accuracy of each land cover type and geomorphic objects will also be examined to determine the best input dataset combination to extract a certain class.

Following metrics will be used to evaluate the classification accuracy:

1. Producer's accuracy: when calculate the accuracy of land use land cover map, a confusion matrix is often used. As can be seen in Table 9, producer's accuracy for category X can be calculated as correctly classified samples of category X divided by total number of reference samples of category X (equation 7). Producer's accuracy is actually measure the omission errors and can tell us from the perspective of the map maker how accurate is the map (Story and Congalton 1986).

$$X = \frac{a_1}{a_1 + a_4 + a_7} \tag{7}$$

Table 9. An example of confusion matrix

		Reference Data		
		X	Y	Z
Classified Data	X	a_1	a_2	a_3
	Y	a_4	a_5	a_6
	Z	a_7	a_8	a_9

2. User's accuracy: user's accuracy for category X can be calculated as correctly classified samples of category X divided by the total number of samples that were classified to category X (equation 8). User's accuracy is actually measure the commission error and can tell us from the perspective of the map user how accurate is the map (Story and Congalton 1986).

$$X = \frac{a_1}{a_1 + a_2 + a_3} \tag{8}$$

3. Hellden's Mean Accuracy Index (Hellden): Hellden's mean accuracy index (Helldén 1980; Rosenfield and Fitzpatrick-Lins 1986) for category X is calculated as:

$$X = \frac{2a_1}{(a_1 + a_2 + a_3) + (a_1 + a_4 + a_7)} \tag{9}$$

Hellden's mean accuracy index is the harmonic mean of producer's and user's accuracy (Turk 2002; Liu, Frazier and Kumar 2007).

4. Short's Mean Accuracy Index (Short): Short's mean accuracy index (Short 1982) for category X is calculated as:

$$X = \frac{a_1}{(a_1 + a_2 + a_3) + (a_1 + a_4 + a_7) - a_1} \quad (10)$$

Short's mean accuracy index is similar to Hellden's mean accuracy index, and it's a monotonic function of the harmonic mean of producer's and user's accuracy (Liu et al. 2007).

5. Kappa Index of Agreement (KIA): Kappa index of agreement is first introduced by Cohen (1960), and represent the proportion of agreement after chance agreement is removed. Calculation of the KIA is explained in detailed in Liu et al. (2007).

4.5. Using Automated Local Thresholding Method to Extract Scroll Bar

ImageJ is an open source image processing program designed for scientific multidimensional images (ImageJ 2018a). Automated local threshold plugin inside ImageJ can transform 8-bit images into binary images using various local threshold methods. Local thresholding meaning the threshold is computed for each pixel within a window of radius r around it (ImageJ 2018b). There are currently nine methods available in this plugin:

1. Bernsen: This method is introduced by Bernsen (1986). If local contrast (max-min) is equal or larger than 15, threshold will be set to local mid-grey value (mean of the minimum and maximum grey values in a user defined area). If the local contrast is less than 15, pixel value of the output binary image will be set to white or black depending on the value of mid-grey (Sezgin and Sankur 2004).

2. Contrast: based on contrast, the pixel value of the output binary image will be set to white (pixel value 255) if current value is closer to local maximum in a calculation window defined by the user. Pixel value will be set to black (pixel value 0) if current value is closer to local minimum (Soille 2013).

3. Mean: this method selects the mean of the local greyscale distribution as the threshold, pixel value of the output binary image will be set to white or black depending on whether current value is larger or smaller than the mean.

4. Median: this method selects the median of the local greyscale distribution as the threshold, pixel value of the output binary image will be set to white or black depending on whether current value is larger or smaller than the median.

5. MidGrey: this method selects the mid-grey of the local greyscale distribution ((min+max)/2) as the threshold, pixel value of the output binary image will be set to white or black depending on whether current value is larger or smaller than the mid-grey value.

6. Niblack: this method is introduce by Niblack (1986).

$$\text{Threshold} = \text{mean} + k * \text{standard\_deviation} \tag{11}$$

K is 0.2 and -0.2 for bright, dark object. Pixel value of the output binary image will be set to white or black depending on whether current value is larger or smaller than the threshold value calculated based on user defined window.

7. Otsu: this method is introduce by Otsu (1979). This method searches for one threshold that will minimize the intra-class variance, which is calculated as the weighted sum of the variances of two classes.

8. Phansalkar: this method is introduce by Phansalkar et al. (2011). It's an adaptation of Sauvola's method aim to process images with low contrast.

$$\text{Threshold} = \text{mean}*(1 + p* \exp(- q*\text{mean}) + k*(\left(\frac{\text{stdev}}{r}\right) - 1) \tag{12}$$

In here, mean and stdev are the local mean and standard deviation in a user defined window. K = 0.25, r = 0.5, p = 2 and q = 10 is recommended by the Phansalkar.

9. Sauvola: this method is introduce by Sauvola and Pietikäinen (2000). It's an adaptation of Niblack's method.

$$\text{Threshold} = \text{mean}*\left(1 + k*\left(\frac{\text{stdev}}{r} - 1 \right) \right) \quad (13)$$

In here, k = 0.5 and r = 128 is recommended by Sauvola.

Strick (2016) implemented automated local threshold algorithm in his research of floodplain geomorphology and topography. Specifically, he used this method on LiDAR DEM to generate a binary image of the scroll bar, segmented the scroll bar into two classes, scroll bar ridge are treated as binary "foreground" (white) and scroll bar swale are treated as binary "background" (black) (Strick et al. 2018). In the paper, the conclusion is drawn that Niblack method is best method for his study area and most suitable window size is 100m.

In our study, we intend to experiment all nine automated local threshold methods to two scroll bar rich areas within our floodplain study site. We first digitized all the visible scroll bar ridge and scroll bar swale of our two chosen study areas in ArcMap 10.5 to be used as a reference in the later accuracy assessment. Strick (2016) use radius range between 50m and 200m at 5m interval in his trials in seek optimal local window radius. In our study, since we use SRTM DEM which has much coarser spatial resolution than the LiDAR DEM used by Strick, hence we first adopted a range of 30m, 60m, 90m, 120m, 150m, 180m, 210m, 240m, 270m and 300m (1 to 10 times pixel size) as radius and used those radius setting in our first trial on study area 1 using Niblack method. Based on the visual examination, we found radius ranges between 150m to 270m trend to generate better segmentation result than other radius settings. Then we adopted this new

radius setting: 150m, 180m, 210m, 240m and 270m which corresponding to five to nine times pixel size (30m) of the SRTM DEM used in our study. We use those radius settings on nine auto local threshold methods to our study sites and then compare the resulting binary images showing segmented scroll bar ridges and scroll bar swales to our reference data for an accuracy assessment.

5. RESULT AND DISCUSSION

5.1. Segmentation Result

In object-based image classification, the prerequisite of a decent classification result is a decent image segmentation result as input layer. In order to derive an optimal segmentation result, we proposed 15 trials with each trial utilize different weighting scheme for the segmentation input layer and different scale parameter as indicated in previous section (Table 7). Scale parameter determines the average size of the output image objects in the multiresolution segmentation. In our study, we choose three different scale: 10, 20 and 30 to investigate which scale is the most suitable for our application. Sample segmentation images showing the effect of using different scale parameter to the same study area is shown in Figure 7. From the example, it's clear that high scale parameter will yield to large image objects and low scale parameter will yield to small image objects.

Optimal segmentation result should be a reflection of real-world objects. In our study, we want to select those segmentation results which can accurately delineate objects from our eight land-cover and geomorphic classes. Therefore, 60 percent of reference regions (Table 5) for each land-cover and geomorphic class were randomly selected and compared to the segmentation result from our proposed 15 trials. Calculation of the following indices were conducted in ArcMap 10.6 using a Python script wrote by the author.

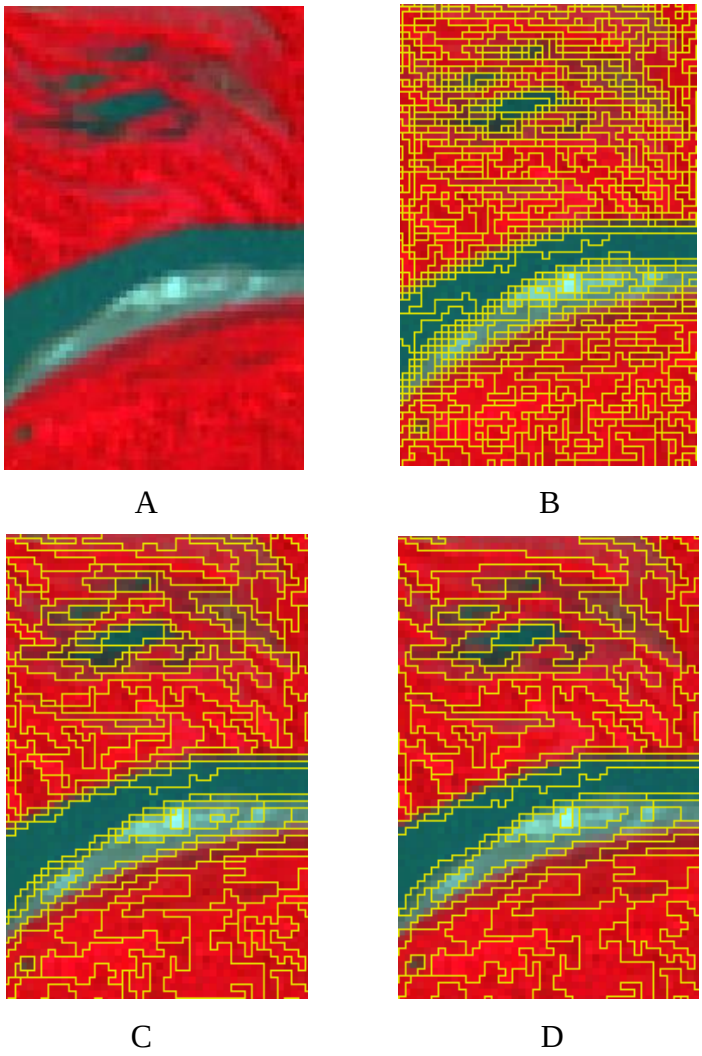

Figure 7. An example of segmented image using different scale parameter. A. False color composite image of Landsat 7 ETM+. B. Scale parameter = 10. C. Scale parameter = 20. D. Scale parameter = 30.

5.1.1. Index 1: Percentage of the Area of the Largest Sub-object

As can be observed from Table 10, the average area percentage of the largest sub-object has a trend to increase when scale parameter increased from 10 to 30. This is because when scale

Table 10. Percentage of the area of the largest sub-object (indicator of over-segmentation)

Scale Parameter	Trial NO.	River	Oxbow Lake (Bright)	Oxbow Lake (Dark)	Sand Bar (Bright)	Sand Bar (Dark)	Scroll Bar Ridge	Scroll Bar Swale	Non Forest Vegetation	Bare Soil	Average
	1	7.51%	10.90%	13.29%	10.88%	18.08%	13.45%	15.98%	7.94%	10.78%	12.09%
	2	9.49%	14.73%	16.20%	11.57%	19.46%	15.95%	19.50%	9.41%	11.36%	14.19%
10	3	8.59%	13.65%	12.91%	11.46%	18.15%	14.32%	16.48%	8.47%	11.73%	12.86%
	4	9.42%	14.57%	16.64%	12.01%	20.74%	16.54%	21.24%	10.67%	12.48%	14.92%
	5	10.91%	14.40%	15.63%	12.85%	20.04%	17.51%	20.81%	9.72%	13.81%	15.08%
	6	22.12%	23.59%	28.80%	22.59%	35.33%	15.04%	30.82%	20.12%	21.78%	24.47%
	7	25.70%	28.21%	36.63%	25.34%	39.99%	13.03%	32.92%	20.94%	21.93%	27.19%
20	8	23.04%	24.70%	30.27%	24.12%	37.59%	15.39%	31.97%	21.59%	22.51%	25.69%
	9	25.35%	30.80%	37.38%	28.37%	41.64%	13.83%	32.48%	22.01%	23.81%	28.41%
	10	26.02%	30.58%	31.49%	29.40%	40.25%	13.83%	34.07%	22.49%	25.67%	28.20%
	11	31.16%	36.18%	48.76%	36.86%	46.00%	8.08%	29.89%	28.83%	30.76%	32.95%
	12	33.26%	41.80%	44.62%	44.48%	54.35%	9.39%	28.50%	33.49%	29.72%	35.51%
30	13	35.74%	37.23%	51.68%	41.33%	45.75%	6.04%	28.50%	30.98%	31.45%	34.30%
	14	36.59%	43.26%	46.96%	45.18%	55.62%	7.74%	22.24%	36.75%	30.47%	36.09%
	15	37.23%	40.74%	50.81%	43.51%	46.01%	5.69%	23.14%	33.43%	36.26%	35.20%

parameter is set to 10, the image is being divided into finer parts, and since the reference object are the same, there will be more image objects inside one reference object compare to segmentation image using larger scale parameter. We can also observe different land-cover and geomorphic classes have different area percentage. When the scale parameter is set to 30, we can see oxbow lake, sand bar has largest average area percentage of the largest sub-object, which is around 40% to 50%. River, non-forest vegetation and bare soil classes have lower average area percentage around 30%, while scroll bar has a lowest average area percentage. This trend is also observable when scale parameter is set to 10 and 20.

For an ideal segmentation, the percentage of the area of the largest sub-object should be high, which indicates the over-segmentation of the reference object is low. So, we can conclude from the calculation of this index that segmentation result is better to delineate the shape of oxbow lake and sand bar while not so accurately delineate the shape of the scroll bar.

5.1.2. Index 2: Percentage of the Area of the Lost Pixels

As can be observed from Table 11, the average area percentage of the lost pixel also has a trend to increase when scale parameter increased from 10 to 30. Different land-cover and geomorphic classes also have different area percentage. When the scale parameter is set to 30, we can see both bright and dark oxbow lake classes have the lowest area percentage, around 6%, while bright sand bar and bare soil has the second lowest area percentage. River, dark sand bar and non-forest vegetation has average area percentage of around 20% while scroll bar ridge class has the highest area percentage. This trend is also observable when scale parameter is set to 10 and 20.

Table 11. Percentage of the area of lost pixels (indicator of under-segmentation)

Scale Parameter	Trial NO.	River	Oxbow Lake (Bright)	Oxbow Lake (Dark)	Sand Bar (Bright)	Sand Bar (Dark)	Scroll Bar Ridge	Scroll Bar Swale	Non-Forest Vegetation	Bare Soil	Average
10	1	5.96%	3.79%	4.35%	8.59%	13.29%	38.35%	23.18%	11.31%	7.09%	12.88%
10	2	7.42%	3.75%	4.15%	8.40%	13.09%	45.38%	24.75%	13.33%	7.08%	14.15%
10	3	6.33%	3.81%	4.24%	8.42%	13.35%	41.55%	24.29%	12.18%	7.16%	13.48%
10	4	6.93%	3.68%	4.09%	8.28%	13.13%	47.64%	26.46%	13.04%	7.64%	14.54%
10	5	5.92%	3.73%	4.19%	8.36%	13.71%	44.22%	25.07%	13.00%	7.89%	14.01%
20	6	10.35%	4.53%	4.34%	9.19%	19.38%	74.08%	39.26%	15.76%	13.57%	21.16%
20	7	11.43%	5.06%	4.90%	10.22%	19.21%	80.96%	44.68%	22.70%	13.75%	23.66%
20	8	10.98%	4.82%	4.45%	9.57%	19.29%	77.60%	40.50%	17.32%	13.13%	21.96%
20	9	12.21%	5.12%	5.33%	9.56%	19.40%	81.07%	46.41%	23.38%	15.99%	24.28%
20	10	9.67%	5.11%	5.14%	9.63%	20.06%	81.13%	43.82%	20.29%	12.72%	23.06%
30	11	20.85%	5.92%	6.91%	10.82%	22.09%	89.90%	51.78%	22.44%	14.57%	27.25%
30	12	18.31%	5.86%	7.55%	10.68%	25.04%	88.96%	59.53%	24.96%	18.34%	28.80%
30	13	18.29%	6.15%	6.84%	10.58%	21.93%	91.73%	55.87%	22.28%	15.39%	27.67%
30	14	17.49%	5.89%	7.83%	11.18%	24.12%	90.86%	66.57%	23.08%	22.59%	29.96%
30	15	20.84%	6.08%	6.88%	12.32%	28.22%	92.72%	64.91%	24.55%	12.33%	29.87%

For an ideal segmentation, the percentage of the area of the lost pixels should be low, which indicated the under-segmentation of the reference object is low. So, we can conclude from the calculation of this index that segmentation result is better to delineate the shape of oxbow lake, bright sand bar and bare soil while not so accurately delineate the shape of the scroll bar ridge.

5.1.3. Index 3: Percentage of the Area of the Extra Pixels

As can be observed from Table 12, the average area percentage of the lost pixel still has a trend to increase when scale parameter increased from 10 to 30. However, the trend is not as steep as can been seen in previous two indices. Different land-cover and geomorphic classes also have different area percentage while the range is also not as large as previous result. When the scale parameter is set to 30, we can see scroll bar ridge class have the lowest area percentage, around 4% while oxbow lake class has area percentage of 6.5%. River, bright sand bar and scroll bar swale classes has an area percentage of 11% while dark sand bar and non-forest vegetation has the highest area percentage of around 17.5%.

For an ideal segmentation, the percentage of the area of the extra pixels should also be low, which is another indicator that the under-segmentation of the reference object is low. So, we can conclude from the calculation of this index that segmentation result is better to delineate the shape of scroll bar ridge and oxbow lake while not so accurately delineate the shape of the dark sand bar and non-forest vegetation.

5.1.4. Index 4: Count of Deformed Area Due to Lost Pixels

Index 4 calculated the number of reference objects which lost more than 25 percent of the pixels. As can be observed from Table 13, the total number of deformed objects is increasing as the scale parameter increases.

Table 12. Percentage of the area of extra pixels (indicator of under-segmentation)

Scale Parameter	Trial NO.	River	Oxbow Lake (Bright)	Oxbow Lake (Dark)	Sand Bar (Bright)	Sand Bar (Dark)	Scroll Bar Ridge	Scroll Bar Swale	Non-Forest Vegetation	Bare Soil	Average
10	1	4.28%	4.23%	4.77%	6.71%	9.62%	17.77%	15.24%	8.87%	6.44%	8.66%
10	2	5.02%	4.41%	5.14%	7.13%	10.23%	17.20%	17.72%	8.98%	7.33%	9.24%
10	3	4.56%	4.29%	4.92%	7.05%	9.96%	17.54%	16.29%	8.95%	6.96%	8.95%
10	4	5.59%	4.62%	5.33%	7.42%	10.46%	18.13%	17.55%	9.78%	7.17%	9.56%
10	5	5.06%	4.51%	5.14%	7.36%	10.20%	18.95%	18.33%	9.58%	7.27%	9.60%
20	6	7.54%	5.36%	6.44%	9.59%	13.35%	11.48%	17.68%	15.71%	9.03%	10.69%
20	7	8.85%	5.44%	7.14%	9.19%	14.34%	6.67%	17.08%	12.90%	10.62%	10.25%
20	8	7.47%	5.34%	6.71%	9.75%	13.99%	10.21%	17.61%	14.94%	9.99%	10.67%
20	9	10.11%	5.59%	7.12%	9.45%	14.49%	6.63%	16.55%	13.54%	9.19%	10.29%
20	10	10.03%	5.39%	6.69%	9.97%	15.21%	7.74%	17.34%	14.08%	11.06%	10.84%
30	11	10.87%	5.67%	6.52%	10.71%	18.58%	4.03%	15.36%	16.54%	12.50%	11.20%
30	12	11.57%	6.09%	7.33%	11.41%	17.52%	5.12%	11.13%	18.73%	12.47%	11.26%
30	13	12.11%	5.98%	6.68%	11.29%	18.75%	3.50%	13.87%	17.09%	13.43%	11.41%
30	14	12.93%	6.38%	7.24%	11.14%	17.35%	4.10%	9.01%	19.72%	11.14%	11.00%
30	15	12.39%	6.36%	7.18%	11.37%	15.43%	3.54%	9.27%	16.53%	15.61%	10.85%

When scale parameter is set to 10, we can see deformed objects are mainly in the scroll bar ridge and scroll bar swale classes. Non-forest vegetation class also shows a few deformed objects. When scale parameter is set to 20, deformed objects in scroll bar ridge and scroll bar swale class are slowly increasing, we can also see deformed objects in non-forest vegetation, bare soil and dark sand bar classes in small quantities. When scale parameter is set to 30, in addition to the aforementioned observation, deformed objects begin to show in the river class.

5.1.5. Index 5: Count of Deformed Area Due to Extra Pixels

Index 5 calculated the number of reference objects which gained more than 25 percent of the pixels. As can be observed from Table 14, the total number of deformed objects do not have a clear trend to increase or decrease as the scale parameter increases. When scale parameter is set to 10, we can see deformed objects are mainly in the scroll bar swale, non-forest vegetation and bare soil classes. Deformed objects are also presented in dark sand bar, scroll bar ridge, bright sand bar and river class in small quantities. When scale parameter increased to 20, we can observe that number of deformed objects in scroll bar ridge and scroll bar swale classes increased while the number of deformed objects in dark sand bar, bright sand bar, non-forest vegetation, bare soil and river classes all declined to 0. When scale parameter increased to 30, we can see deformed objects are still mainly in scroll bar ridge and scroll bar swale class. Deformed objects reappeared in the dark sand bar, non-forest vegetation and bare soil classes while none or few deformed objects can be seen in these classes when scale parameter is set to 20.

Table 13. Count of deformed areas due to lost pixels

Scale Parameter	Trial NO.	River	Oxbow Lake (Bright)	Oxbow Lake (Dark)	Sand Bar (Bright)	Sand Bar (Dark)	Scroll Bar Ridge	Scroll Bar Swale	Non-Forest Vegetation	Bare Soil	Ratio
10	1	0	0	0	0	0	22	13	2	1	19.49%
10	2	0	0	0	0	0	24	13	3	0	20.51%
10	3	0	0	0	0	0	24	14	3	1	21.54%
10	4	0	0	0	0	0	24	16	3	0	22.05%
10	5	0	0	0	0	0	24	14	3	1	21.54%
20	6	0	0	0	0	3	30	18	4	5	30.77%
20	7	0	0	0	1	3	29	22	8	4	34.36%
20	8	0	0	0	0	3	30	20	7	4	32.82%
20	9	0	0	0	0	3	29	21	9	5	34.36%
20	10	0	0	0	0	3	29	20	9	4	33.33%
30	11	4	0	0	0	3	30	20	11	4	36.92%
30	12	2	0	0	0	6	29	24	8	6	38.46%
30	13	3	0	0	0	2	30	21	11	4	36.41%
30	14	2	0	0	1	4	30	25	7	7	38.97%
30	15	5	0	0	1	4	29	24	13	3	40.51%

Table 14. Count of deformed areas due to extra pixels

Scale Parameter	Trial NO.	River	Oxbow Lake (Bright)	Oxbow Lake (Dark)	Sand Bar (Bright)	Sand Bar (Dark)	Scroll Bar Ridge	Scroll Bar Swale	Non-Forest Vegetation	Bare Soil	Ratio
10	1	0	0	0	0	2	1	6	5	3	8.72%
10	2	0	0	0	0	1	3	4	9	5	11.28%
10	3	2	0	0	1	2	1	6	5	3	10.26%
10	4	0	0	0	1	1	2	4	9	3	10.26%
10	5	1	0	0	1	2	2	3	6	4	9.74%
20	6	0	0	0	0	0	4	3	0	0	3.59%
20	7	0	0	0	0	0	4	8	0	1	6.67%
20	8	0	0	0	0	0	3	3	0	1	3.59%
20	9	0	0	0	0	0	6	6	0	1	6.67%
20	10	0	0	0	0	0	8	7	0	0	7.69%
30	11	0	0	0	0	0	6	6	3	1	8.21%
30	12	0	0	0	0	0	1	6	2	4	6.67%
30	13	0	0	0	0	1	4	5	3	2	7.69%
30	14	0	0	0	0	1	1	7	3	2	7.18%
30	15	0	0	0	0	2	3	5	2	3	7.69%

5.1.6. Segmentation Result Selection

In above sections, we examined the performance of each segmentation trial by looking at the five indices calculated based on the comparison between the reference objects and segmented land cover and geomorphic classes. We can observe that segmentation result demonstrates different level of delineation details for each land cover and geomorphic classes. Judging by the result summarized from Table 10 to Table 14, we can see bright oxbow lake, dark oxbow lake classes have the highest segmentation performance and bright sand bar and dark sand bar classes has second highest segmentation performance. This is due to those classes has specific spectral signature and clear object boundary. River class has slightly lower performance at large scale because surface reflectance variance within river class is small, so the segmented objects of river class tend to have larger size (Figure 7) which may not align well with our smaller reference river object. Non-forest vegetation and bare-soil classes have moderate performance. Scroll bar ridges and scroll bar swales has the lowest performance largely due to land cover above those geomorphic objects. Scroll bar ridges is usually covered with forest or non-forest vegetation while scroll bar swales is usually covered in bare soil or water during the rainy season. This will limit the ability of the segmentation algorithm to differentiate them from neighboring landforms. Also due to the coarse resolution (30m) of the Landsat ETM+ image and DEM, small scroll bar and scroll bar ridges used as reference regions may not pick up by the segmentation algorithm.

In order to find optimal segmentation result to be used as input layer in the classification process, we have to compare overall segmentation performance for all classes. We evaluated the average accuracy for each trial and summarized the best trials for each scale in Table 15. We can conclude trial 1 and trial 6 are the optimal segmentation results for scale 10 and scale 20. Situation

for scale 30 is a bit complicated because different between trials is not significant. Since both trial 1 and trial 6 share a common layer weighting, we intend to follow the same layer weighting for scale 30, so in the end trial 11 was chosen to be the optimal trial for scale 30.

Table 15. Selection of the optimal segmentation trial

	Optimal Segmentation Trail NO. (Scale = 10)	Optimal Segmentation Trail NO. (Scale = 20)	Optimal Segmentation Trail NO. (Scale = 30)
Index 1	5	9	14
Index 2	1	6	11
Index 3	1	7	15
Index 4	1	6	13
Index 5	1	6	12

Segmentation result derived from trail 6 and trial 11 were used in the classification process. Segmentation result derived from trial 1 was not used because under further examination, segmented objects are too small and many objects only consists one pixel which contradict the purpose of object-based analysis.

5.2. Classification Result

5.2.1. Overall Classification Accuracy

The accuracy assessment result of the classified map is summarized in Table 16. Both overall accuracy and Kappa Index of Agreement (KIA) were calculated for 24 trials. Overall accuracy ranges from 0.5522 to 0.8852 while KIA ranges from 0.4417 to 0.8539.

Table 16. Classification accuracy result for proposed 24 trials

Trial NO.	Overall Accuracy	KIA	Trial NO.	Overall Accuracy	KIA
Trial 01	0.6377	0.5405	Trial 13	0.5522	0.4417
Trial 02	0.8845	0.8526	Trial 14	0.8721	0.8368
Trial 03	0.8813	0.8485	Trial 15	0.8756	0.8415
Trial 04	0.8846	0.8527	Trial 16	0.8719	0.8368
Trial 05	0.5602	0.4515	Trial 17	0.6272	0.5272
Trial 06	0.8852	0.8539	Trial 18	0.8725	0.8372
Trial 07	0.8794	0.8466	Trial 19	0.8717	0.8362
Trial 08	0.8828	0.8510	Trial 20	0.8736	0.8386
Trial 09	0.6272	0.5272	Trial 21	0.5522	0.4417
Trial 10	0.8725	0.8372	Trial 22	0.8721	0.8368
Trial 11	0.8717	0.8362	Trial 23	0.8756	0.8415
Trial 12	0.8736	0.8386	Trial 24	0.8719	0.8368

If we sort those accuracy values in an ascending order as shown in Table 17, those values can be roughly divided into two groups. Trial 13, 21, 05, 09, 17 and 01 can be grouped into group one and the rest 18 trials can be grouped into group two. Overall accuracy of group one ranges from 0.5522 to 0.6377 while the overall accuracy of the group two ranges from 0.8717 to 0.8852. The lowest overall accuracy of 0.5522 comes from trial 13, which only used Landsat image in the classification process and its segmentation input layer is based on Landsat image and detrended DEM at scale 30. The highest overall accuracy of 0.8852 comes from trial 06, which use Landsat and EVI images in the classification process and its segmentation input layer is based on Landsat only at scale 30.

Table 17. Classification trials sorted by overall accuracy in an ascending order. (DDEM = Detrended DEM)

Low to High	Trial NO.	Overall Accuracy	KIA	Segmentation Layers		Scale	Classification Layers			
1	13	0.5522	0.4417	Landsat	DDEM	30	Landsat	-	-	-
2	21	0.5522	0.4417	Landsat	DDEM	30	Landsat	DDEM	-	-
3	05	0.5602	0.4515	Landsat	-	30	Landsat	-	-	-
4	09	0.6272	0.5272	Landsat	DDEM	20	Landsat	-	-	-
5	17	0.6272	0.5272	Landsat	DDEM	20	Landsat	DDEM	-	-
6	01	0.6377	0.5405	Landsat	-	20	Landsat	-	-	-
7	11	0.8717	0.8362	Landsat	DDEM	20	Landsat	NDWI	-	-
8	19	0.8717	0.8362	Landsat	DDEM	20	Landsat	NDWI	DDEM	-
9	16	0.8719	0.8368	Landsat	DDEM	30	Landsat	EVI	NDWI	-
10	24	0.8719	0.8368	Landsat	DDEM	30	Landsat	EVI	NDWI	DDEM
11	14	0.8721	0.8368	Landsat	DDEM	30	Landsat	EVI	-	-
12	22	0.8721	0.8368	Landsat	DDEM	30	Landsat	EVI	DDEM	-
13	10	0.8725	0.8372	Landsat	DDEM	20	Landsat	EVI	-	-
14	18	0.8725	0.8372	Landsat	DDEM	20	Landsat	EVI	DDEM	-
15	12	0.8736	0.8386	Landsat	DDEM	20	Landsat	EVI	NDWI	-
16	20	0.8736	0.8386	Landsat	DDEM	20	Landsat	EVI	NDWI	DDEM
17	15	0.8756	0.8415	Landsat	DDEM	30	Landsat	NDWI	-	-
18	23	0.8756	0.8415	Landsat	DDEM	30	Landsat	NDWI	DDEM	-
19	07	0.8794	0.8466	Landsat	-	30	Landsat	NDWI	-	-
20	03	0.8813	0.8485	Landsat	-	20	Landsat	NDWI	-	-
21	08	0.8828	0.8510	Landsat	-	30	Landsat	EVI	NDWI	-
22	02	0.8845	0.8526	Landsat	-	20	Landsat	EVI	-	-
23	04	0.8846	0.8527	Landsat	-	20	Landsat	EVI	NDWI	-
24	06	0.8852	0.8539	Landsat	-	30	Landsat	EVI	-	-

By looking closely at group one in Table 17, we can see despite the segmentation layer used in those trials is different, layers used in classification is either Landsat image only or the combination of the Landsat image and detrended DEM. It's clear from the statistical standpoint, using Landsat image or using Landsat image plus detrended DEM in the classification process does not help to achieve high classification accuracy.

If we examine group two closely, we can see from the statistic standpoint, segmentation layer that is derive from Landsat image is performed better than segmentation layer derived using Landsat image and detrended DEM (trial 07, 03, 08, 02, 04 and 06 versus other trials in the group two). When compare different layers used in the classification process, we can conclude that using Landsat image and EVI can achieve highest overall classification accuracy. Moreover, we can see using the combination of the Landsat image and EVI layer, combination of Landsat image with EVI and NDWI layer, combination of Landsat image with NDWI layer in the classification process can all achieve high overall classification accuracy. Introducing detrended DEM to those combination does not benefit from achieving higher overall accuracy.

Classification map of the Río Beni floodplain showing all eight land cover and geomorphic classes are illustrated in Figure 8. Classification result used here is from trial 06, which has the highest overall accuracy among 24 trials. Classification accuracy for each land cover and geomorphic class will be discussed in next section.

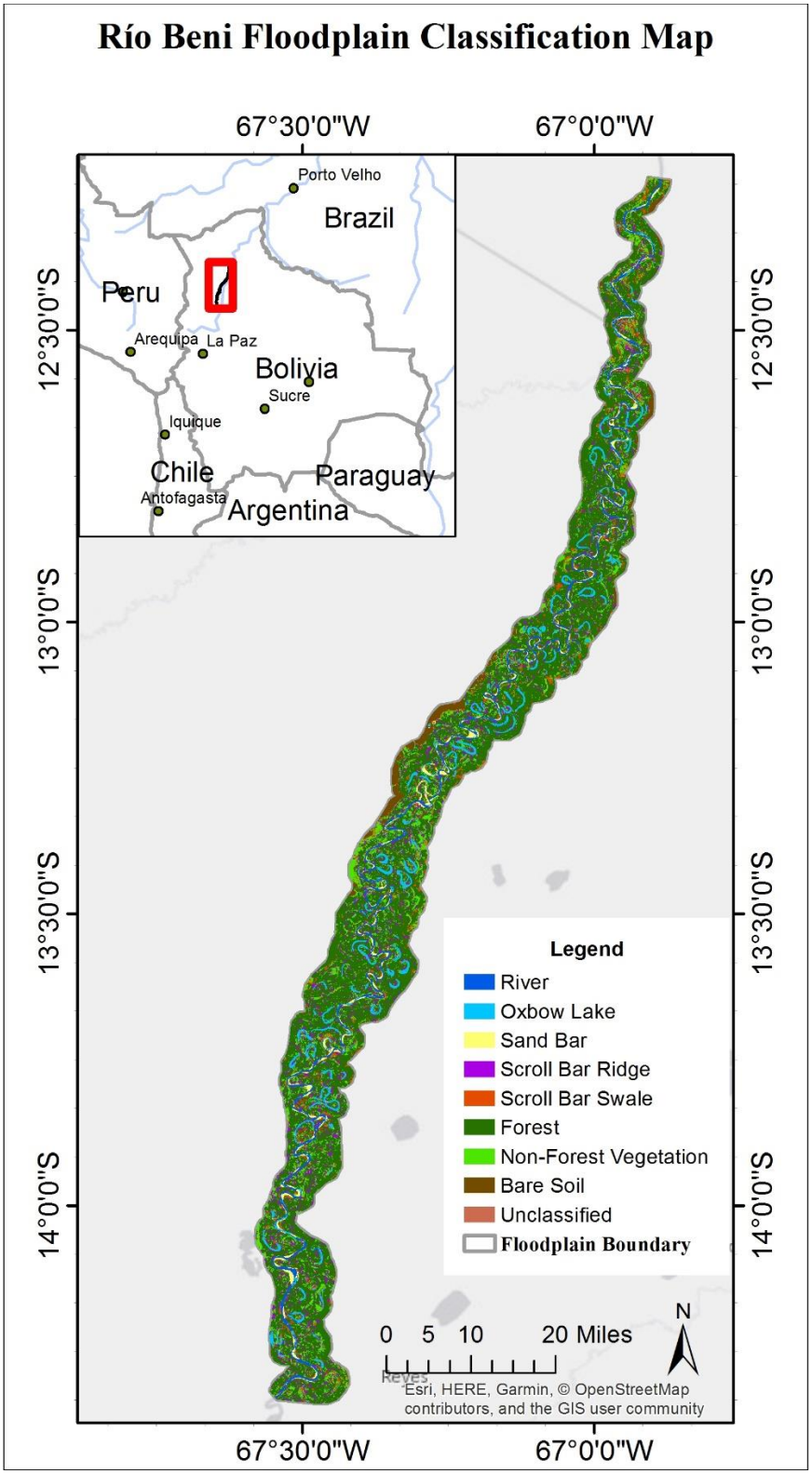

Figure 8. Río Beni floodplain classification map

5.2.2. Classification Accuracy Result by Land Cover and Geomorphic Classes

5.2.2.1. River

The accuracy assessment result for the river class is summarized in Table 18. Five accuracy assessment metrics: producer's accuracy, user's accuracy, Hellden's Mean Accuracy Index (Hellden), Short's Mean Accuracy Index (Short) and Kappa Index of Agreement (KIA) were calculated for 24 trials. Producer's accuracy ranges from 0.5522 to 0.9132, user's accuracy ranges from 0.5385 to 0.9482, Hellden's mean accuracy index ranges from 0.5708 to 0.9205, Short's mean accuracy index ranges from 0.3994 to 0.8527 and KIA ranges from 0.4269 to 0.8868.

Similar to the overall accuracy, those 24 trials can be grouped into two groups. Group one consists trial 09, 17, 13, 21, 05, 01 and all the rest can be grouped into group two. Producer's and user's accuracy for group one ranges from 0.5522 to 0.6442 and from 0.5385 to 0.5907 respectively. On the other hand, producer's and user's accuracy for group two ranges from 0.8363 to 0.9132 and from 0.9164 to 0.9482 respectively.

The lowest producer's accuracy of 0.5522 comes from trial 09, which only used Landsat image in the classification process and its segmentation input layer is based on Landsat image and detrended DEM at scale 20. The highest producer's accuracy of 0.9132 comes from trial 08, which use Landsat image, EVI and NDWI layers in the classification process and its segmentation input layer is based on Landsat only at scale 30.

Table 18. River classification accuracy sorted by producer's accuracy in an ascending order

Order	Trial NO.	Producer	User	Hellden	Short	KIA	Segmentation Layers		Scale	Classification Layers			
1	09	0.5522	0.5907	0.5708	0.3994	0.4269	Landsat	DDEM	20	Landsat	-	-	-
2	17	0.5522	0.5907	0.5708	0.3994	0.4269	Landsat	DDEM	20	Landsat	DDEM	-	-
3	13	0.5969	0.5650	0.5805	0.4089	0.4646	Landsat	DDEM	30	Landsat	-	-	-
4	21	0.5969	0.5650	0.5805	0.4089	0.4646	Landsat	DDEM	30	Landsat	DDEM	-	-
5	05	0.6297	0.5385	0.5805	0.4090	0.4903	Landsat	-	30	Landsat	-	-	-
6	01	0.6442	0.5818	0.6114	0.4403	0.5198	Landsat	-	20	Landsat	-	-	-
7	14	0.8363	0.9376	0.8840	0.7922	0.7931	Landsat	DDEM	30	Landsat	EVI	-	-
8	22	0.8363	0.9376	0.8840	0.7922	0.7931	Landsat	DDEM	30	Landsat	EVI	DDEM	-
9	10	0.8512	0.9379	0.8924	0.8057	0.8111	Landsat	DDEM	20	Landsat	EVI	-	-
10	18	0.8512	0.9379	0.8924	0.8057	0.8111	Landsat	DDEM	20	Landsat	EVI	DDEM	-
11	16	0.8535	0.9289	0.8896	0.8012	0.8134	Landsat	DDEM	30	Landsat	EVI	NDWI	-
12	24	0.8535	0.9289	0.8896	0.8012	0.8134	Landsat	DDEM	30	Landsat	EVI	NDWI	DDEM
13	11	0.8577	0.9357	0.8950	0.8099	0.8188	Landsat	DDEM	20	Landsat	NDWI	-	-
14	19	0.8577	0.9357	0.8950	0.8099	0.8188	Landsat	DDEM	20	Landsat	NDWI	DDEM	-
15	12	0.8583	0.9394	0.8970	0.8133	0.8198	Landsat	DDEM	20	Landsat	EVI	NDWI	-
16	20	0.8583	0.9394	0.8970	0.8133	0.8198	Landsat	DDEM	20	Landsat	EVI	NDWI	DDEM
17	15	0.8693	0.9274	0.8974	0.8139	0.8326	Landsat	DDEM	30	Landsat	NDWI	-	-
18	23	0.8693	0.9274	0.8974	0.8139	0.8326	Landsat	DDEM	30	Landsat	NDWI	DDEM	-
19	02	0.8895	0.9482	0.9179	0.8483	0.8585	Landsat	-	20	Landsat	EVI	-	-
20	04	0.8935	0.9425	0.9173	0.8473	0.8631	Landsat	-	20	Landsat	EVI	NDWI	-
21	06	0.8950	0.9357	0.9149	0.8432	0.8647	Landsat	-	30	Landsat	EVI	-	-
22	03	0.8991	0.9429	0.9205	0.8527	0.8702	Landsat	-	20	Landsat	NDWI	-	-
23	07	0.9078	0.9164	0.9121	0.8383	0.8800	Landsat	-	30	Landsat	NDWI	-	-
24	08	0.9132	0.9175	0.9153	0.8439	0.8868	Landsat	-	30	Landsat	EVI	NDWI	-

The lowest user's accuracy of 0.5385 comes from trial 05, which only used Landsat image in the classification process and its segmentation input layer is based on Landsat image only at scale 30. The highest user's accuracy of 0.9482 comes from trial 02, which use Landsat image and EVI layer in the classification process and its segmentation input layer is based on Landsat only at scale 20.

Based on the performance of the 24 trials using producer's accuracy and user's accuracy, we can derive similar conclusion from the analysis of the overall accuracy assessment:

1. Using Landsat image alone or with detrended DEM in the classification process does not generate satisfactory classification accuracy for the river class.
2. Trials that using the segmentation layer derived from Landsat image and using either the combination of the Landsat image and EVI layer, the combination of Landsat image with EVI and NDWI layer, the combination of Landsat image with NDWI layer in the classification process can all achieve high overall classification accuracy for river class.
3. Based on the result of the user's accuracy, trials using segmentation layer with scale parameter 20 trends to have better user's accuracy than those trials use segmentation layer with scale parameter 30. This trend is not observed in the producer's accuracy result.

A map showing the classified river class (derived from trial 08) of the Río Beni floodplain is depicted in Figure 9. Visual comparison between the classified river class and Landsat 7 ETM+ image indicates a good match along the river channel. However, we can also observe that part of the oxbow lakes are misclassified as river in the output.

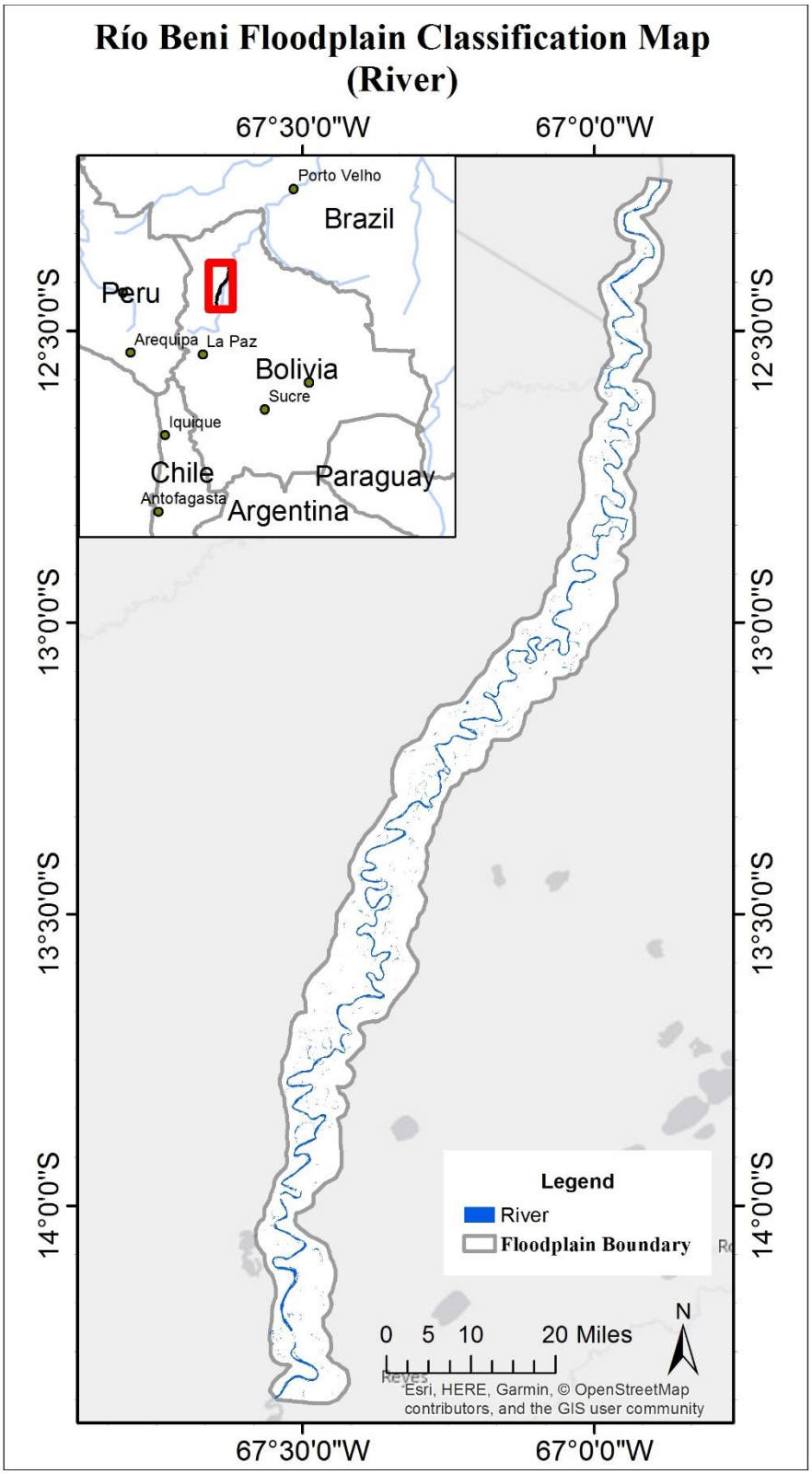

Figure 9. Río Beni floodplain classification map for river class

5.2.2.2. Oxbow Lake

The accuracy assessment result for the oxbow class is summarized in Table 19. Producer's accuracy ranges from 0.5593 to 0.9690, user's accuracy ranges from 0.6721 to 0.9377, Hellden's mean accuracy index ranges from 0.6230 to 0.9445, Short's mean accuracy index ranges from 0.4524 to 0.8948 and KIA ranges from 0.4242 to 0.9550.

Grouping phenomenon can still be observed in the result. Producer's and user's accuracy for group one ranges from 0.5593 to 0.6848 and from 0.6721 to 0.7030 respectively. On the other hand, producer's and user's accuracy for group two ranges from 0.9374 to 0.9690 and from 0.8884 to 0.9377 respectively.

The lowest producer's accuracy of 0.5593 comes from trial 05, which only used Landsat image in the classification process and its segmentation input layer is based on Landsat image only at scale 30. The highest producer's accuracy of 0.9690 comes from trial 02, which use Landsat image and EVI layer in the classification process and its segmentation input layer is based on Landsat only at scale 20.

The lowest user's accuracy of 0.6721 comes from trial 09, which only used Landsat image in the classification process and its segmentation input layer is based on Landsat image and detrended DEM at scale 20. The highest user's accuracy of 0.9377 comes from trial 08, which use Landsat image, EVI and NDWI layers in the classification process and its segmentation input layer is based on Landsat only at scale 20.

Table 19. Oxbow lake classification accuracy sorted by producer's accuracy in an ascending order

Order	Trial NO.	Producer	User	Hellden	Short	KIA	Segmentation Layers		Scale	Classification Layers			
1	05	0.5593	0.7030	0.6230	0.4524	0.4242	Landsat	-	30	Landsat	-	-	-
2	13	0.6181	0.6753	0.6454	0.4765	0.4768	Landsat	DDEM	30	Landsat	-	-	-
3	21	0.6181	0.6753	0.6454	0.4765	0.4768	Landsat	DDEM	30	Landsat	DDEM	-	-
4	01	0.6181	0.6879	0.6511	0.4827	0.4804	Landsat	-	20	Landsat	-	-	-
5	09	0.6848	0.6721	0.6784	0.5133	0.5493	Landsat	DDEM	20	Landsat	-	-	-
6	17	0.6848	0.6721	0.6784	0.5133	0.5493	Landsat	DDEM	20	Landsat	DDEM	-	-
7	08	0.9374	0.9377	0.9375	0.8824	0.9112	Landsat	-	30	Landsat	EVI	NDWI	-
8	07	0.9380	0.9339	0.9359	0.8795	0.9119	Landsat	-	30	Landsat	NDWI	-	-
9	15	0.9515	0.9108	0.9307	0.8704	0.9299	Landsat	DDEM	30	Landsat	NDWI	-	-
10	23	0.9515	0.9108	0.9307	0.8704	0.9299	Landsat	DDEM	30	Landsat	NDWI	DDEM	-
11	16	0.9519	0.8999	0.9252	0.8607	0.9301	Landsat	DDEM	30	Landsat	EVI	NDWI	-
12	24	0.9519	0.8999	0.9252	0.8607	0.9301	Landsat	DDEM	30	Landsat	EVI	NDWI	DDEM
13	06	0.9574	0.9264	0.9417	0.8898	0.9388	Landsat	-	30	Landsat	EVI	-	-
14	11	0.9603	0.8966	0.9274	0.8646	0.9420	Landsat	DDEM	20	Landsat	NDWI	-	-
15	19	0.9603	0.8966	0.9274	0.8646	0.9420	Landsat	DDEM	20	Landsat	NDWI	DDEM	-
16	14	0.9613	0.8884	0.9234	0.8577	0.9431	Landsat	DDEM	30	Landsat	EVI	-	-
17	22	0.9613	0.8884	0.9234	0.8577	0.9431	Landsat	DDEM	30	Landsat	EVI	DDEM	-
18	12	0.9622	0.8975	0.9287	0.8670	0.9447	Landsat	DDEM	20	Landsat	EVI	NDWI	-
19	20	0.9622	0.8975	0.9287	0.8670	0.9447	Landsat	DDEM	20	Landsat	EVI	NDWI	DDEM
20	10	0.9624	0.8932	0.9265	0.8631	0.9449	Landsat	DDEM	20	Landsat	EVI	-	-
21	18	0.9624	0.8932	0.9265	0.8631	0.9449	Landsat	DDEM	20	Landsat	EVI	DDEM	-
22	03	0.9643	0.9255	0.9445	0.8948	0.9484	Landsat	-	20	Landsat	NDWI	-	-
23	04	0.9645	0.9212	0.9424	0.8910	0.9486	Landsat	-	20	Landsat	EVI	NDWI	-
24	02	0.9690	0.9197	0.9437	0.8934	0.9550	Landsat	-	20	Landsat	EVI	-	-

Based on the performance of the 24 trials using producer's accuracy and user's accuracy, we can see conclusion 1 and 2 derived previously still valid for the oxbow lake class. Although we observed a different pattern for conclusion 3: that is based on the result of the producer's accuracy, trials using segmentation layer with scale parameter 20 trends to have better producer's accuracy than those trials use segmentation layer with scale parameter 30. However, for the user's accuracy, trials using segmentation layer with scale parameter 30 trends to have slightly better accuracy than those trials use segmentation layer with scale parameter 30.

A map showing the classified oxbow lake class (derived from trial 02) of the Río Beni floodplain is depicted in Figure 10. Visual comparison between the classified oxbow lake class and Landsat 7 ETM+ image indicates a good match for most of the oxbow lakes. However, we can also observe that several river segments and isolated water areas are misclassified as oxbow lake in the output.

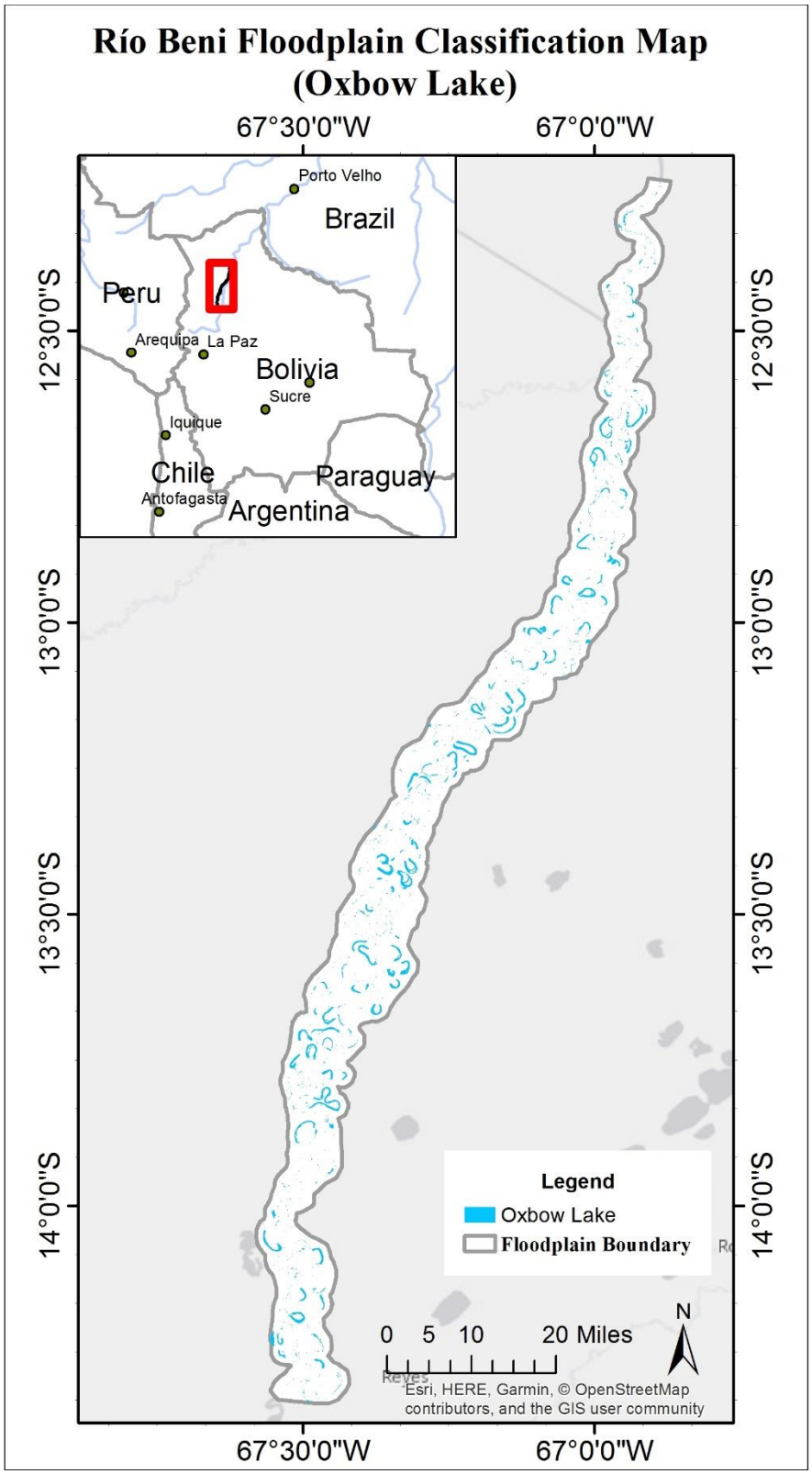

Figure 10. Río Beni floodplain classification map for oxbow lake class

5.2.2.3. Sand Bar

The accuracy assessment result for the sandbar class is summarized in Table 20. Producer's accuracy ranges from 0.4825 to 0.8668, user's accuracy ranges from 0.4513 to 0.8244, Hellden's mean accuracy index ranges from 0.4664 to 0.8433, Short's mean accuracy index ranges from 0.3041 to 0.7291 and KIA ranges from 0.4630 to 0.8618.

Grouping phenomenon can still be observed in the result. Producer's and user's accuracy for group one ranges from 0.4825 to 0.6080 and from 0.4513 to 0.7377 respectively. On the other hand, producer's and user's accuracy for group two ranges from 0.8555 to 0.8668 and from 0.7750 to 0.8244 respectively.

The lowest producer's accuracy of 0.4823 comes from trial 13, which only used Landsat image in the classification process and its segmentation input layer is based on Landsat image and detrended DEM at scale 30. The highest producer's accuracy of 0.8668 comes from trial 20, which use Landsat image, detrended DEM, EVI and NDWI layer in the classification process and its segmentation input layer is based on Landsat only at scale 20.

The lowest user's accuracy of 0.4513 comes from trial 13 as well. The highest user's accuracy of 0.8244 comes from trial 03, which use Landsat image and NDWI layer in the classification process and its segmentation input layer is based on Landsat only at scale 20.

Based on the performance of the 24 trials using producer's accuracy and user's accuracy, we can conclude:

1. Using Landsat image alone or with detrended DEM in the classification process does not generate satisfactory classification accuracy for the sandbar class.

Table 20. Sandbar classification accuracy sorted by producer's accuracy in an ascending order

Order	Trial NO.	Producer	User	Hellden	Short	KIA	Segmentation Layers		Scale	Classification Layers			
1	13	0.4825	0.4513	0.4664	0.3041	0.4630	Landsat	DDEM	30	Landsat	-	-	-
2	21	0.4825	0.4513	0.4664	0.3041	0.4630	Landsat	DDEM	30	Landsat	DDEM	-	-
3	05	0.5441	0.5137	0.5284	0.3591	0.5271	Landsat	-	30	Landsat	-	-	-
4	09	0.5851	0.7377	0.6526	0.4843	0.5736	Landsat	DDEM	20	Landsat	-	-	-
5	17	0.5851	0.7377	0.6526	0.4843	0.5736	Landsat	DDEM	20	Landsat	DDEM	-	-
6	01	0.6080	0.7084	0.6544	0.4863	0.5963	Landsat	-	20	Landsat	-	-	-
7	11	0.8555	0.8215	0.8382	0.7214	0.8502	Landsat	DDEM	20	Landsat	NDWI	-	-
8	19	0.8555	0.8199	0.8373	0.7202	0.8502	Landsat	DDEM	20	Landsat	NDWI	DDEM	-
9	02	0.8579	0.8085	0.8325	0.7130	0.8526	Landsat	-	20	Landsat	EVI	-	-
10	16	0.8592	0.7750	0.8149	0.6876	0.8536	Landsat	DDEM	30	Landsat	EVI	NDWI	-
11	24	0.8592	0.7750	0.8149	0.6876	0.8536	Landsat	DDEM	30	Landsat	EVI	NDWI	DDEM
12	14	0.8604	0.7881	0.8226	0.6987	0.8550	Landsat	DDEM	30	Landsat	EVI	-	-
13	22	0.8604	0.7881	0.8226	0.6987	0.8550	Landsat	DDEM	30	Landsat	EVI	DDEM	-
14	10	0.8612	0.8091	0.8343	0.7157	0.8560	Landsat	DDEM	20	Landsat	EVI	-	-
15	15	0.8612	0.7768	0.8168	0.6903	0.8557	Landsat	DDEM	30	Landsat	NDWI	-	-
16	18	0.8612	0.8075	0.8335	0.7145	0.8560	Landsat	DDEM	20	Landsat	EVI	DDEM	-
17	23	0.8612	0.7768	0.8168	0.6903	0.8557	Landsat	DDEM	30	Landsat	NDWI	DDEM	-
18	04	0.8620	0.8210	0.8410	0.7256	0.8569	Landsat	-	20	Landsat	EVI	NDWI	-
19	07	0.8628	0.8006	0.8305	0.7102	0.8576	Landsat	-	30	Landsat	NDWI	-	-
20	03	0.8632	0.8244	0.8433	0.7291	0.8581	Landsat	-	20	Landsat	NDWI	-	-
21	06	0.8632	0.7998	0.8303	0.7098	0.8580	Landsat	-	30	Landsat	EVI	-	-
22	08	0.8648	0.8004	0.8313	0.7114	0.8596	Landsat	-	30	Landsat	EVI	NDWI	-
23	12	0.8668	0.8089	0.8368	0.7194	0.8618	Landsat	DDEM	20	Landsat	EVI	NDWI	-
24	20	0.8668	0.8089	0.8368	0.7194	0.8618	Landsat	DDEM	20	Landsat	EVI	NDWI	DDEM

2. Different from previous analysis, we can observe that adding the detrended DEM to the segmentation process or the classification process is beneficial to improvement of the classification accuracy (trial 12 and 20).
3. Trials that using the segmentation layer derived from Landsat image and using either the combination of the Landsat image and EVI layer, the combination of Landsat image with EVI and NDWI layer, the combination of Landsat image with NDWI layer in the classification process can all achieve high overall classification accuracy for sanbar class.
4. Based on the result of the user's accuracy, trials using segmentation layer with scale parameter 20 trends to have better user's accuracy than those trials use segmentation layer with scale parameter 30. This trend is not observed in the producer's accuracy result.

A map showing the classified sand bar class (derived from trial 20) of the Río Beni floodplain is depicted in Figure 11. Visual comparison between the classified sand bar class and Landsat 7 ETM+ image indicates the classification result accurately represented the sand bar areas that is observable along the river banks.

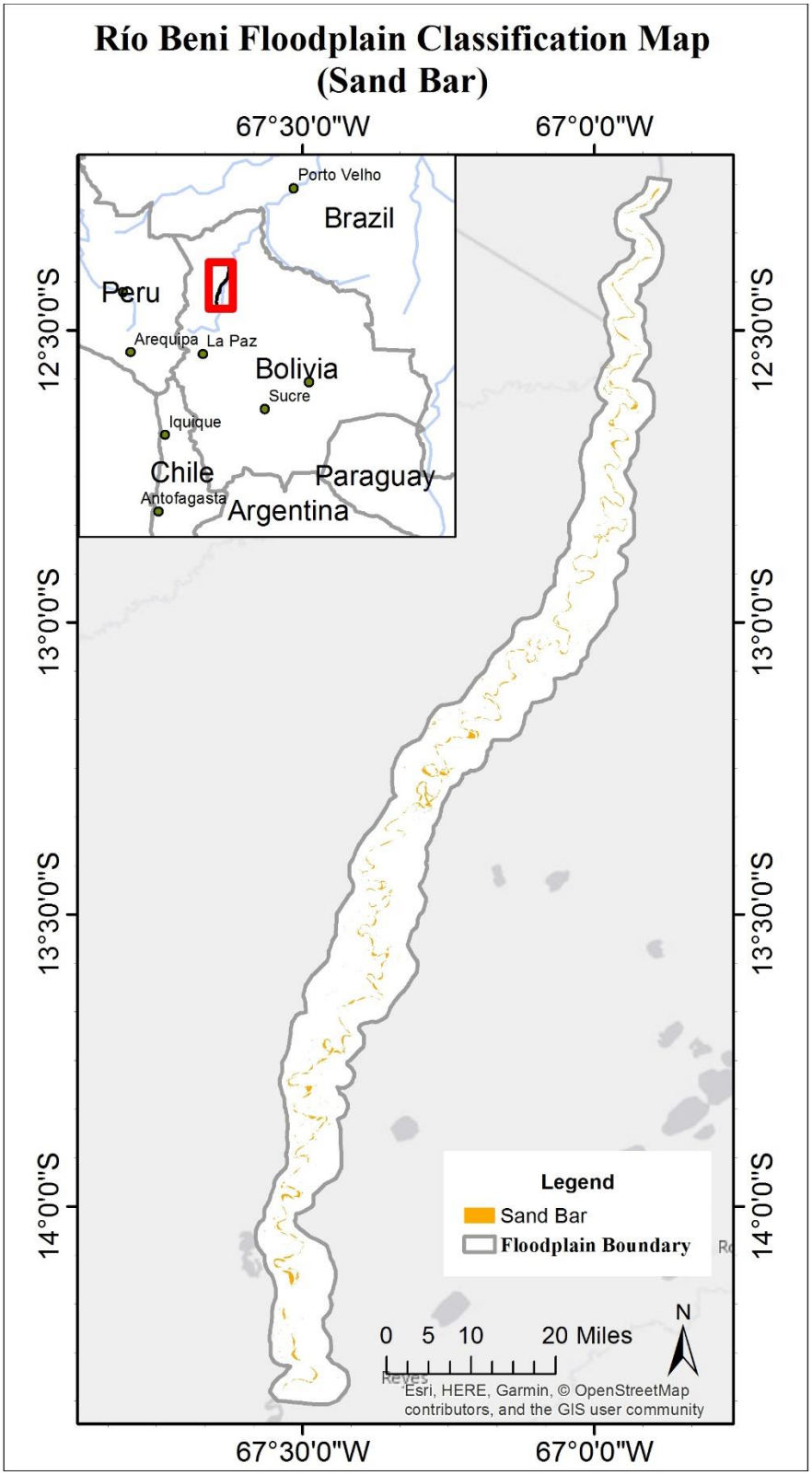

Figure 11. Río Beni floodplain classification map for sand bar class

5.2.2.4. Scroll Bar Ridge and Scroll Bar Swale

The accuracy assessment result for the scrollbar class are summarized in Table 21 and Table 22. For scroll bar ridge class, producer's accuracy ranges from 0.0673 to 0.2885, user's accuracy ranges from 0.0659 to 0.3785, Hellden's mean accuracy index ranges from 0.0666 to 0.3274, Short's mean accuracy index ranges from 0.0344 to 0.1958 and KIA ranges from 0.0481 to 0.2776. For scroll bar swale class, producer's accuracy ranges from 0.1617 to 0.3553, user's accuracy ranges from 0.0989 to 0.4423, Hellden's mean accuracy index ranges from 0.1227 to 0.3899, Short's mean accuracy index ranges from 0.0654 to 0.2422 and KIA ranges from 0.1151 to 0.3377.

Grouping phenomenon can still be observed in the result. For scroll bar ridge class, producer's and user's accuracy for group one ranges from 0.0673 to 0.1692 and from 0.0659 to 0.2105 respectively. On the other hand, producer's and user's accuracy for group two ranges from 0.1699 to 0.2885 and from 0.2714 to 0.3785 respectively. For scroll bar swale class, producer's and user's accuracy for group one ranges from 0.1617 to 0.2088 and from 0.0989 to 0.2277 respectively. On the other hand, producer's and user's accuracy for group two ranges from 0.2958 to 0.3553 and from 0.3823 to 0.4423 respectively.

For scroll bar ridge class, the lowest producer's accuracy of 0.0673 comes from trial 05, which only used Landsat image in the classification process and its segmentation input layer is based on Landsat image only at scale 30. The highest producer's accuracy of 0.2885 comes from trial 06, which use Landsat image and EVI layer in the classification process and its segmentation input layer is based on Landsat only at scale 30.

Table 21. Scrollbar Ridge classification accuracy sorted by producer's accuracy in an ascending order

Order	Trial NO.	Producer	User	Hellden	Short	KIA	Segmentation Layers		Scale	Classification Layers			
1	05	0.0673	0.0659	0.0666	0.0344	0.0481	Landsat	-	30	Landsat	-	-	-
2	13	0.0832	0.1581	0.1090	0.0577	0.0736	Landsat	DDEM	30	Landsat	-	-	-
3	21	0.0832	0.1581	0.1090	0.0577	0.0736	Landsat	DDEM	30	Landsat	DDEM	-	-
4	09	0.0971	0.1212	0.1078	0.0570	0.0826	Landsat	DDEM	20	Landsat	-	-	-
5	17	0.0971	0.1212	0.1078	0.0570	0.0826	Landsat	DDEM	20	Landsat	DDEM	-	-
6	01	0.1692	0.2105	0.1876	0.1035	0.1558	Landsat	-	20	Landsat	-	-	-
7	11	0.1699	0.3043	0.2181	0.1224	0.1607	Landsat	DDEM	20	Landsat	NDWI	-	-
8	19	0.1699	0.3043	0.2181	0.1224	0.1607	Landsat	DDEM	20	Landsat	NDWI	DDEM	-
9	12	0.1824	0.3321	0.2355	0.1334	0.1734	Landsat	DDEM	20	Landsat	EVI	NDWI	-
10	20	0.1824	0.3321	0.2355	0.1334	0.1734	Landsat	DDEM	20	Landsat	EVI	NDWI	DDEM
11	10	0.1872	0.3529	0.2447	0.1394	0.1787	Landsat	DDEM	20	Landsat	EVI	-	-
12	15	0.1872	0.2714	0.2216	0.1246	0.1760	Landsat	DDEM	30	Landsat	NDWI	-	-
13	18	0.1872	0.3529	0.2447	0.1394	0.1787	Landsat	DDEM	20	Landsat	EVI	DDEM	-
14	23	0.1872	0.2714	0.2216	0.1246	0.1760	Landsat	DDEM	30	Landsat	NDWI	DDEM	-
15	04	0.1983	0.3119	0.2425	0.1380	0.1882	Landsat	-	20	Landsat	EVI	NDWI	-
16	02	0.2039	0.3213	0.2495	0.1425	0.1938	Landsat	-	20	Landsat	EVI	-	-
17	03	0.2039	0.3101	0.2460	0.1403	0.1934	Landsat	-	20	Landsat	NDWI	-	-
18	16	0.2101	0.3183	0.2531	0.1449	0.1997	Landsat	DDEM	30	Landsat	EVI	NDWI	-
19	24	0.2101	0.3183	0.2531	0.1449	0.1997	Landsat	DDEM	30	Landsat	EVI	NDWI	DDEM
20	14	0.2247	0.3344	0.2688	0.1552	0.2143	Landsat	DDEM	30	Landsat	EVI	-	-
21	22	0.2247	0.3344	0.2688	0.1552	0.2143	Landsat	DDEM	30	Landsat	EVI	DDEM	-
22	07	0.2774	0.3735	0.3183	0.1893	0.2667	Landsat	-	30	Landsat	NDWI	-	-
23	08	0.2816	0.3701	0.3198	0.1903	0.2706	Landsat	-	30	Landsat	EVI	NDWI	-
24	06	0.2885	0.3785	0.3274	0.1958	0.2776	Landsat	-	30	Landsat	EVI	-	-

Table 22. Scrollbar Swale classification accuracy sorted by producer's accuracy in an ascending order

Order	Trial NO.	Producer	User	Hellden	Short	KIA	Segmentation Layers		Scale	Classification Layers			
1	13	0.1617	0.0989	0.1227	0.0654	0.1151	Landsat	DDEM	30	Landsat	-	-	-
2	21	0.1617	0.0989	0.1227	0.0654	0.1151	Landsat	DDEM	30	Landsat	DDEM	-	-
3	01	0.1744	0.1859	0.1800	0.0989	0.1487	Landsat	-	20	Landsat	-	-	-
4	09	0.1851	0.2026	0.1934	0.1071	0.1604	Landsat	DDEM	20	Landsat	-	-	-
5	17	0.1851	0.2026	0.1934	0.1071	0.1604	Landsat	DDEM	20	Landsat	DDEM	-	-
6	05	0.2088	0.2277	0.2178	0.1222	0.1848	Landsat	-	30	Landsat	-	-	-
7	14	0.2958	0.4043	0.3417	0.2060	0.2789	Landsat	DDEM	30	Landsat	EVI	-	-
8	22	0.2958	0.4043	0.3417	0.2060	0.2789	Landsat	DDEM	30	Landsat	EVI	DDEM	-
9	15	0.3018	0.4155	0.3496	0.2119	0.2851	Landsat	DDEM	30	Landsat	NDWI	-	-
10	23	0.3018	0.4155	0.3496	0.2119	0.2851	Landsat	DDEM	30	Landsat	NDWI	DDEM	-
11	16	0.3065	0.4068	0.3496	0.2118	0.2892	Landsat	DDEM	30	Landsat	EVI	NDWI	-
12	24	0.3065	0.4068	0.3496	0.2118	0.2892	Landsat	DDEM	30	Landsat	EVI	NDWI	DDEM
13	03	0.3272	0.4097	0.3639	0.2224	0.3095	Landsat	-	20	Landsat	NDWI	-	-
14	02	0.3285	0.4351	0.3744	0.2303	0.3118	Landsat	-	20	Landsat	EVI	-	-
15	04	0.3298	0.4382	0.3764	0.2318	0.3132	Landsat	-	20	Landsat	EVI	NDWI	-
16	06	0.3447	0.4423	0.3874	0.2402	0.3278	Landsat	-	30	Landsat	EVI	-	-
17	11	0.3447	0.4070	0.3732	0.2294	0.3263	Landsat	DDEM	20	Landsat	NDWI	-	-
18	19	0.3447	0.4070	0.3732	0.2294	0.3263	Landsat	DDEM	20	Landsat	NDWI	DDEM	-
19	12	0.3463	0.4096	0.3753	0.2310	0.3281	Landsat	DDEM	20	Landsat	EVI	NDWI	-
20	20	0.3463	0.4096	0.3753	0.2310	0.3281	Landsat	DDEM	20	Landsat	EVI	NDWI	DDEM
21	07	0.3489	0.3823	0.3648	0.2231	0.3292	Landsat	-	30	Landsat	NDWI	-	-
22	10	0.3506	0.4151	0.3801	0.2347	0.3324	Landsat	DDEM	20	Landsat	EVI	-	-
23	18	0.3506	0.4151	0.3801	0.2347	0.3324	Landsat	DDEM	20	Landsat	EVI	DDEM	-
24	08	0.3553	0.4321	0.3899	0.2422	0.3377	Landsat	-	30	Landsat	EVI	NDWI	-

For scroll bar swale class, the lowest producer's accuracy of 0.1617 comes from trial 13, which only used Landsat image in the classification process and its segmentation input layer is based on Landsat image and detrended DEM at scale 30. The highest producer's accuracy of 0.3553 comes from trial 08, which use Landsat image, EVI and NDWI layer in the classification process and its segmentation input layer is based on Landsat image only at scale 30.

For scroll bar ridge class, the lowest user's accuracy of 0.0659 comes from trial 05 as well. The highest user's accuracy of 0.3785 comes from trial 06. For scroll bar swale class, the lowest user's accuracy of 0.0989 also comes from trial 13, and the highest user's accuracy of 0.4423 comes from trial 06.

Maps showing the classified scroll bar ridge class (derived from trial 06) and scroll bar swale (derived from trial 08) of the Río Beni floodplain are depicted in Figure 12 and Figure 13. Visual comparison between the classified scroll bar ridge/swale classes and Landsat 7 ETM+ image indicates the classification result unable to accurately extract scroll bar ridges and swales.

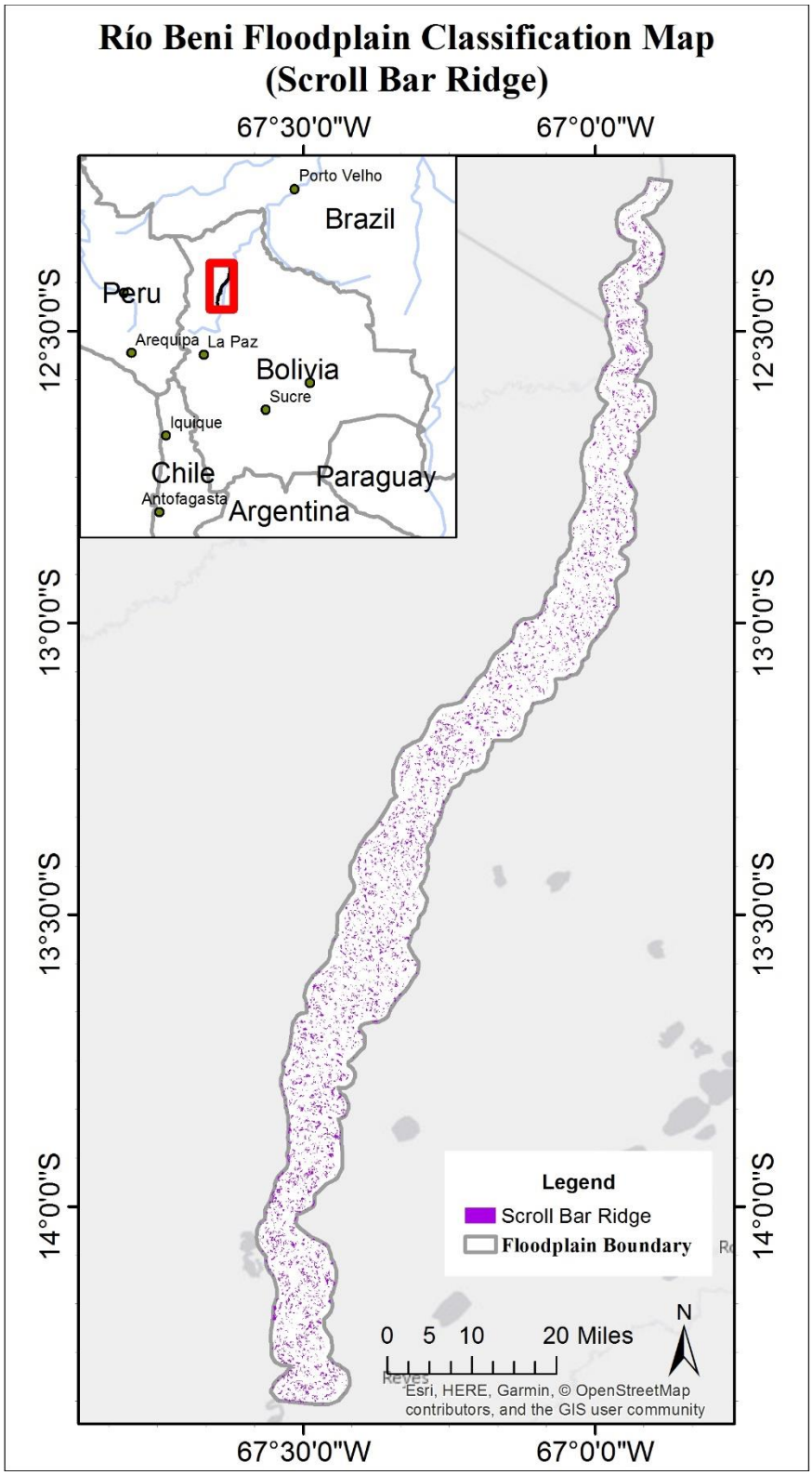

Figure 12. Río Beni floodplain classification map for scroll bar ridge class

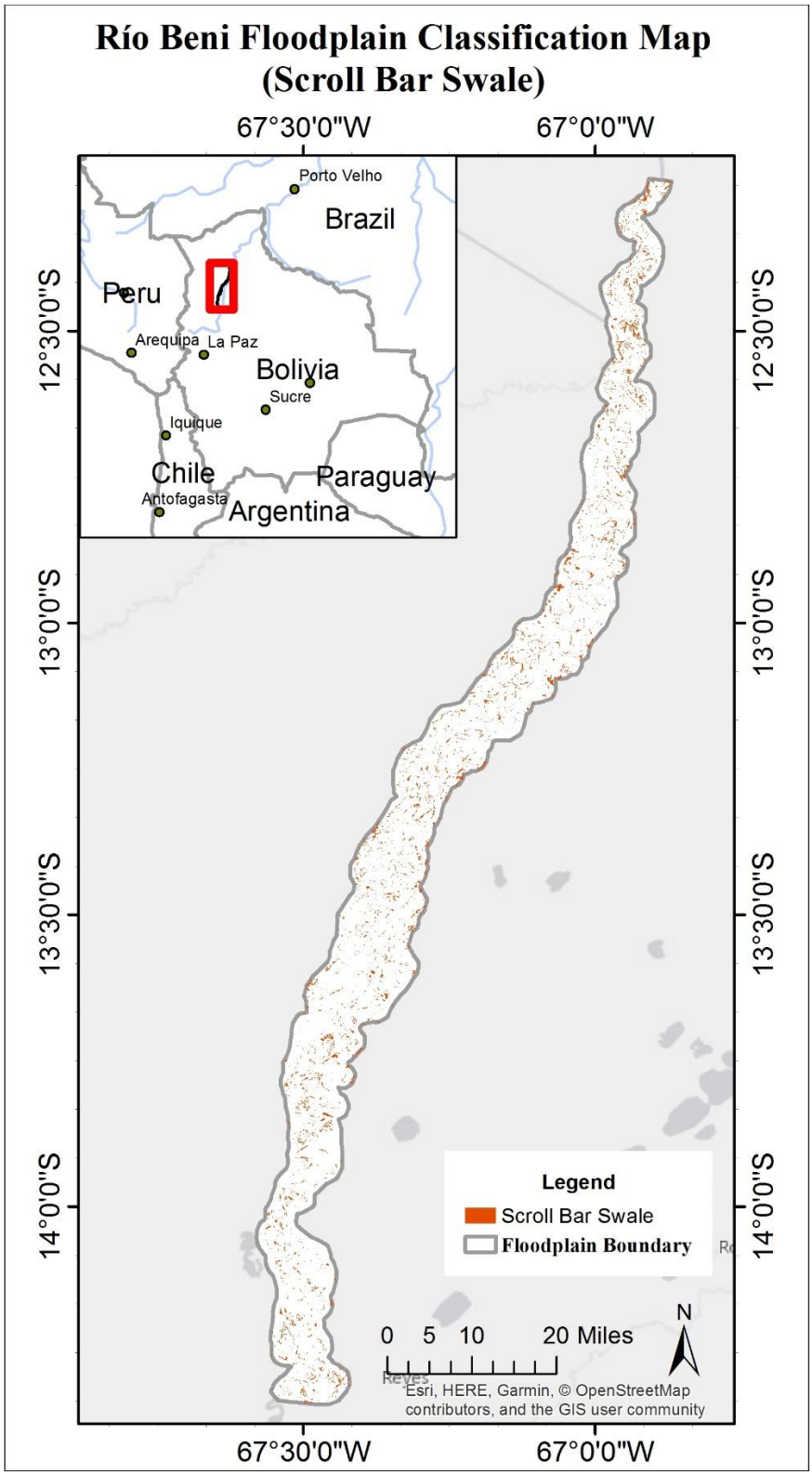

Figure 13. Río Beni floodplain classification map for scroll bar swale class

5.2.2.5. Forest

The accuracy assessment result for the forest class is summarized in Table 23. Producer's accuracy ranges from 0.6219 to 0.9701, user's accuracy ranges from 0.1865 to 0.6002, Hellden's mean accuracy index ranges from 0.2972 to 0.7203, Short's mean accuracy index ranges from 0.1745 to 0.5629 and KIA ranges from 0.5977 to 0.9688.

Grouping phenomenon can still be observed in the result. Producer's and user's accuracy for group one ranges from 0.6219 to 0.7640 and from 0.1865 to 0.2553 respectively. On the other hand, producer's and user's accuracy for group two ranges from 0.8684 to 0.9701 and from 0.5275 to 0.6002 respectively.

The lowest producer's accuracy of 0.6219 comes from trial 01, which only used Landsat image in the classification process and its segmentation input layer is based on Landsat image only at scale 20. The highest producer's accuracy of 0.9701 comes from trial 24, which use Landsat image, detrended DEM, EVI and NDWI layer in the classification process and its segmentation input layer is based on Landsat and detrended DEM at scale 30.

The lowest user's accuracy of 0.1865 comes from trial 05, which only used Landsat image in the classification process and its segmentation input layer is based on Landsat image only at scale 30. The highest user's accuracy of 0.6002 comes from trial 04, which use Landsat image, EVI and NDWI layer in the classification process and its segmentation input layer is based on Landsat only at scale 20.

Based on the performance of the 24 trials using producer's accuracy and user's accuracy, we can conclude:

Table 23. Forest classification accuracy sorted by producer's accuracy in an ascending order

Order	Trial NO.	Producer	User	Hellden	Short	KIA	Segmentation Layers		Scale	Classification Layers			
1	01	0.6219	0.2553	0.3620	0.2210	0.5977	Landsat	-	20	Landsat	-	-	-
2	09	0.6595	0.2300	0.3410	0.2055	0.6335	Landsat	DDEM	20	Landsat	-	-	-
3	17	0.6595	0.2300	0.3410	0.2055	0.6335	Landsat	DDEM	20	Landsat	DDEM	-	-
4	05	0.7308	0.1865	0.2972	0.1745	0.7019	Landsat	-	30	Landsat	-	-	-
5	13	0.7640	0.1889	0.3029	0.1785	0.7377	Landsat	DDEM	30	Landsat	-	-	-
6	21	0.7640	0.1889	0.3029	0.1785	0.7377	Landsat	DDEM	30	Landsat	DDEM	-	-
7	10	0.8684	0.5757	0.6924	0.5295	0.8633	Landsat	DDEM	20	Landsat	EVI	-	-
8	18	0.8684	0.5757	0.6924	0.5295	0.8633	Landsat	DDEM	20	Landsat	EVI	DDEM	-
9	12	0.8695	0.5762	0.6931	0.5303	0.8645	Landsat	DDEM	20	Landsat	EVI	NDWI	-
10	20	0.8695	0.5762	0.6931	0.5303	0.8645	Landsat	DDEM	20	Landsat	EVI	NDWI	DDEM
11	02	0.8740	0.5955	0.7083	0.5484	0.8692	Landsat	-	20	Landsat	EVI	-	-
12	04	0.8773	0.6002	0.7128	0.5537	0.8727	Landsat	-	20	Landsat	EVI	NDWI	-
13	03	0.8795	0.5948	0.7096	0.5499	0.8749	Landsat	-	20	Landsat	NDWI	-	-
14	11	0.8800	0.5745	0.6952	0.5328	0.8753	Landsat	DDEM	20	Landsat	NDWI	-	-
15	19	0.8800	0.5745	0.6952	0.5328	0.8753	Landsat	DDEM	20	Landsat	NDWI	DDEM	-
16	07	0.9420	0.5347	0.6821	0.5176	0.9393	Landsat	-	30	Landsat	NDWI	-	-
17	06	0.9447	0.5275	0.6770	0.5117	0.9422	Landsat	-	30	Landsat	EVI	-	-
18	08	0.9447	0.5317	0.6805	0.5157	0.9422	Landsat	-	30	Landsat	EVI	NDWI	-
19	15	0.9453	0.5627	0.7054	0.5449	0.9429	Landsat	DDEM	30	Landsat	NDWI	-	-
20	23	0.9453	0.5627	0.7054	0.5449	0.9429	Landsat	DDEM	30	Landsat	NDWI	DDEM	-
21	14	0.9701	0.5722	0.7199	0.5623	0.9688	Landsat	DDEM	30	Landsat	EVI	-	-
22	16	0.9701	0.5728	0.7203	0.5629	0.9688	Landsat	DDEM	30	Landsat	EVI	NDWI	-
23	22	0.9701	0.5722	0.7199	0.5623	0.9688	Landsat	DDEM	30	Landsat	EVI	DDEM	-
24	24	0.9701	0.5728	0.7203	0.5629	0.9688	Landsat	DDEM	30	Landsat	EVI	NDWI	DDEM

1. Using Landsat image alone or with detrended DEM in the classification process does not generate satisfactory classification accuracy for the forest class.
2. Adding the detrended DEM to the segmentation process or the classification process is beneficial to the classification accuracy (trial 15, 23, 14, 16, 22 and 24).
3. Using segmentation result at scale 30 will have better producer's accuracy when compared to the trials using segmentation result at scale 20. This trend is inversed in the user's accuracy result.

A map showing the classified forest class (derived from trial 24) of the Río Beni floodplain is depicted in Figure 14. From the map we can observe that most of the study site is covered by forest. Visual comparison between the classified forest class and Landsat Vegetation Continuous Fields (VCF) tree-cover data (Global Land Cover Facility, University of Maryland) indicates a good match over the tree covered area.

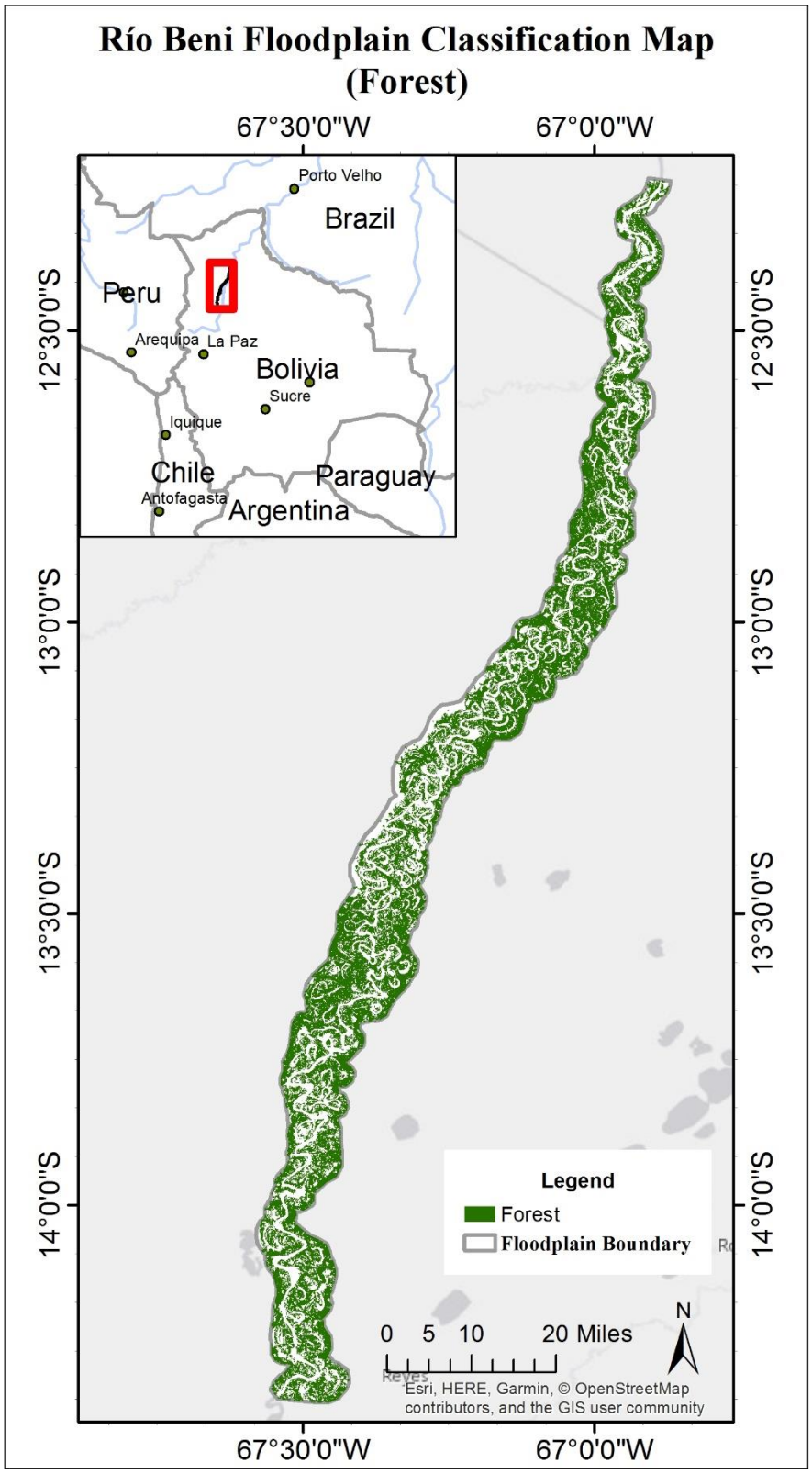

Figure 14. Río Beni floodplain classification map for forest class

5.2.2.6. Non-forest vegetation

The accuracy assessment result for the non-forest vegetation class is summarized in Table 24. Producer's accuracy ranges from 0.4265 to 0.8029, user's accuracy ranges from 0.4732 to 0.8289, Hellden's mean accuracy index ranges from 0.4501 to 0.8072, Short's mean accuracy index ranges from 0.2904 to 0.6767 and KIA ranges from 0.3548 to 0.7740.

Grouping phenomenon can still be observed in the result. Producer's and user's accuracy for group one ranges from 0.4265 to 0.4767 and from 0.4292 to 0.4767 respectively. On the other hand, producer's and user's accuracy for group two ranges from 0.7579 to 0.8029 and from 0.7646 to 0.7834 respectively.

The lowest producer's accuracy of 0.4265 comes from trial 13, which only used Landsat image in the classification process and its segmentation input layer is based on Landsat image and detrended DEM at scale 30. The highest producer's accuracy of 0.8029 comes from trial 04, which use Landsat image, EVI and NDWI layer in the classification process and its segmentation input layer is based on Landsat image only at scale 20.

The lowest user's accuracy of 0.4732 comes from trial 05, which only used Landsat image in the classification process and its segmentation input layer is based on Landsat image only at scale 30. The highest user's accuracy of 0.8289 comes from trial 06, which use Landsat image and EVI layer in the classification process and its segmentation input layer is based on Landsat only at scale 30.

Table 24. Non-forest vegetation classification accuracy sorted by producer's accuracy in an ascending order

Order	Trial NO.	Producer	User	Hellden	Short	KIA	Segmentation Layers		Scale	Classification Layers			
1	13	0.4265	0.5054	0.4626	0.3009	0.3576	Landsat	DDEM	30	Landsat	-	-	-
2	21	0.4265	0.5054	0.4626	0.3009	0.3576	Landsat	DDEM	30	Landsat	DDEM	-	-
3	05	0.4292	0.4732	0.4501	0.2904	0.3548	Landsat	-	30	Landsat	-	-	-
4	09	0.4743	0.5838	0.5234	0.3544	0.4138	Landsat	DDEM	20	Landsat	-	-	-
5	17	0.4743	0.5838	0.5234	0.3544	0.4138	Landsat	DDEM	20	Landsat	DDEM	-	-
6	01	0.4767	0.6134	0.5364	0.3665	0.4193	Landsat	-	20	Landsat	-	-	-
7	07	0.7579	0.8220	0.7886	0.6510	0.7258	Landsat	-	30	Landsat	NDWI	-	-
8	03	0.7646	0.7891	0.7766	0.6348	0.7315	Landsat	-	20	Landsat	NDWI	-	-
9	11	0.7765	0.7926	0.7845	0.6454	0.7447	Landsat	DDEM	20	Landsat	NDWI	-	-
10	19	0.7765	0.7926	0.7845	0.6454	0.7447	Landsat	DDEM	20	Landsat	NDWI	DDEM	-
11	08	0.7803	0.8238	0.8015	0.6687	0.7502	Landsat	-	30	Landsat	EVI	NDWI	-
12	06	0.7834	0.8289	0.8055	0.6743	0.7538	Landsat	-	30	Landsat	EVI	-	-
13	12	0.7850	0.7915	0.7882	0.6505	0.7540	Landsat	DDEM	20	Landsat	EVI	NDWI	-
14	20	0.7850	0.7915	0.7882	0.6505	0.7540	Landsat	DDEM	20	Landsat	EVI	NDWI	DDEM
15	10	0.7898	0.7932	0.7915	0.6550	0.7594	Landsat	DDEM	20	Landsat	EVI	-	-
16	18	0.7898	0.7932	0.7915	0.6550	0.7594	Landsat	DDEM	20	Landsat	EVI	DDEM	-
17	15	0.7913	0.8136	0.8023	0.6699	0.7619	Landsat	DDEM	30	Landsat	NDWI	-	-
18	23	0.7913	0.8136	0.8023	0.6699	0.7619	Landsat	DDEM	30	Landsat	NDWI	DDEM	-
19	16	0.7927	0.8098	0.8012	0.6683	0.7633	Landsat	DDEM	30	Landsat	EVI	NDWI	-
20	24	0.7927	0.8098	0.8012	0.6683	0.7633	Landsat	DDEM	30	Landsat	EVI	NDWI	DDEM
21	14	0.7985	0.8161	0.8072	0.6767	0.7699	Landsat	DDEM	30	Landsat	EVI	-	-
22	22	0.7985	0.8161	0.8072	0.6767	0.7699	Landsat	DDEM	30	Landsat	EVI	DDEM	-
23	02	0.8009	0.7958	0.7983	0.6643	0.7717	Landsat	-	20	Landsat	EVI	-	-
24	04	0.8029	0.7965	0.7997	0.6663	0.7740	Landsat	-	20	Landsat	EVI	NDWI	-

Based on the performance of the 24 trials using producer's accuracy and user's accuracy, we can conclude:

1. Using Landsat image alone or with detrended DEM in the classification process does not generate satisfactory classification accuracy for the non-forest vegetation class.
2. Using the combination of the Landsat image and EVI, the combination of the Landsat image, EVI and NDWI layer in the classification process will achieve the highest classification accuracy for non-forest vegetation class.
3. Using segmentation result at scale 30 will have better user's accuracy when compared to the trials using segmentation result at scale 20. This trend is not observed in the producer's accuracy result.

A map showing the classified non-forest vegetation class (derived from trial 04) of the Río Beni floodplain is depicted in Figure 15. From the map we can observe that non-forest vegetation has a presence over the entire floodplain.

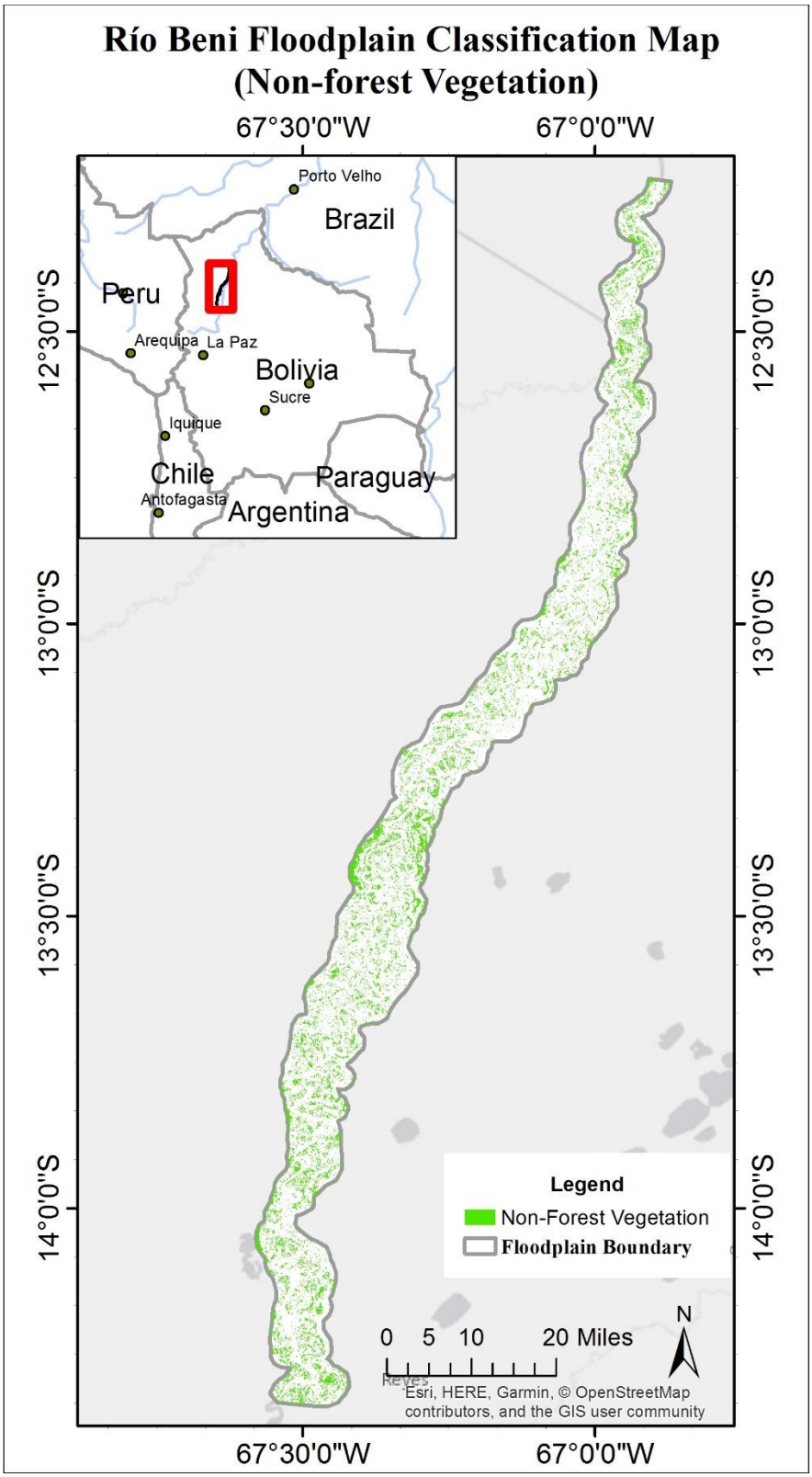

Figure 15. Río Beni floodplain classification map for non-forest vegetation class

5.2.2.7. Bare soil

The accuracy assessment result for the bare soil class is summarized in Table 25. Producer's accuracy ranges from 0.5738 to 0.9639, user's accuracy ranges from 0.7595 to 0.9778, Hellden's mean accuracy index ranges from 0.6537 to 0.9700, Short's mean accuracy index ranges from 0.4855 to 0.9418 and KIA ranges from 0.4825 to 0.9530.

Grouping phenomenon can still be observed in the result. Producer's and user's accuracy for group one ranges from 0.5738 to 0.8529 and from 0.7595 to 0.8234 respectively. On the other hand, producer's and user's accuracy for group two ranges from 0.9571 to 0.9639 and from 0.9525 to 0.9778 respectively.

The lowest producer's accuracy of 0.5738 comes from trial 13, which only used Landsat image in the classification process and its segmentation input layer is based on Landsat image and detrended DEM at scale 30. The highest producer's accuracy of 0.9639 comes from trial 023, which use Landsat image, detrended DEM and NDWI layer in the classification process and its segmentation input layer is based on Landsat image and detrended DEM at scale 30.

The lowest user's accuracy of 0.7595 comes from trial 13 as well. The highest user's accuracy of 0.9778 comes from trial 06, which use Landsat image and EVI layer in the classification process and its segmentation input layer is based on Landsat only at scale 30.

Table 25. Bare soil classification accuracy sorted by producer's accuracy in an ascending order

Order	Trial NO.	Producer	User	Hellden	Short	KIA	Segmentation Layers		Scale	Classification Layers			
1	13	0.5738	0.7595	0.6537	0.4855	0.4825	Landsat	DDEM	30	Landsat	-	-	-
2	21	0.5738	0.7595	0.6537	0.4855	0.4825	Landsat	DDEM	30	Landsat	DDEM	-	-
3	05	0.6372	0.7663	0.6958	0.5335	0.5498	Landsat	-	30	Landsat	-	-	-
4	09	0.8214	0.8177	0.8195	0.6942	0.7666	Landsat	DDEM	20	Landsat	-	-	-
5	17	0.8214	0.8177	0.8195	0.6942	0.7666	Landsat	DDEM	20	Landsat	DDEM	-	-
6	01	0.8529	0.8234	0.8379	0.7210	0.8060	Landsat	-	20	Landsat	-	-	-
7	10	0.9571	0.9653	0.9612	0.9253	0.9442	Landsat	DDEM	20	Landsat	EVI	-	-
8	18	0.9571	0.9653	0.9612	0.9253	0.9442	Landsat	DDEM	20	Landsat	EVI	DDEM	-
9	02	0.9574	0.9635	0.9604	0.9239	0.9445	Landsat	-	20	Landsat	EVI	-	-
10	12	0.9575	0.9654	0.9614	0.9257	0.9447	Landsat	DDEM	20	Landsat	EVI	NDWI	-
11	20	0.9575	0.9654	0.9614	0.9257	0.9447	Landsat	DDEM	20	Landsat	EVI	NDWI	DDEM
12	04	0.9577	0.9637	0.9607	0.9244	0.9449	Landsat	-	20	Landsat	EVI	NDWI	-
13	16	0.9577	0.9674	0.9626	0.9278	0.9450	Landsat	DDEM	30	Landsat	EVI	NDWI	-
14	24	0.9577	0.9674	0.9626	0.9278	0.9450	Landsat	DDEM	30	Landsat	EVI	NDWI	DDEM
15	03	0.9584	0.9525	0.9554	0.9147	0.9456	Landsat	-	20	Landsat	NDWI	-	-
16	08	0.9589	0.9767	0.9677	0.9375	0.9466	Landsat	-	30	Landsat	EVI	NDWI	-
17	11	0.9590	0.9614	0.9602	0.9234	0.9465	Landsat	DDEM	20	Landsat	NDWI	-	-
18	19	0.9590	0.9614	0.9602	0.9234	0.9465	Landsat	DDEM	20	Landsat	NDWI	DDEM	-
19	14	0.9608	0.9696	0.9652	0.9327	0.9490	Landsat	DDEM	30	Landsat	EVI	-	-
20	22	0.9608	0.9696	0.9652	0.9327	0.9490	Landsat	DDEM	30	Landsat	EVI	DDEM	-
21	06	0.9615	0.9778	0.9696	0.9410	0.9501	Landsat	-	30	Landsat	EVI	-	-
22	07	0.9627	0.9774	0.9700	0.9418	0.9516	Landsat	-	30	Landsat	NDWI	-	-
23	15	0.9639	0.9694	0.9667	0.9355	0.9530	Landsat	DDEM	30	Landsat	NDWI	-	-
24	23	0.9639	0.9694	0.9667	0.9355	0.9530	Landsat	DDEM	30	Landsat	NDWI	DDEM	-

Based on the performance of the 24 trials using producer's accuracy and user's accuracy, we can conclude:

1. Using Landsat image alone or with detrended DEM in the classification process does not generate satisfactory classification accuracy for the non-forest vegetation class.
2. Using the combination of the Landsat image, NDWI and detrended DEM, the combination of the Landsat image and NDWI layer in the classification process will achieve the highest classification accuracy for bare soil class.
3. Using segmentation result at scale 30 will have better accuracy when compared to the trials using segmentation result at scale 20.

A map showing the classified bare soil class (derived from trial 23) of the Río Beni floodplain is depicted in Figure 16. From the map we can observe that bare soil class has a presence over the entire floodplain while majority of the bare soil class are located in the floodplain boundary.

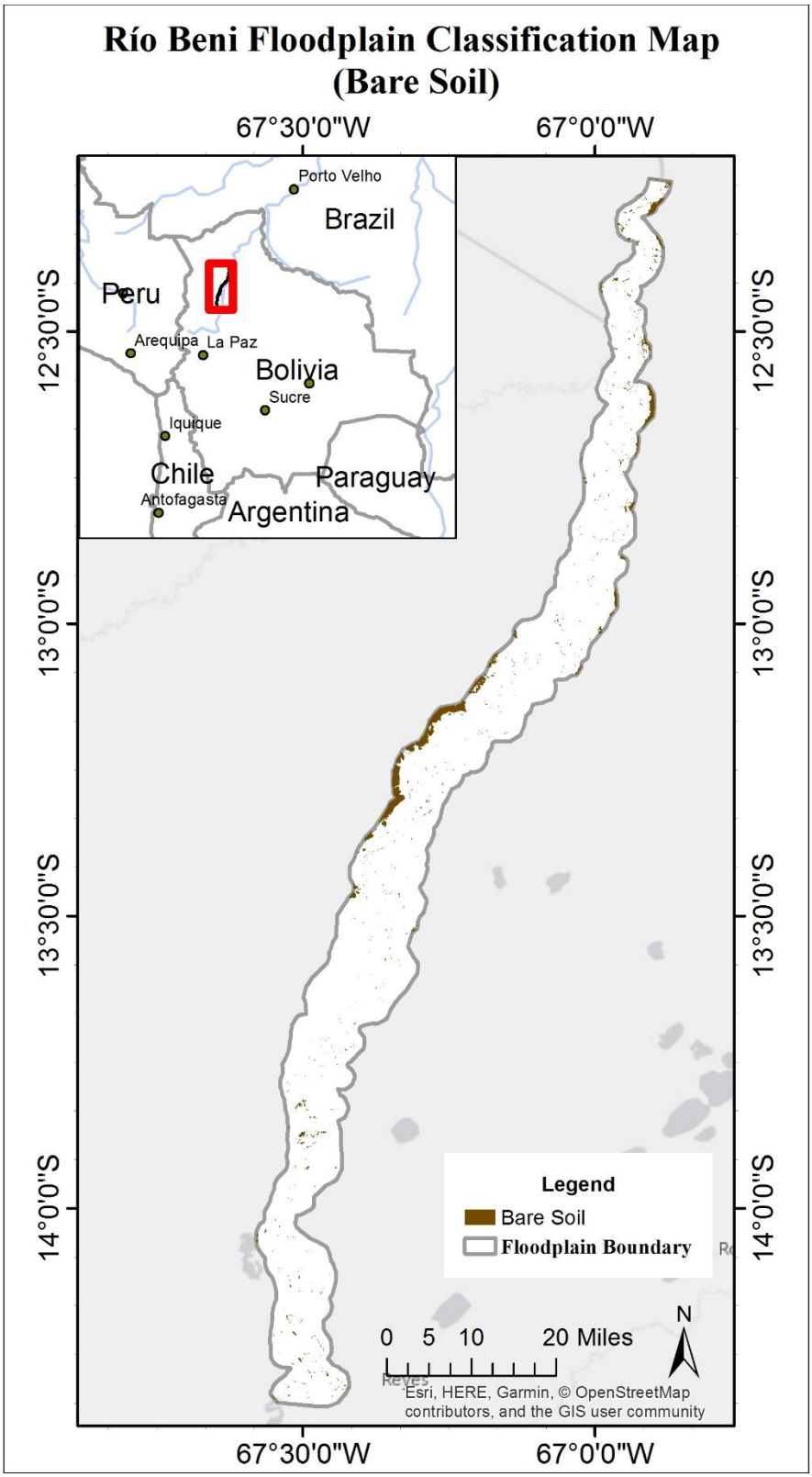

Figure 16. Río Beni floodplain classification map for bare soil class

5.3. Automated Local Threshold Result

Digitized scroll bar ridges and scroll bar swales of our two chosen study areas in our floodplain study site are shown in Figure 17.

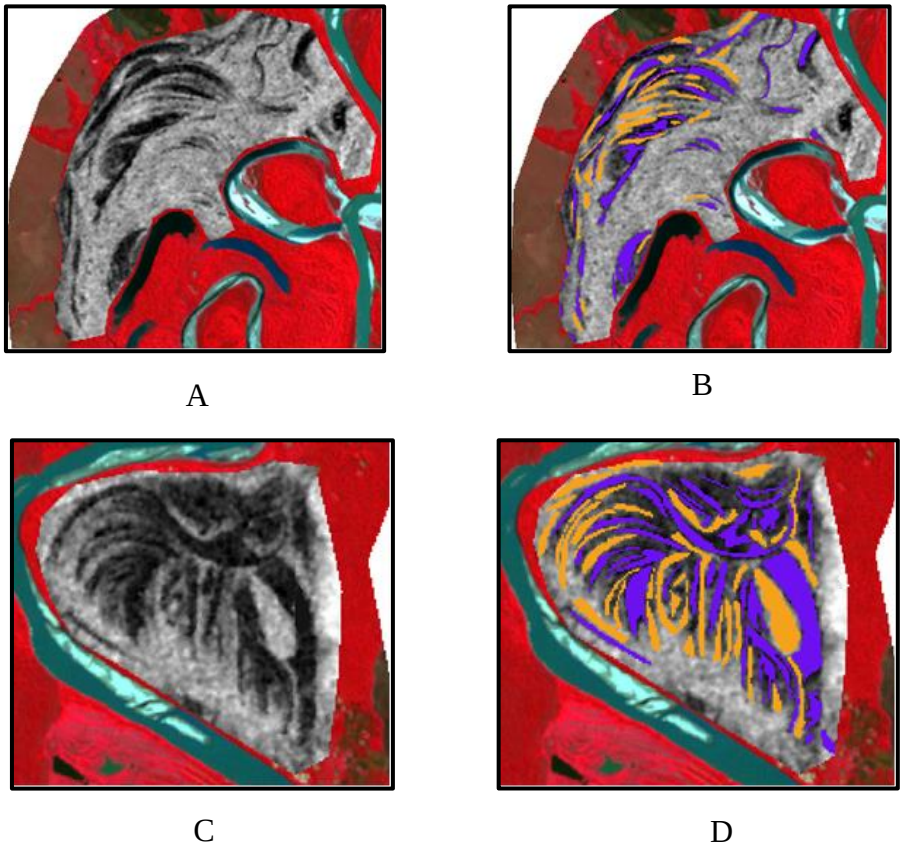

Figure 17. A. Study area 1, superimposed image of SRTM DEM on Landsat false color composite image. B. Study area 1, digitized scroll bar ridges (yellow) and scroll bar swale (purple). C. Study area 2, superimposed image of SRTM DEM on Landsat false color composite image. D. Study area 2, digitized scroll bar ridges (yellow) and scroll bar swale (purple).

Two subsets of SRTM DEM of study area 1 and 2 were processed to derive 8-bit grey scale images, and then were imported to ImageJ software. As indicated in the previous section, all nine automated local threshold methods are used, and we implement each method with different radius settings, ranging from 150m to 270m. 90 trials in total are conducted for study areas 1 and 2; an image showing the segmentation result derived from all nine methods for study area 1, using a radius setting of 150m, is shown in Figure 18.

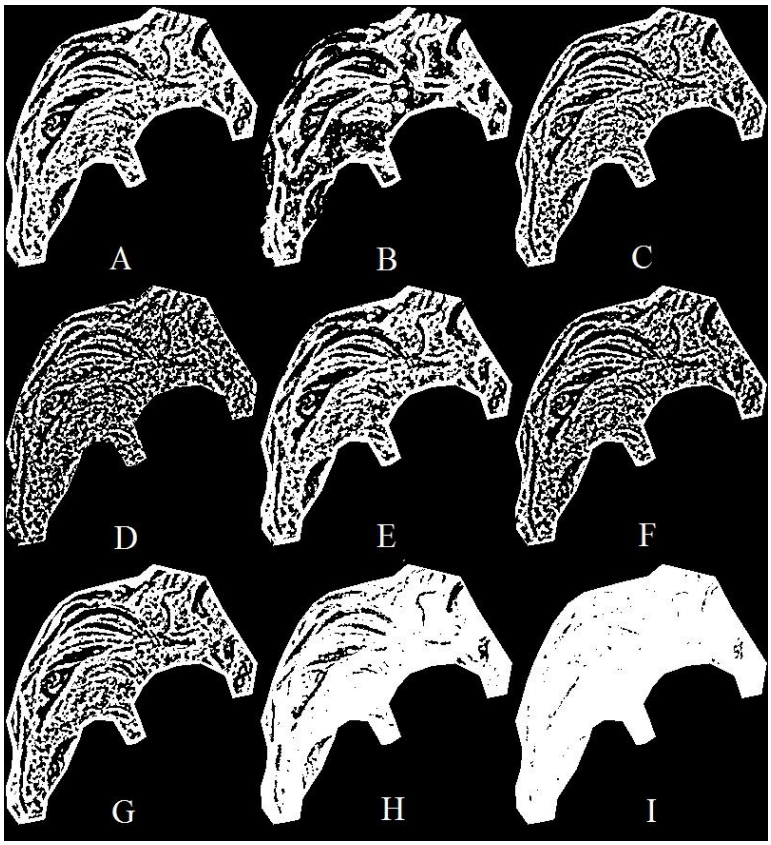

Figure 18. Applying all nine methods on study area 1 with a 150m radius setting. A. Bernsen; B. Contrast; C. Mean; D. Median; E. MidGrey; F. Niblack; G. Otsu; H. Phansalkar; I. Sauvola.

The segmented binary images were then georeferenced and then compare with the digitized scroll bar ridges and swales for accuracy assessment. Accuracy for both ridges and swales were calculated and then arithmetic mean is derived for each trials and the result is summarized in Table 26 and Table 27 for study area 1 and 2.

Table 26. Mean accuracy of scroll bar ridges and swales for study area 1.

Method	Local Window Radius				
	150m	180m	210m	240m	270m
Bernsen	90.70%	91.26%	91.36%	91.18%	90.81%
Contrast	87.14%	89.36%	90.65%	91.30%	91.56%
Mean	89.71%	91.07%	91.48%	91.70%	91.67%
Median	86.60%	88.32%	89.80%	90.92%	91.42%
MidGrey	90.37%	91.13%	91.30%	91.13%	90.77%
Niblack	89.05%	90.25%	90.98%	91.17%	91.34%
Otsu	89.86%	90.76%	90.66%	90.32%	90.26%
Phansalkar	80.66%	83.17%	84.92%	85.94%	86.56%
Sauvola	54.94%	57.50%	60.72%	63.34%	65.43%

Table 27. Mean accuracy of scroll bar ridges and swales for study area 2.

Method	Local Window Radius				
	150m	180m	210m	240m	270m
Bernsen	90.79%	92.10%	93.04%	93.21%	93.30%
Contrast	79.70%	79.98%	79.66%	79.26%	78.78%
Mean	87.45%	89.79%	91.07%	91.90%	92.47%
Median	82.20%	83.90%	85.74%	87.07%	88.04%
MidGrey	90.14%	91.58%	92.65%	92.69%	92.61%
Niblack	85.96%	87.92%	89.56%	90.85%	91.31%
Otsu	89.38%	91.66%	92.66%	93.32%	93.39%
Phansalkar	92.93%	93.47%	93.72%	93.97%	94.14%
Sauvola	61.60%	64.17%	66.88%	69.65%	71.73%

By average those two tables together, we can derive the overall performance assessment for those nine methods used in our two study areas. The result is summarized in Table 28. Based on the result, we can derive the top five trials which has highest accuracy as follow:

1. Using Bernsen's method at radius 210m can achieve an accuracy of 92.20%.
2. Using Bernsen's method at radius 240m can achieve an accuracy of 92.19%.
3. Using Mean method at radius 270m can achieve an accuracy of 92.07%.
4. Using Bernsen's method at radius 270m can achieve an accuracy of 92.06%.
5. Using MidGrey method at radius 210m can achieve an accuracy of 91.98%.

Table 28. Mean accuracy of scroll bar ridges and swales for both study areas.

Method	Local Window Radius				
	150m	180m	210m	240m	270m
Bernsen	90.75%	91.68%	92.20%	92.19%	92.06%
Contrast	83.42%	84.67%	85.16%	85.28%	85.17%
Mean	88.58%	90.43%	91.27%	91.80%	92.07%
Median	84.40%	86.11%	87.77%	88.99%	89.73%
MidGrey	90.26%	91.35%	91.98%	91.91%	91.69%
Niblack	87.51%	89.08%	90.27%	91.01%	91.33%
Otsu	89.62%	91.21%	91.66%	91.82%	91.82%
Phansalkar	86.79%	88.32%	89.32%	89.95%	90.35%
Sauvola	58.27%	60.84%	63.80%	66.50%	68.58%

In Figure 19 we illustrated the result when applying three different method: Bernsen at radius 210m, Mean at radius 270m, MidGrey at radius 210m to study area 1 and 2 and corresponding reference data.

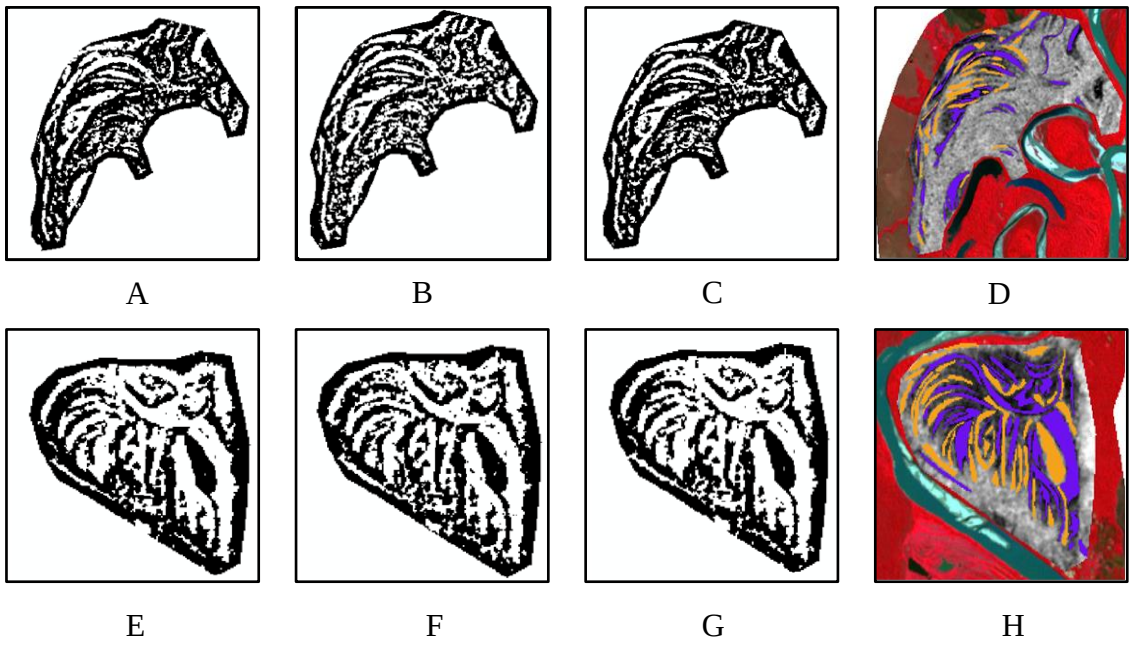

Figure 19. Automated local threshold output in area 1 (A-D) and area 2 (E-H). A. Bernsen, radius =210m; B. Mean, radius=270m; C. MidGrey, radius=210m; D. Digitized ridges and swales; E. Bernsen, radius =210m; F. Mean, radius=270m; G. MidGrey, radius=210m; H. Digitized ridges and swales.

Table 29. Accuracy of the scroll bar segmentation when compared to reference data

Method	Radius (m)	Sroll Bar Swale Accuracy	Scroll Bar Ridge Accuracy	Average Accuracy
Bernsen	210	95.05%	61.76%	78.40%
Mean	270	93.34%	68.70%	81.02%
MidGrey	210	95.58%	59.00%	77.29%

Furthermore, we applied those three methods to our whole floodplain and compared with same reference data of the scroll bar ridges and swale used in the classification accuracy assessment described in previous section, the result is summarized in Table 29. Mean method has

a highest accuracy of 81.02% while Bernsen's method and MidGrey's method has an accuracy of 78.4% and 77.29% respectively.

6. CONCLUSION

In this research we implement GEOgraphic Object-Based Image Analysis on Landsat 7 ETM+ imagery and ancillary datasets in an attempt to classify Río Beni floodplain into eight land cover and geomorphic classes as defined by the author.

Multi-resolution segmentation using Landsat 7 atmospheric corrected surface reflectance image and SRTM DEM is conducted inside eCognition. Segmentation result indicates choosing a weighting scheme of 1:1:1:3:1:1 for Landsat 7 blue, green, red, near-infrared, shortwave infrared 1 and shortwave infrared 2 bands can achieve optimal segmentation result in all three scale (10, 20 and 30). Inclusion of SRTM DEM in the segmentation does not significantly improve the overall accuracy of the segmentation result. We can also observe that segmentation result demonstrates different level of delineation details for each land cover and geomorphic classes. Bright oxbow lake, dark oxbow lake classes have the highest segmentation performance and bright sand bar and dark sand bar classes has second highest segmentation performance. River, non-forest vegetation and bare-soil classes have moderate performance. Scroll bar ridges and scroll bar swales has the lowest performance largely due to land cover above those geomorphic objects, as well as the spatial resolution of the our datasets, limiting the ability of the segmentation algorithm to differentiate them from neighboring objects. Segmentation result of scale 20 and 30 are deemed suitable for our study.

We implemented nearest neighbor classifier in the object-based classification and proposed 24 trials using different combination of segmentation input layers and classification input layers. Overall accuracy ranges from 0.5522 to 0.8852 while Kappa Index of Agreement ranges from 0.4417 to 0.8539. The highest overall accuracy of 0.8852 comes from trial that uses Landsat 7 and

EVI images in the classification process and its segmentation input layer is based on Landsat 7 image only at scale 30. Classification result also showed despite using various segmentation layers, classification trials which use Landsat 7 image only or combination of Landsat 7 and detrended DEM in the classification process trend to have significantly lower accuracy than other dataset combination.

The highest accuracy for each land cover and geomorphic class is listed here: river (91.32%), oxbow lake (96.90%), sandbar (86.68%), scroll bar ridge (28.85%), scroll bar swale (35.53%), forest (97.01%), non-forest vegetation (80.29%) and bare soil (96.39%). Result showed in addition to the Landsat 7 image, NDWI layer is beneficial to the classification of river class, EVI and NDWI layers are beneficial to the classification of oxbow lake and non-forest vegetation class, Detrended DEM is beneficial to the classification of sandbar class, Detrended DEM and NDWI layers are beneficial to the classification of the bare soil class. Result also showed segmentation result with a scale 30 is suitable for the classification of river, scroll bar ridge, forest, bare soil classes, while segmentation result with a scale 20 is more suitable for the classification of oxbow lake, sand bar and non-forest vegetation classes.

In the end, we experimented nine automated local threshold methods to two scroll bar rich areas within our floodplain study site to segment image into scroll bar ridges and scroll bar swales. Result showing Bernsen's method with a local radius 210m can achieve an accuracy of 92.20% across our two study sites. When applying to the whole floodplain, the mean method can achieve an accuracy of 81.02%.

Accurate floodplain land cover and geomorphic objects mapping is an important step to understand floodplain geomorphology in a large scale, result from this study could applied to finding the underlying factor of floodplain pattern change as well as river restoration, helping

decrease the chance of flooding and habitats losses. The knowledge of floodplain classification will also help authority to design the floodplain, which will benefit the sustainable agriculture, forestry management and carbon sequestration.

REFERENCES

Baatz, M., A. Schäpe, J. Strobl, T. Blaschke & G. Griesebner (2000) Multiresolution Segmentation-an optimization approach for high quality multi-scale image segmentation. Angewandte Geographische Informationsverarbeitung, 12, 12–23. Retrieved from internal-pdf. *xn--baatz_schpe_2000-3891068462-jkc/Baatz_Sch.*

Bernsen, J. 1986. Dynamic thresholding of gray-level images. In *Proc. Eighth Int'l conf. Pattern Recognition, Paris, 1986*.

Bhowmik, N. G. & J. B. Stall (1979) Hydraulic geometry and carrying capacity of floodplains.

Brondízio, E., E. Moran, P. Mausel & Y. Wu (1996) Land cover in the Amazon estuary: linking of the Thematic Mapper with botanical and historical data. *Photogrammetric Engineering and Remote Sensing,* 62**,** 921-930.

Chubey, M. S., S. E. Franklin & M. A. Wulder (2006) Object-based analysis of Ikonos-2 imagery for extraction of forest inventory parameters. *Photogrammetric Engineering & Remote Sensing,* 72**,** 383-394.

Cohen, J. (1960) A coefficient of agreement for nominal scales. *Educational and psychological measurement,* 20**,** 37-46.

Cooley, T., G. Anderson, G. Felde, M. Hoke, A. Ratkowski, J. Chetwynd, J. Gardner, S. Adler-Golden, M. Matthew & A. Berk. 2002. FLAASH, a MODTRAN4-based atmospheric correction algorithm, its application and validation. In *Geoscience and Remote Sensing Symposium, 2002. IGARSS'02. 2002 IEEE International*, 1414-1418. IEEE.

de Graaf, C. N., A. S. Koster, K. L. Vincken & M. A. Viergever (1994) Validation of the interleaved pyramid for the segmentation of 3D vector images. *Pattern Recognition Letters,* 15**,** 469-475.

Di Zenzo, S. (1986) A note on the gradient of a multi-image. *Computer vision, graphics, and image processing,* 33**,** 116-125.

Dilts, E., J. Yang & P. J. Weisberg (2010) Mapping riparian vegetation with lidar data.

Dorren, L. K., B. Maier & A. C. Seijmonsbergen (2003) Improved Landsat-based forest mapping in steep mountainous terrain using object-based classification. *Forest Ecology and Management,* 183**,** 31-46.

Drăguţ, L. & T. Blaschke (2006) Automated classification of landform elements using object-based image analysis. *Geomorphology,* 81**,** 330-344.

Dunne, T., L. A. Mertes, R. H. Meade, J. E. Richey & B. R. Forsberg (1998) Exchanges of sediment between the flood plain and channel of the Amazon River in Brazil. *Geological Society of America Bulletin,* 110**,** 450-467.

eCognition Developer, T. (2014) 9.0 User Guide. *Trimble Germany GmbH: Munich, Germany*.

Flanders, D., M. Hall-Beyer & J. Pereverzoff (2003) Preliminary evaluation of eCognition object-based software for cut block delineation and feature extraction. *Canadian Journal of Remote Sensing,* 29**,** 441-452.

Forghani, A., B. Cechet & K. Nadimpalli. 2007. Object-based classification of multi-sensor optical imagery to generate terrain surface roughness information for input to wind risk simulation. In *2007 IEEE International Geoscience and Remote Sensing Symposium*, 3090-3095. IEEE.

Franzinelli, E. & H. Igreja (2002) Modern sedimentation in the lower Negro river, Amazonas state, Brazil. *Geomorphology,* 44**,** 259-271.

Friedl, M. A., D. K. McIver, J. C. Hodges, X. Zhang, D. Muchoney, A. H. Strahler, C. E. Woodcock, S. Gopal, A. Schneider & A. Cooper (2002) Global land cover mapping from MODIS: algorithms and early results. *Remote Sensing of Environment,* 83**,** 287-302.

Frohn, R., B. Autrey, C. Lane & M. Reif (2011) Segmentation and object-oriented classification of wetlands in a karst Florida landscape using multi-season Landsat-7 ETM+ imagery. *International Journal of Remote Sensing,* 32**,** 1471-1489.

Furtado, L. F. d. A., T. S. F. Silva, P. J. F. Fernandes & E. M. L. d. M. Novo (2015) Land cover classification of Lago Grande de Curuai floodplain (Amazon, Brazil) using multi-sensor and image fusion techniques. *Acta Amazonica,* 45**,** 195-202.

Gautier, E., D. Brunstein, P. Vauchel, J. M. Jouanneau, M. Roulet, C. Garcia, J. L. Guyot & M. Castro (2010) Channel and floodplain sediment dynamics in a reach of the tropical meandering Rio Beni (Bolivian Amazonia). *Earth Surface Processes and Landforms,* 35**,** 1838-1853.

Gautier, E., D. Brunstein, P. Vauchel, M. Roulet, O. Fuertes, J.-L. Guyot, J. Darozzes & L. Bourrel (2007) Temporal relations between meander deformation, water discharge and sediment fluxes in the floodplain of the Rio Beni (Bolivian Amazonia). *Earth Surface Processes and Landforms,* 32**,** 230-248.

Gesch, D., M. Oimoen, S. Greenlee, C. Nelson, M. Steuck & D. Tyler (2002) The national elevation dataset. *Photogrammetric engineering and remote sensing,* 68**,** 5-32.

Gesch, D., M. Oimoen, Z. Zhang, J. Danielson & D. Meyer (2011) Validation of the ASTER Global Digital Elevation Model (GDEM) Version 2 over the Conterminous United States. *Report to the ASTER GDEM Version,* 2.

Gómez, C., J. C. White & M. A. Wulder (2016) Optical remotely sensed time series data for land cover classification: A review. *ISPRS Journal of Photogrammetry and Remote Sensing,* 116**,** 55-72.

Goward, S. N., J. G. Masek, D. L. Williams, J. R. Irons & R. Thompson (2001) The Landsat 7 mission: Terrestrial research and applications for the 21st century. *Remote Sensing of Environment,* 78**,** 3-12.

Graf, W. L. 1988. *Fluvial processes in dryland rivers*. Springer-Verlag New York.

Gupta, N. & H. Bhadauria (2014) Object based information extraction from high resolution satellite imagery using eCognition. *International Journal of Computer Science Issues (IJCSI),* 11**,** 139.

Gutman, G. & A. Ignatov (1998) The derivation of the green vegetation fraction from NOAA/AVHRR data for use in numerical weather prediction models. *International Journal of remote sensing,* 19**,** 1533-1543.

Guyot, J. L., J. M. Jouanneau & J. G. Wasson (1999) Characterisation of river bed and suspended sediments in the Rio Madeira drainage basin (Bolivian Amazonia). *Journal of South American Earth Sciences,* 12**,** 401-410.

Harris geospatial solutions. 2019. *Fast Line-of-sight Atmospheric Analysis of Hypercubes (FLAASH)*. http://www.harrisgeospatial.com/docs/FLAASH.html (last accessed April 21, 2019).

Hassan, Q. K., C. P. Bourque & F.-R. Meng (2007) Application of Landsat-7 ETM+ and MODIS products in mapping seasonal accumulation of growing degree days at an enhanced resolution. *Journal of Applied Remote Sensing,* 1**,** 013539.

Helldén, U. 1980. *A test of Landsat-2 imagery and digital data for thematic mapping: illustrated by an environmental study in Northern Kenya*. Laboratory of Remote Sensing, Department of Physical Geography, University ….

Henik, J. J. (2012) Utilizing NDVI and remote sensing data to identify spatial variability in plant stress as influenced by management.

Huete, A., K. Didan, T. Miura, E. P. Rodriguez, X. Gao & L. G. Ferreira (2002) Overview of the radiometric and biophysical performance of the MODIS vegetation indices. *Remote sensing of environment,* 83**,** 195-213.

Huete, A., C. Justice & H. Liu (1994) Development of vegetation and soil indices for MODIS-EOS. *Remote Sensing of Environment,* 49**,** 224-234.

Hurlbert, A. H. (2004) Species–energy relationships and habitat complexity in bird communities. *Ecology Letters,* 7**,** 714-720.

Iersel, W., E. Addink, M. Straatsma & H. Middelkoop (2016) River floodplain vegetation classification using multi-temporal high-resolution colour infrared UAV imagery.

Ilhardt, B. L., E. S. Verry & B. J. Palik (2000) Defining riparian areas. *Forestry and the riparian zone, Orono, Maine***,** 7-14.

ImageJ. 2018a. *About ImageJ*. https://imagej.net/Welcome (last accessed April 21, 2019).

ImageJ. 2018b. *Auto Local Threshold*. https://imagej.net/Auto_Local_Threshold#Use (last accessed April 21, 2019).

Janssen, L. 1994. *Methodology for updating terrain object data from remote sensing data: the application of Landsat TM data with respect to agricultural fields*. Janssen.

Jet Propulsion Laboratory. 2004. *ASTER mission*. https://asterweb.jpl.nasa.gov/mission.asp (last accessed April 21, 2019).

Jet Propulsion Laboratory. 2019. *Mission overview*. https://www2.jpl.nasa.gov/srtm/missionoverview.html (last accessed April 21, 2019).

Jiang, Z., A. R. Huete, K. Didan & T. Miura (2008) Development of a two-band enhanced vegetation index without a blue band. *Remote sensing of Environment,* 112**,** 3833-3845.

Jones, J. L. (2006) Side channel mapping and fish habitat suitability analysis using lidar topography and orthophotography. *Photogrammetric Engineering and Remote Sensing,* 72**,** 1202.

Junk, W. J., P. B. Bayley & R. E. Sparks (1989) The flood pulse concept in river-floodplain systems. *Canadian special publication of fisheries and aquatic sciences,* 106**,** 110-127.

Kampouraki, M., G. Wood & T. Brewer. 2008. Opportunities and limitations of object based image analysis for detecting urban impervious and vegetated surfaces using true-colour aerial photography. In *Object-Based Image Analysis*, 555-569. Springer.

Kartikeyan, B., A. Sarkar & K. Majumder (1998) A segmentation approach to classification of remote sensing imagery. *International Journal of Remote Sensing,* 19**,** 1695-1709.

Kellndorfer, J., W. Walker, L. Pierce, C. Dobson, J. A. Fites, C. Hunsaker, J. Vona & M. Clutter (2004) Vegetation height estimation from shuttle radar topography mission and national elevation datasets. *Remote sensing of Environment,* 93**,** 339-358.

Khatami, R., G. Mountrakis & S. V. Stehman (2016) A meta-analysis of remote sensing research on supervised pixel-based land-cover image classification processes: General guidelines for practitioners and future research. *Remote Sensing of Environment,* 177**,** 89-100.

Kim, M., M. Madden & B. Xu (2010) GEOBIA vegetation mapping in Great Smoky Mountains National Park with spectral and non-spectral ancillary information. *Photogrammetric Engineering & Remote Sensing,* 76**,** 137-149.

Latrubesse, E. M. & E. Franzinelli (2002) The Holocene alluvial plain of the middle Amazon River, Brazil. *Geomorphology,* 44**,** 241-257.

Latrubesse, E. M., J. C. Stevaux & R. Sinha (2005) Tropical rivers. *Geomorphology,* 70**,** 187-206.

Levine, M. D. & A. M. Nazif (1985) Dynamic measurement of computer generated image segmentations. *IEEE Transactions on Pattern Analysis and Machine Intelligence***,** 155-164.

Lewinski, S. 2006. Applying fused multispectral and panchromatic data of Landsat ETM+ to object oriented classification. In *Proceedings of the 26th EARSeL Symposium, New Developments and Challenges in Remote Sensing*. Warsaw, Poland.

Liang, S., H. Fang & M. Chen (2001) Atmospheric correction of Landsat ETM+ land surface imagery. I. Methods. *IEEE Transactions on geoscience and remote sensing,* 39**,** 2490-2498.

Liu, C., P. Frazier & L. Kumar (2007) Comparative assessment of the measures of thematic classification accuracy. *Remote sensing of environment,* 107**,** 606-616.

Marpu, P., M. Neubert, H. Herold & I. Niemeyer (2010) Enhanced evaluation of image segmentation results. *Journal of spatial science,* 55**,** 55-68.

Matsushita, B., W. Yang, J. Chen, Y. Onda & G. Qiu (2007) Sensitivity of the enhanced vegetation index (EVI) and normalized difference vegetation index (NDVI) to topographic effects: a case study in high-density cypress forest. *Sensors,* 7**,** 2636-2651.

McFeeters, S. K. (1996) The use of the Normalized Difference Water Index (NDWI) in the delineation of open water features. *International journal of remote sensing,* 17**,** 1425-1432.

Mertes, L. A. & T. Dunne. 2007. *Effects of tectonism, climate change, and sea-level change on the form and behaviour of the modern Amazon River and its floodplain*. Wiley.

Mertes, L. A., T. Dunne & L. A. Martinelli (1996) Channel-floodplain geomorphology along the Solimões-Amazon river, Brazil. *Geological Society of America Bulletin,* 108**,** 1089-1107.

Myint, S. W., P. Gober, A. Brazel, S. Grossman-Clarke & Q. Weng (2011) Per-pixel vs. object-based classification of urban land cover extraction using high spatial resolution imagery. *Remote sensing of environment,* 115**,** 1145-1161.

Nanson, G. & J. Croke (1992) A genetic classification of floodplains. *Geomorphology,* 4**,** 459-486.

NASA/METI/AIST/Japan Space Systems (2009) ASTER global digital elevation model [data set]. *NASA EOSDIS Land Processes DAAC*.

Neubert, M., H. Herold & G. Meinel. 2008. Assessing image segmentation quality–concepts, methods and application. In *Object-based image analysis*, 769-784. Springer.

Nghiem, S., D. Balk, C. Small, U. Deichmann, A. Wannebo, R. Blom, P. Sutton, G. Yetman, R. Chen & E. Rodriguez (2001) Global infrastructure: The potential of SRTM data to break new ground. *White Paper Produced by CIESIN and NASA's Jet Propulsion Laboratory*.

Niblack, W. 1986. *An introduction to digital image processing*. Prentice-Hall Englewood Cliffs.

Oguro, Y., Y. Suga, S. Takeuchi, H. Ogawa & K. Tsuchiya (2003) Monitoring of a rice field using Landsat-5 TM and Landsat-7 ETM+ data. *Advances in Space Research,* 32**,** 2223-2228.

Olson, P. L., N. T. Legg, T. B. Abbe, M. A. Reinhart & J. K. Radloff. 2014. A methodology for delineating planning-level channel migration zones. Washington (State). Dept. of Ecology.

Otsu, N. (1979) A threshold selection method from gray-level histograms. *IEEE transactions on systems, man, and cybernetics,* 9**,** 62-66.

Pal, N. R. & S. K. Pal (1989) Entropic thresholding. *Signal processing,* 16**,** 97-108.

Phansalkar, N., S. More, A. Sabale & M. Joshi. 2011. Adaptive local thresholding for detection of nuclei in diversity stained cytology images. In *2011 International Conference on Communications and Signal Processing*, 218-220. IEEE.

Powers, R. P., G. J. Hay & G. Chen (2012) How wetland type and area differ through scale: A GEOBIA case study in Alberta's Boreal Plains. *Remote Sensing of Environment,* 117**,** 135-145.

Remsen Jr, J. & T. A. Parker III (1983) Contribution of river-created habitats to bird species richness in Amazonia. *Biotropica***,** 223-231.

Robinson, N., J. Regetz & R. P. Guralnick (2014) EarthEnv-DEM90: A nearly-global, void-free, multi-scale smoothed, 90m digital elevation model from fused ASTER and SRTM data. *ISPRS Journal of Photogrammetry and Remote Sensing,* 87**,** 57-67.

Rodriguez, E., C. Morris, J. Belz, E. Chapin, J. Martin, W. Daffer & S. Hensley (2005) An assessment of the SRTM topographic products.

Rodriguez, E., C. S. Morris & J. E. Belz (2006) A global assessment of the SRTM performance. *Photogrammetric Engineering & Remote Sensing,* 72**,** 249-260.

Rosenfield, G. H. & K. Fitzpatrick-Lins (1986) A coefficient of agreement as a measure of thematic classification accuracy. *Photogrammetric engineering and remote sensing,* 52**,** 223-227.

Sahoo, P. K., S. Soltani & A. K. Wong (1988) A survey of thresholding techniques. *Computer vision, graphics, and image processing,* 41**,** 233-260.

Sauvola, J. & M. Pietikäinen (2000) Adaptive document image binarization. *Pattern recognition,* 33**,** 225-236.

Sezgin, M. & B. Sankur (2004) Survey over image thresholding techniques and quantitative performance evaluation. *Journal of Electronic imaging,* 13**,** 146-166.

Short, N. M. (1982) Landsat tutorial workbook.

Skidmore, A. (1989) Unsupervised training area selection in forests using a nonparametric distance measure and spatial information. *Remote Sensing,* 10**,** 133-146.

Soille, P. 2013. *Morphological image analysis: principles and applications*. Springer Science & Business Media.

Soudani, K., C. François, G. Le Maire, V. Le Dantec & E. Dufrêne (2006) Comparative analysis of IKONOS, SPOT, and ETM+ data for leaf area index estimation in temperate coniferous and deciduous forest stands. *Remote sensing of environment,* 102**,** 161-175.

Story, M. & R. G. Congalton (1986) Accuracy assessment: a user's perspective. *Photogrammetric Engineering and remote sensing,* 52**,** 397-399.

Strick, R. J., P. J. Ashworth, G. Awcock & J. Lewin (2018) Morphology and spacing of river meander scrolls. *Geomorphology,* 310**,** 57-68.

Strick, R. J. P. 2016. Floodplain Geomorphology and Topography in Large Rivers. University of Brighton.

Sun, X., H. Du, N. Han, G. Zhou, D. Lu, H. Ge, X. Xu & L. Liu (2014) Synergistic use of Landsat TM and SPOT5 imagery for object-based forest classification. *Journal of Applied Remote Sensing,* 8**,** 083550.

Syed, S., P. Dare & S. Jones. 2005. Automatic classification of land cover features with high resolution imagery and lidar data: an object-oriented approach. In *Proceedings of SSC2005 spatial intelligence, innovation and praxis: the national biennial conference of the spatial sciences institute*, 512-522. Melbourne: Spatial Science Institute Melbourne.

Tachikawa, T., M. Kaku, A. Iwasaki, D. B. Gesch, M. J. Oimoen, Z. Zhang, J. J. Danielson, T. Krieger, B. Curtis & J. Haase. 2011. ASTER global digital elevation model version 2-summary of validation results. NASA.

Tatsumi, K., Y. Yamashiki, M. A. C. Torres & C. L. R. Taipe (2015) Crop classification of upland fields using Random forest of time-series Landsat 7 ETM+ data. *Computers and Electronics in Agriculture,* 115**,** 171-179.

Thomas, I., N. Ching, V. Benning & J. D'aguanno (1987) Review Article A review of multi-channel indices of class separability. *International Journal of Remote Sensing,* 8**,** 331-350.

Thomas, N., C. Hendrix & R. G. Congalton (2003) A comparison of urban mapping methods using high-resolution digital imagery. *Photogrammetric Engineering & Remote Sensing,* 69**,** 963-972.

Trahanias, P. E. & A. N. Venetsanopoulos (1993) Color edge detection using vector order statistics. *IEEE Transactions on Image Processing,* 2**,** 259-264.

Trimble. 2010. *Trimble acquires definiens' earth sciences business to expand its geospatial portfolio*. http://investor.trimble.com/news-releases/news-release-details/trimble-acquires-definiens-earth-sciences-business-expand-its (last accessed April 21, 2019).

Trimble. 2011. eCognition Developer 8.64. 1 reference book, version 8.64. 1. Trimble Germany GmbH München, Germany.

Turk, G. (2002) Map evaluation and" chance correction". *Photogrammetric Engineering and Remote Sensing*, 68**,** 123-+.

Turner, M. & R. Congalton (1998) Classification of multi-temporal SPOT-XS satellite data for mapping rice fields on a West African floodplain. *International Journal of Remote Sensing*, 19**,** 21-41.

USGS. 2016. *A Vision to Observe Earth*. https://www.usgs.gov/news/vision-observe-earth (last accessed April 21, 2019).

USGS. 2019a. *Landsat Missions*. https://www.usgs.gov/land-resources/nli/landsat (last accessed April 21, 2019).

USGS. 2019b. *Landsat processing details*. https://landsat.usgs.gov/landsat-processing-details (last accessed April 21, 2019).

Valor, E. & V. Caselles (1996) Mapping land surface emissivity from NDVI: Application to European, African, and South American areas. *Remote sensing of Environment*, 57**,** 167-184.

Wei, W., X. Chen & A. Ma. 2005. Object-oriented information extraction and application in high-resolution remote sensing image. In *Geoscience and Remote Sensing Symposium, 2005. IGARSS'05. Proceedings. 2005 IEEE International*, 3803-3806. IEEE.

Wong, W. V., S. Tsuyuki, K. Loki & M. Phua. 2014. Accuracy assessment of global topographic data (SRTM & ASTER GDEM) in comparison with lidar for tropical montane forest. In *Proceedings of the 35th Asian Conference on Remote Sensing, Nay Pyi Taw, Myanmar*, 27-31.

Wu, C., L. Wang, Z. Niu, S. Gao & M. Wu (2010) Nondestructive estimation of canopy chlorophyll content using Hyperion and Landsat/TM images. *International Journal of Remote Sensing,* 31**,** 2159-2167.

Yengoh, G. T., D. Dent, L. Olsson, A. E. Tengberg & C. J. Tucker (2014) The use of the Normalized Difference Vegetation Index (NDVI) to assess land degradation at multiple scales: a review of the current status, future trends, and practical considerations. *Lund University Center for Sustainability Studies (LUCSUS), and The Scientific and Technical Advisory Panel of the Global Environment Facility (STAP/GEF),* 47.

Zhang, Y., T. Maxwell, H. Tong & V. Dey. 2010. *Development of a supervised software tool for automated determination of optimal segmentation parameters for ecognition*. na.

Zhang, Y. J. (1996) A survey on evaluation methods for image segmentation. *Pattern recognition,* 29**,** 1335-1346.